Declaration

I hereby certify that this thesis is the product of my own research and any material which does not belong to my work has been appropriately cited or acknowledged. No part of this thesis has been or is being submitted for any other degree.

Tristan Barrett

University department of Radiology
Cambridge University Hospitals NHS Foundation Trust

Dated: 8/2/2018

FUNCTIONAL IMAGING TO ENABLE MORE ACCURATE LOCALISATION AND CHARACTERISATION OF PROSTATE TUMOURS

Tristan Barrett

This dissertation is submitted for the degree of Doctor of Medicine (MD)

September 2017

Clare Hall College
University of Cambridge

Functional Imaging to enable more accurate localisation and characterisation of prostate tumours

Abstract

Prostate cancer is the leading cause of cancer death in men after skin cancer, with an incidence expected to double by 2030 mainly due to the ageing population. However, many more men die with prostate cancer rather than from the disease, highlighting the indolent nature of many tumours. Therefore, the development of non-invasive imaging methods to stratify prostate cancer is important for patient management.

Recently, multiparametric MRI has revolutionised the work-up of prostate cancer, becoming a routine part of clinical practice and migrating earlier in the diagnostic pathway. However, the technique remains challenging, with patient-related factors, intrinsic insensitivity of MRI, protocol differences, and radiologist experienced all combining to limit its overall accuracy. Anatomical T2-weighted imaging is limited by the non-specific nature of its findings and improvements have mainly been driven by the addition of functional sequences such as diffusion-weighted imaging, dynamic contrast-enhanced MRI and spectroscopy. In the absence of validated circulating biomarkers, only functional imaging currently offers the potential for further improvements in lesion detection and characterisation, with the additional advantages of providing whole gland coverage of the prostate and being non-invasive.

This thesis addresses the issues of prostate tumour localisation and characterisation using functional imaging techniques. Chapter 2 assesses whether simple pre-imaging interventions relating to patient preparation can help improve MRI quality. Chapter 3

evaluates the potential for two novel functional MR sequences to differentiate tumour from normal prostate tissue. Chapter 4 investigates whether non-proton sodium MRI can offer functional information reflecting cell membrane integrity and cell viability. Chapter 5 evaluates whether the PET/CT tracer ^{11}C-acetate can offer additive information on primary prostate tumours.

Tristan Barrett

Acknowledgements

While this thesis is my own work, I am deeply grateful to a wide group of colleagues and co-workers who have provided advice and support, and whose collaboration and hard work have made this possible.

I am grateful to Sarah Hilborne and Jackie Mason in Radiology and to Kelly Leonard and Sara Stearn in Urology for their tireless efforts to recruit patients and to Rhys Slough and Ilse Patterson in MRI, and Vic Warnes in PET-CT for their help in scheduling research scans, often at short notice.

I would like to thank my colleagues in Urology including Christof Kastner, Vincent Gnanapragasam, Nimish Shah and Ola Bratt who have believed in the clinical value of radiology in prostate cancer from the very start and have shown enthusiasm and willingness to develop project ideas in both the research and clinical settings.

I would also like to thank my colleagues in radiology who helped me analysis and critically appraise results, including, but not limited, to Andrew Gill, Mary McLean, Andrew Patterson, and Andrew Priest and, in particular, to Ferdia Gallagher who has served as a mentor, peer, supervisor, colleague, adviser and friend during this period.

Finally, I am indebted to the support provided by Fiona Gilbert as head of department and supervisor for my MD, both in fulfilling this work and for enabling me to develop as an academic radiologist.

Table of Contents

List of Figures

List of Tables

Abbreviations

ADC = apparent diffusion coefficient

ANT = Advanced Normalization Tools

ARSAC = administration of radioactive substances advisory committee

AS = active surveillance

ATP = adenosine triphosphate

BPH = benign prostatic hypertrophy

CO_2 = Carbon Dioxide

CT = computed tomography

CZ = central zone

DCE = dynamic contrast-enhanced

DKI = diffusional kurtosis imaging

DRE = digital rectal examination

DTI = diffusion tensor imaging

DWI = diffusion-weighted imaging

ED = effective dose

EPI = echo-planar imaging

ERC = endorectal coil

ERSPC = European randomized study of screening for prostate cancer

ESUR = European Society of Urogenital Radiology

FAS = fatty acid synthase

FDA = food and drug administration

FDG = fluorodeoxyglucose

FOV = field-of-view

FRFSE = fast-relaxation fast spin echo

GFR = glomerular filtration rate

H&E = hematoxylin and eosin

HBB = hyoscine butylbromide

IVIM = intravoxel incoherent motion

IR = inversion recovery

MBq = megabecquerel

mpMRI = multiparametric magnetic resonance imaging

mSv = millisievert

MTI = magnetization transfer imaging

MTR = magnetization transfer ratio

OSEM = ordered-subsets expectation maximisation

PACS = picture archiving and communication system

PCa = prostate cancer

PET = positron emission tomography

p.i. = post injection

PIN = prostatic intraepithelial neoplasia

PI-RADS = prostate imaging reporting and data system

PLCO = prostate, lung, colorectal and ovarian

PSA = prostate-specific antigen

PSMA = prostate-specific membrane antigen

PZ = peripheral zone

ROC = receiver operating characteristic

ROI = region-of-interest

SAR = specific absorption ratio

SEER = surveillance, epidemiology, and end results

SNR = signal-to-noise ratio

SUV = standardized uptake values

SV = seminal vesicle

SyN = symmetric normalisation

TBR = target-to-background ratio

TCA = tricarboxylic acid

TE = echo time

TOF = time-of-flight

TPUS = transperineal ultrasound

TR = repetition time

TRUS = transrectal ultrasound

TSC = tissue sodium concentration

TZ = transition zone

US = ultrasound

USPSTF = United States preventive services task force

Chapter 1: Background

This chapter provides an overview of prostate cancer incidence and epidemiology, the current clinical work-up of the disease in the UK and its limitations, the sequences that form part of multiparametric (mp) MRI of the prostate, and the evolving role of MRI in the diagnostic pathway.

1.1 Epidemiology of prostate cancer

Prostate cancer (PCa) is the most common non-cutaneous malignancy in men worldwide, and accounts for almost 1-in-5 of all new male cancer diagnoses [1]. In 2014 there were 46,690 new cases in the UK, with the global incidence of the disease expected to double by 2030, in part due to the ageing population [2, 3]. Despite the high incidence overall, prognosis is good with cancer-specific survival being 84% at 10 years [2].

In 1986 the US Food and Drug Administration (FDA) approved the prostate-specific antigen (PSA) test for monitoring PCa progression, and in 1994 approved its use alongside digital rectum examination (DRE) to test asymptomatic men. This introduction led to a spike in incidence in the early 1990s (**Figure 1.1**) due to a surge in the detection of asymptomatic disease [4]. The name PSA is a misnomer as it is not specific to the prostate and is known to be produced in the lung and salivary glands, and may even be expressed by breast, ovarian and endometrial tumours [5]. Moreover, it is not specific to cancer of the prostate and can be raised in benign prostatic hypertrophy (BPH), inflammation, infection, and trauma.

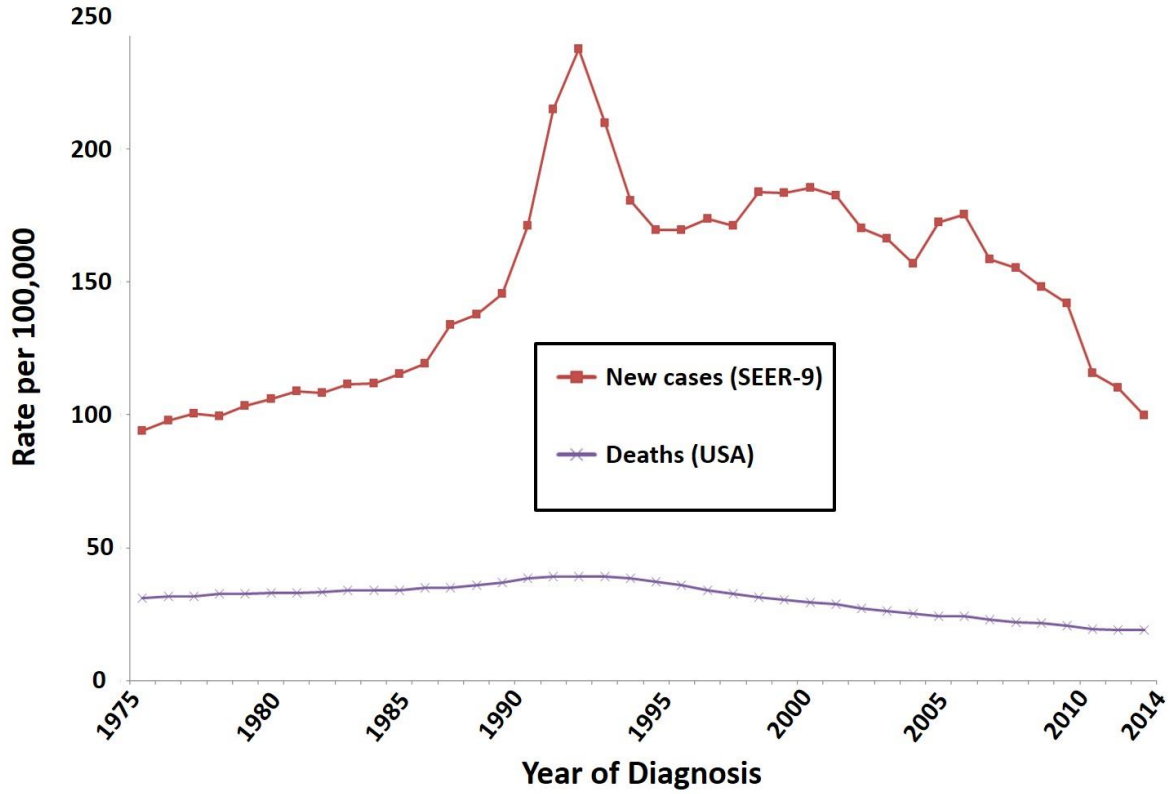

Figure 1.1. Surveillance, Epidemiology, and End Results (SEER) program: US men prostate cancer incidence and mortality [14]

Several screening studies have attempted to quantify the benefit of PSA as a screening test, the largest being the USA Prostate, Lung, Colorectal and Ovarian (PLCO) cancer screening trial and the European Randomized Study of Screening for Prostate Cancer (ERSPC). The PLCO study reported more diagnoses of PCa in the screened group at 10 years, but with a similar death rate in each arm [6]. Although an upper limit of normal PSA is quoted as 4.0 ng/ml for men aged over 60 years, many men with PSA below this threshold will have cancer, and PSA therefore represents a continuum of risk at all values [7]. The sensitivity and specificity of a raised PSA at >4.1 ng/ml is 20% and 94%, respectively [8]; this low sensitivity arguably means PSA fails the primary goal of a screening test, namely detecting cancer. Current European and US guidelines from the Preventive Services Task Force (USPSTF) therefore do not recommend population screening for prostate cancer [9]. More recently the incidence of prostate cancer in the US has declined dramatically and by more

than 10% annually from 2010 to 2013, which is likely to relate directly to the USPSTF recommending against routine use of PSA for screening purposes [1]. However, the USPSTF recently recommended that PSA can be selectively offered to men aged 55 to 69 years, depending on individual circumstances, professional judgment and patient preferences, as they consider there to be at least moderate certainty of the net benefit being small (category C) [10]. PSA-based screening for prostate cancer continues to be discouraged for men age 70 years and older (category D). It remains to be seen how this impacts on prostate cancer diagnosis.

1.2 Potential for over-diagnosis

While 1-in-6 men are diagnosed with prostate cancer, only 1-in-36 will die from the disease [11]. This highlights the indolent nature of many of the tumours currently diagnosed and it remains true that many more men will die with prostate cancer than directly because of the disease.

The introduction of PSA testing dramatically changed the profile of patients presenting with prostate cancer. The average age at presentation reduced from 64 to 59 years, index lesion volume reduced by more than 50% with fewer tumours therefore detectable by DRE, and the majority now present with low risk rather than high risk disease [12]. Additionally, soon after widespread PSA use, the average PSA level at presentation had reduced from 25 to 8 ng/ml, whilst the average gland volume increased from 44 to 53 cm^3, meaning that a raised PSA at baseline shifted from being indicative of cancer to being more likely to be due to BPH [13]. The implication is that this practice has led to the over-diagnosis of clinically insignificant cancer that would not otherwise have resulted in symptoms or cancer-related

death [14]. Indeed, whilst the overall incidence of prostate cancer has declined over the last 10 years, the rates for higher stage and distant disease have been stable in the same period [15], suggesting it is the diagnosis of indolent disease that has been reduced. However, there remains the risk that current urological practice may serve to exacerbate the problem of over-diagnosis. Repeating PSA tests, using a lower PSA threshold for performing prostatic biopsy, taking more cores at biopsy, and repeating a biopsy after initial negative results, are all factors which are likely to lead to a further increase in the incidence of lower grade, smaller volume, and relatively indolent cancer [12].

1.3 Risk of over-treatment

Over-diagnosis in itself is not a problem, but this potentially leads to over-treatment of indolent disease, which is an issue due to the associated risk of significant morbidity. The traditional radical treatment of prostate cancer with either prostatectomy or external beam radiation therapy carries with it a 50-60% risk of erectile dysfunction and, although the rates of severe urinary incontinence are low, as many as 30% continue to report some symptoms at long-term follow-up [16-18].

It is estimated that in screen-detected populations, 48 men will need to undergo treatment to prevent 1 prostate cancer death [19]; this ratio compares unfavourably with breast cancer screening programs where 3 patients need treatment to prevent 1 death [20]. Indeed, the USPSTF recommendations against PSA for screening purposes are mainly based on these growing concerns about over-treatment [9].

Active surveillance (AS) has recently emerged as a means of addressing such over-treatment

and is now recommended as the management strategy of choice in men with low-risk localized prostate cancer for whom radical therapy remains a clinical option [21]. This approach is supported by Level 1 evidence that not all men diagnosed with prostate cancer need active treatment, and that radical curative therapy only benefits those with more aggressive, high-risk disease [22, 23]. The Prostate Cancer Intervention Versus Observation Trial (PIVOT) was the first well controlled trial to assess the impact of radical prostatectomy compared with observation and suggests that for patients with low risk disease (diagnosed by systematic TRUS biopsy) or PSA ≤ 10, treatment does not confer a prostate-cancer mortality advantage, however, those with higher risk disease would benefit from intervention [22]. A recent update of the PIVOT trial at longer term follow-up, suggests that surgery may also be associated with lower all-cause mortality than observation among men with intermediate-risk disease [24].

1.4 Risk of under-treatment

Prostate cancer is almost unique amongst solid organ tumours in that it is predominantly diagnosed by an indirect, non-targeted method. The standard diagnostic test for clinically suspected prostate cancer remains transrectal ultrasound (TRUS) guided biopsy. The biopsy needle is “guided”, but only to the prostate gland rather than to a tumour and systematically under-samples the anteriorly gland, the midline and the extreme apex. Ultimately only 1% of the gland is sampled and therefore TRUS biopsy is unsurprisingly prone to sampling error [25]. It is well established that TRUS biopsy underestimates aggressiveness in around one-third of cases [26], underestimates volume in one-half of cases, and may miss up to 50% of clinically significant tumours [27]. Therefore, whilst over-treatment is a concern there is also a real risk of traditional diagnostic pathways resulting in

under-treatment due to misclassifying cancers as being less aggressive or incorrectly categorizing patients as being tumour free.

1.5 Role of Imaging in Prostate Cancer

Given this potential for both under- and over-treatment, there needs to be a rethink in how patients are assessed diagnostically. There are several blood tests available that may serve as indicators of prostate cancer including PCA-3, the 4K score test, and the Prostate health index, with increasing excitement about a potential role for circulating tumour DNA [28, 29]. However, there are currently no blood or urine-based biomarkers that can reliably locate the presence of a high-grade aggressive tumour in the prostate [29]. Realistically, imaging offers the greatest potential of differentiating these more aggressive, lethal cancers.

Imaging has traditionally performed a limited role of staging in higher risk tumours with MRI being used for local staging and CT or bone scintigraphy for nodal and bone metastases. However, multi-parametric MRI (mp-MRI), incorporating multi-planar T_2-weighted, and functional DCE and diffusion-weighted imaging, has now been validated as a means of detecting prostate tumours [30, 31].

Alongside accurate risk stratification of prostate tumours, another driver to improved tumour detection and localisation is to aid biopsy targeting. Current UK guidelines recommend that mpMRI be performed in high risk patients following a negative systematic TRUS biopsy in order to target subsequent repeat biopsy [32]. A recent meta-analysis demonstrated that in the re-biopsy population, mpMRI increased the detection rates of significant cancers by 54% and reduced insignificant (indolent) cancer detection by 18% [33].

As a result, some authors even suggest that MRI should replace TRUS biopsy as the initial diagnostic test for prostate cancer to enable guidance of subsequent biopsy [34]. However, the data is less convincing in biopsy naïve patients, where mpMRI guided prostate biopsy only marginally increases the detection rates of significant disease by 10%, although it remains of benefit in reducing insignificant cancer detection by 49% [33]. This diagnostic gain has to be balanced against the restrictions of the UK national 31-day time-to-diagnosis targets and difficulty in obtaining an MRI at short notice. Reserved MRI slots may be difficult to justify if (even occasionally) they are left unfilled given that MRI is a relatively scarce resource.

Nevertheless, several UK centres have implemented MRI pre-biopsy over and above national guidelines. The 2017 update of the National Prostate Cancer Audit suggests that in men who do undergo MR imaging for prostate cancer, this is being performed prior to first biopsy in 73% of cases [35]. Indeed, the London Cancer Alliance Best Practice Prostate Pathway has highlighted pre-biopsy MRI as a key component of delivering prostate cancer diagnosis and treatment within the 62 day national cancer target [36]. Pre-biopsy prostate MRI is not appropriate for all patients, but is indicated in candidates for radical curative treatment when there is a palpable abnormality on DRE, or in men with two raised PSA measurements, or high clinical suspicion of prostate cancer, or to potentially avoid the adverse effects of biopsy, if considered to be of high risk. The recently published Prostate MRI Imaging Study (PROMIS) supports this practice and is likely to influence future UK guidelines [37]. PROMIS demonstrated that mpMRI in biopsy-naïve patients outperforms systematic TRUS biopsy, the current standard of care. As a triage test, mpMRI could potentially avoid unnecessary biopsy in 27% of patients, whilst diagnosing up to 18% more

cases of clinically significant cancer and 5% fewer clinically insignificant cancers. Clearly the increased use of MRI in biopsy naïve patients brings additional challenges, with the emphasis of radiological interpretation shifting from one of basic staging to lesion detection and characterisation in order to direct subsequent sampling.

1.6 What is prostate multiparametric MRI?

Multiparametric (mp) MRI of the prostate is the addition of functional imaging to standard anatomical T1 and T2-weighted imaging [38]. The available functional sequences include diffusion-weighted imaging (DWI) with calculation of apparent diffusion coefficient (ADC) maps, dynamic contrast-enhanced (DCE) MRI, and spectroscopic imaging.

Anatomical T2 weighted imaging was the earliest available sequence and remains the optimal sequence for assessment of the transition zone (TZ). Its value in the peripheral zone (PZ) where tumour appears as low signal intensity is more limited due to a number of benign conditions which mimic this appearance, including prostatic intraepithelial neoplasia (PIN), prostatitis, haemorrhage, atrophy, scarring, and post-treatment change [39].

DWI is an MR technique that images the diffusion of water molecules and does not require administration of an exogenous contrast agent. Tumours will typically demonstrate restricted diffusion due to increased cellularity preventing extracellular diffusion of water and an increased nuclear:cytoplasmic ratio, which limits intracellular diffusion. An absolute restriction limit cannot be reached in extracranial tissues and thus the term “impeded” rather than “restricted” diffusion is more physiologically correct for body DW imaging, however, the term “restricted diffusion” will be used throughout this thesis due to its

widespread adoption in the existing literature.

DCE-MRI requires intravenous administration of a low molecular weight Gadolinium chelate. Tumours form their own blood vessels once they grow above a certain size, with this neo-angiogenesis being disorganised, leading to porous endothelia. Gadolinium rapidly washes-into the tumour interstitium, being visualised as early signal change due to contrast enhancement, and then washes-out. Analysis of DCE MRI curves is effective in breast disease as the pattern can differentiate benign and malignant lesions - a Type I curve (slow, late, continuous enhancement) is rarely associated with malignancy (~9%), whereas a Type 3 pattern (early enhancement with peak and wash-out) has a 90.4% specificity for cancer [40]. However, this "curvology" based approach does not work well in the prostate because benign conditions such as prostatitis and hypervascular BPH nodules can have a Type 3 curve, and overall it is more common for tumours to demonstrate a Type 2 curve (early enhancement and plateau) making it difficult to accurately differentiate malignancy [41]. As a result, the role of DCE-MRI has been significantly downplayed in the Prostate Imaging Reporting and Data System (PI-RADS) guidelines, version 2 and only concentrates on the wash-in phase [42].

MR spectroscopy is challenging, often requiring significant post-processing and additional input from MR physicists. The paradigm is based on tumour cell proliferation and cell membrane turnover leading to an increased amount of choline, with a corresponding reduction in citrate levels, a metabolite produced by the normal prostate and therefore a marker of benign tissue. The low sensitivity (16%) makes spectroscopy poor for lesion detection, and although it has an excellent specificity (approaching 100%) and can improve

lesion characterisation, the incremental benefit is comparatively small [43], in particular relative to the step-wise increase in costs incurred [44]. As a result, the most recent version of the PI-RADS guidelines (version 2) has dropped spectroscopy and "mpMRI" therefore should incorporate T2-weighted imaging, DWI and DCE-MRI [41]; **Figure 1.2**. Despite this, a recent National Prostate Cancer Audit in the UK highlighted the fact that although 99% of hospitals in England have access to on-site MRI only 75% are providing mpMRI [45].

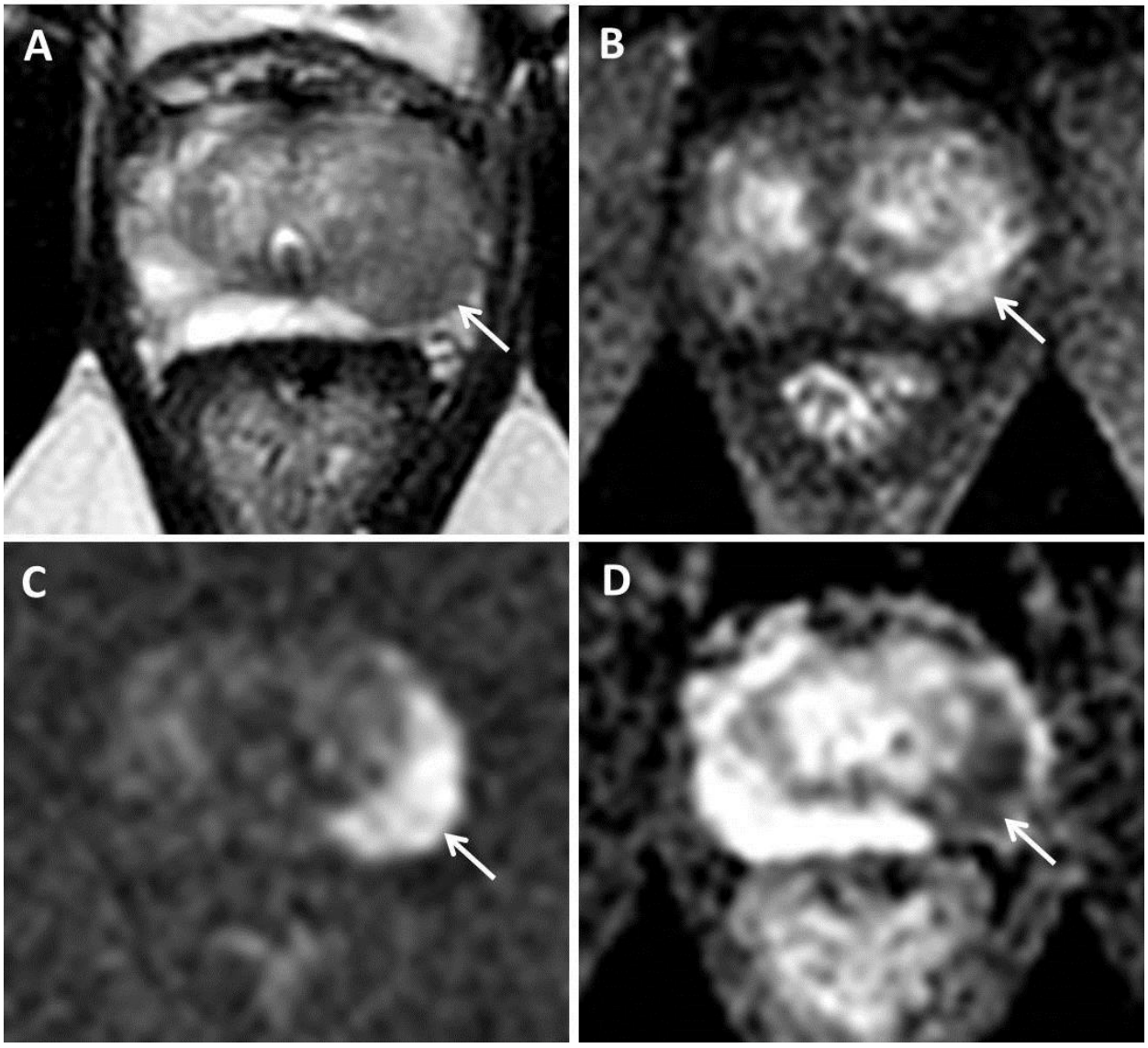

Figure 1.2 Standard clinical mpMRI diagnostic sequences. 73 year old patient, PSA 9.85 ng/ml, MRI performed pre-biopsy. High probability (PI-RADS score 5) 19×10 mm lesion in the left mid PZ (arrows). Lesion demonstrates focal low T2 signal (A), early enhancement on DCE compared to contralateral PZ (B), high signal on b-2000 DWI (C), and low signal on ADC maps (D). Targeted biopsy revealed Gleason 3+4 disease in 50% and 13 mm of all 3 cores, maximum tumour length 9 mm.

1.7 Prostate Imaging Reporting and Data System (PI-RADS)

MR imaging is in general less reproducible between centres than CT, plain film or ultrasound. The reasons are multifactorial and include the magnet strength, coil technology (endorectal coil versus body coil, number of elements), software version being run and protocol set-up (e.g., choice of b-values for DWI). This makes inter-centre comparison challenging, particularly for quantifiable measurements derived from DWI and DCE-MRI. Other inter-patient factors that may be difficult to control include artefact due to hip metalwork, prior biopsy, rectal loading, and tumour-specific factors including a sparse growth pattern [46]; **Table 1.1.**

Technical Factors	Patient-related Factors
The prostate is a small organ	Biopsy-related artefact
Magnet strength (1.5 versus 3T)	Previous treatment
Coil used (body versus endorectal)	Patient motion
Vendor-related differences	Rectal loading and spasm
Number of b-values selected and their value	Hip metalwork
Software upgrades	Normal structures mimicking PCa
Tumour-related Factors	**Radiologist Factors**
Grade of lesion	Subjective interpretation
Size of lesion	Experience/known learning curve
Sparse pattern of growth	Reporting standardisation

Table 1.1 Factors that make mpMRI interpretation challenging

Another variable to consider is the experience of the radiologist. We reviewed our prostate MR interpretation and outcomes based on template transperineal biopsy performed locally and demonstrated a significant increase in cancer detection from 27% to 63%, with a concurrent increase in NPV from 66.6% to 88.9% during a defined learning curve period [47]. There is no data on how many prostate MRIs should be reported to reach the top of this learning curve, but anecdotally 100-150 reports need to supervised and with pathology feedback to achieve an appropriate competence [48]. Beyond this it is recommended that radiologists report at least 50 mpMRIs per year, audit their results, and regularly attend MDT meetings in which outcomes are discussed, in order to maintain competency levels [34].

It is with these MRI protocol-related and radiologist-specific factors in mind that the European Society of Urogenital Radiology (ESUR) in 2012 first devised recommendations based on consensus expert opinion aimed at standardising the acquisition, interpretation and reporting of prostate MRI [49]. These guidelines were modelled on similar efforts in mammography (BI-RADS) that led to the transformation of breast cancer care and became popularly known as “Prostate Imaging-Reporting and Data System” (PI-RADS). Subsequent studies validated PI-RADS in certain research and clinical settings, however, experience also highlighted limitations, in part due to technical improvements. A joint steering committee formed by the American College of Radiology ESUR, and the non-profit organisation AdMeTech Foundation, updated the original guidance, with PI-RADS version 2 made available in early 2015 [50]. The key changes related to MRI acquisition, with spectroscopy being dropped and a single acquisition protocol being recommended and to MRI interpretation, with the concept of a dominant sequence, namely DWI in the PZ and T2WI in

the TZ and secondary sequences (DCE in the PZ and DWI in the TZ) which can upgrade a score “3” to a score “4”. The sequence-specific scoring system is summarised below (**Table 1.2**), with the dominant sequence principle being applied in order derive an overall PI-RADS score of 1-5 for tumour probability, wherein 1 = very low (clinically significant cancer is highly unlikely to be present), 2 = low (clinically significant cancer is unlikely to be present), 3 = intermediate (the presence of clinically significant cancer is equivocal), 4 = high (clinically significant cancer is likely to be present), 5 = very high (clinically significant cancer is highly likely to be present).

T2W for Peripheral Zone	
1	Uniform high signal intensity
2	Linear, wedge shaped, or geographic areas of lower SI, usually not well demarcated
3	Heterogeneous signal intensity or non-circumscribed, rounded, moderate hypointensity. Or other not in categories 1/2 or 4/5
4	Circumscribed, homogenous moderate hypointense focus/mass confined to prostate and <1.5 cm in greatest dimension
5	Same as 4 but ≥1.5cm in greatest dimension or definite ECE/invasive behaviour
T2W for Transition Zone	
1	Heterogeneous intermediate SI
2	Circumscribed hypointense or heterogeneous encapsulated nodule(s) (BPH)
3	Heterogeneous signal intensity with obscured margins. Or other not in categories 1/2 or 4/5
4	Lenticlular or non-circumscribed, homogeneous, moderately hypointense, and <1.5 cm in greatest dimension
5	Same as 4, but ≥ 1.5cm in greatest dimension or definite ECE /invasive behaviour
Diffusion-weighted Imaging	
1	No abnormality (i.e. normal) on ADC and high b-value DWI
2	Indistinct hypointense on ADC
3	Focal mildly/moderately hypointense on ADC and isointense/ mildly hyperintense on high b-value DWI
4	Focal markedly hypontense on ADC and markedly hyperintense on high b-value DWI; <1.5cm in greatest dimension
5	Same as 4 but ≥1.5cm in greatest dimension or definite ECE / invasive behaviour
Dynamic contrast-enhanced MRI	
-	No early enhancement **OR** Diffuse enhancement not corresponding to a focal finding on T2 and/or DWI **OR** Focal enhancement corresponding to a lesion demonstrating features of BPH on T2WI
+	Focal **AND** Earlier than or contemporaneously with enhancement of adjacent normal prostatic tissues **AND** Corresponds to suspicious finding on T2 and/or DWI

Table 1.2. PI-RADS version 2 sequence-specific scoring systems. ECE = Extra-Capsular Extension, BPH = Benign Prostatic Hypertrophy, ADC = apparent diffusion co-efficient, DWI = Diffusion-Weighted Imaging

1.8 How good is prostate mpMRI?

Although anatomical T2-weighted imaging complemented by functional diffusion-weighted imaging can be used for lesion detection, current mpMRI has inherent limitations, and the technique performs particularly poorly for detection of lower grade lesions, or those <0.5 cm^3 in size [51]. Studies report considerable variability, with sensitivity for cancer detection ranging from 53-100% and specificity 32-97%, and being dependant on the composition of the cohort selected, the gold standard employed, and technical factors [52-54].

A systematic review incorporating studies published up to February 2012, and therefore prior to the introduction of PI-RADS, showed MRI to have a pooled sensitivity of 74% and specificity of 88% [55]. A more recent PI-RADS era review of 21 studies (3,857 patients) published in 2015-2016, with all patients being imaged after 2010, showed mpMRI to have a sensitivity of 89% and specificity 74% for high probability lesions [52]. In studies directly comparing PI-RADS versions 1 and 2, it is noteworthy that version 2 resulted in an increased sensitivity (95% compared to 88%), without a reduction in specificity. This may relate to the improved inter-observer agreement demonstrated with PI-RADS version 2, particularly in the PZ [56, 57]. These results are supportive of the changes implemented in version 2, and may reflect removal of MR spectroscopy, which is known to have a high specificity, enabling lesion characterisation, but has a reported sensitivity as low as 16%, limiting lesion detection [43]. The increase in sensitivity at the expense of specificity is beneficial clinically, particularly if MRI is to be used to avoid biopsy. To this end, the negative predictive value of mpMRI as a rule-out test in a systematic review of 48 studies (9,613 patients) was reported to be 82.4% for any cancer and 88.1% for Gleason ≥3+4 cancer [58]. This compares favourably to the current “gold standard” of systematic TRUS biopsy with an NPV of around

75% for clinically significant cancer [37]. It should be noted, however, that NPV is not intrinsic to the test itself and will vary depending on the cancer prevalence within the cohort. The same review reported NPV to range 68.4-100%, with a close inverse correlation to cancer prevalence of 13-74.7% [58], and Woo et al [52] noted a specificity for cancer detection of only 65% in studies where cancer prevalence was below 50%, but rising to 86% when >50%. In should also be noted that studies within the literature need to also be considered in terms of heterogeneity of the patient population, the gold standard employed (a surgical cohort will introduce bias such as operative suitability), and the exclusion criteria applied, such as presence of MRI artefact, haemorrhage or metalwork, meaning these may not necessarily be reflective of a standard clinical reporting list.

1.9 Chapter summary

In this chapter the epidemiology and work-up of prostate cancer has been introduced and discussed. It has been demonstrated that PSA testing has dramatically changed the profile of men presenting with prostate cancer which brings the risk of over-diagnosing and over-treating relatively indolent disease. Contrary to this there is a real risk of under-treatment due to the limitations of the traditional diagnostic pathway resulting in under-grading or missing tumours. Imaging with mpMRI has a potential role to play in mitigating these risks, with MRI having evolved from morphological staging to more accurate localisation of tumours and being used earlier in the diagnostic pathway.

However, mpMRI is a difficult technique to perform and interpret and has its own inherent limitations, highlighting the need for improvement in the existing sequences, or use of further novel functional sequences. Indeed, the most recent version of the PI-RADS

guidelines strongly supports the continued development of novel sequences. In the absence of reliable blood or urine markers biomarkers, realistically imaging offers the greatest potential for differentiating more aggressive, lethal cancers. To achieve this we need to image tumour function rather than structure, and currently PET imaging and novel MRI functional sequences offer the only means of adding incremental value to the existing clinical mpMRI sequences.

In this thesis, the optimisation of existing mpMRI sequences will be assessed and the issues of prostate tumour localisation and characterisation using novel functional imaging techniques assessed, with the ultimate aim of enabling more accurate prostate cancer stratification to inform management decisions.

1.10 References

[1] Siegel RL, et al. Cancer Statistics, 2017. CA Cancer J Clin. 2017; 67(1):7-30

[2] Cancer Research UK Cancer Statistics, 2016: http://www.cancerresearchuk.org/

Last accessed December 22, 2017

[3] Maddams J, et al. Projections of cancer prevalence in the United Kingdom, 2010– 2040. Br J Cancer 2012; 107:1195–1202

[4] Potosky AL, et al. The role of increasing detection in the rising incidence of prostate cancer. JAMA. 1995; 273:548-552

[5] Zarghami N, et al. Expression of the prostate specific antigen gene by lung tissue. Clin Cancer Res. 1997; 3(7):1201-6

[6] Grubb RL 3rd, et al. Prostate cancer screening in the Prostate, Lung, Colorectal and Ovarian cancer screening trial: update on findings from the initial four rounds of screening in a randomized trial. BJU Int. 2008;102(11):1524-30

[7] Thompson IM, et al. Operating characteristics of prostate-specific antigen in men with an initial PSA level of 3.0 ng/ml or lower. JAMA. 2005; 294(1):66-70

[8] Thompson IM, et al. Prevalence of prostate cancer among men with a prostate-specific antigen level < or =4.0 ng per milliliter. NEJM 2004;350:2239-46

[9] Moyer VA; US Preventive Services Task Force. Screening for prostate cancer: U.S. Preventive Services Task Force recommendation statement. Ann Intern Med. 2012; 157:120-134

[10] U.S. Preventive Services Task Force (USPSTF) [Internet]. Rockville: 2017 Available from: https://www.uspreventiveservicestaskforce.org/Page/Document/RecommendationStatementDraft/prostate-cancer-screening1

Last accessed December 22, 2017

[11] American Cancer Society: Cancer Facts and Figures 2013. Atlanta, Ga. Available at: https://www.cancer.org/research/cancer-facts-statistics/all-cancer-facts-figures/cancer-facts-figures-2017.html

Last accessed December 22, 2017

[12] Welch HG, Albertsen PC. Prostate cancer diagnosis and treatment after the introduction of prostate-specific antigen screening: 1986-2005. J Natl Cancer Inst. 2009; 101(19):1325-9

[13] Stamey TA, et al. The prostate specific antigen era in the United States is over for prostate cancer: what happened in the last 20 years? J Urol 2004; 172:1297-301

[14] Klotz L. Prostate cancer overdiagnosis and overtreatment. Curr Opin Endocrinol Diabetes Obes 2013; 20:204–209

[15] Surveillance, Epidemiology, and End Results (SEER) Program. SEER*Stat Database: Incidence-SEER 9 Regs Research Data with Delay-Adjustment, Malignant Only, Nov. 2015 Sub (1975-2013)

<Katrina/Rita Population Adjustment>-Linked To County Attributes-Total US, 1969-2014 Counties. Bethesda, MD: National Cancer Institute, Division of Cancer Control and Population Sciences, Surveillance Research Program, Surveillance Systems Branch; 2016

[16] Ficarra V, et al. Retropubic, laparoscopic, and robot-assisted radical prostatectomy: a systematic review and cumulative analysis of comparative studies. Eur Urol. 2009; 55(5):1037-63

[17] Locally advanced prostate cancer: effective treatments, but many adverse effects. Prescrire Int. 2013; 22(134):18-20, 22-3

[18] Mendenhall WM, et al. Erectile dysfunction after radiotherapy for prostate cancer. Am J Clin Oncol. 2009; 32(4):443-7

[19] Schröder FH, et al; ERSPC Investigators. Screening and prostate-cancer mortality in a randomized European study. N Engl J Med 2009; 360:1320–1328

[20] Independent UK Panel on Breast Cancer Screening. The benefits and harms of breast cancer screening: an independent review. Lancet 2012; 380:1778–1786

[21] **Barrett T**, Haider MA. The Emerging Role of MRI in Prostate Cancer Active Surveillance and Ongoing Challenges. AJR Am J Roentgenol. 2017; 208(1):131-139

[22] Wilt TJ, et al. Prostate Cancer Intervention versus Observation Trial (PIVOT) Study Group. Radical prostatectomy versus observation for localized prostate cancer. N Engl J Med. 2012; 367(3):203-13

[23] Hamdy FC, et al. 10-Year Outcomes after Monitoring, Surgery, or Radiotherapy for Localized Prostate Cancer. N Engl J Med. 2016; 375(15):1415-1424

[24] Wilt TJ, et al. Follow-up of Prostatectomy versus Observation for Early Prostate Cancer. N Engl J Med. 2017; 377(2):132-142

[25] Murphy G, et al. The expanding role of MRI in prostate cancer. AJR 2013; 201:1229–1238

[26] Kvåle R, et al. Concordance between Gleason scores of needle biopsies and radical prostatectomy specimens: a population-based study. BJU Int. 2009; 103(12):1647-54

[27] Hu Y, et al. A biopsy simulation study to assess the accuracy of several transrectal ultrasonography (TRUS)-biopsy strategies compared with template prostate mapping biopsies in patients who have undergone radical prostatectomy. BJU Int 2012; 110:812–820

[28] Gnanapragasam VJ, Burling K, George A, Stearn S, Warren A, **Barrett T**, et al. The Prostate Health Index adds predictive value to multi-parametric MRI in detecting significant prostate cancers in a repeat biopsy population. Sci Rep. 2016; 6:35364

[29] Wadhwa K, **Barrett T**, Kastner C. The post PSA era: new developments in biomarkers, imaging and biopsy techniques in prostate cancer detection. Trends in Urology & Men's Health. 2015; 6(4):25-29. DOI: 10.1002/tre.470

[30] Siddiqui MM, et al. Comparison of MR/ultrasound fusion-guided biopsy with ultrasound-guided biopsy for the diagnosis of prostate cancer. JAMA. 2015;313(4):390-7
[31] Lawrence EM, et al. The emerging role of diffusion-weighted MRI in prostate cancer management. Nat Rev Urol 2012; 9(2):94-101
[32] National Institute for Health and Care Excellence. Prostate cancer: diagnosis and treatment. Clinical guideline 175. https://www.nice.org.uk/guidance/cg175/
Last accessed May 12, 2017
[33] Schoots IG, et al. Magnetic resonance imaging-targeted biopsy may enhance the diagnostic accuracy of significant prostate cancer detection compared to standard transrectal ultrasound-guided biopsy: a systematic review and meta-analysis. Eur Urol. 2015; 68(3):438-50
[34] Kirkham AP, et al. Prostate MRI: who, when, and how? Report from a UK consensus meeting. Clin Radiol. 2013; 68(10):1016-23
[35] National Prostate Cancer Audit Fourth Year Annual Report – Organisation of Services and Analysis of Existing Clinical Data. London: The Royal College of Surgeons of England, 2017. https://www.npca.org.uk/annual-report-2017/
Last accessed January 4, 2018
[36] The London Cancer Alliance Best Practice Prostate Pathway, available at: http://www.londoncanceralliance.nhs.uk/media/109454/lca-best-practice-prostate-pathway-december-2013-updated-september-2015-.pdf
Last accessed January 4, 2018
[37] Ahmed HU, et al. Diagnostic accuracy of multi-parametric MRI and TRUS biopsy in prostate cancer (PROMIS): a paired validating confirmatory study. Lancet 2017; 389(10071): 815-22
[38] **Barrett T**. What is Multiparametric-MRI of the Prostate and Why Do We Need It? J Imag Int Rad. 2016; 1(2):1-5
[39] De Visschere PJ, et al. Multiparametric magnetic resonance imaging characteristics of normal, benign and malignant conditions in the prostate. Eur Radiol. 2017; 27(5):2095-2109
[40] Macura KJ, et al. Patterns of enhancement on breast MR images: interpretation and imaging pitfalls. Radiographics. 2006; 26(6):1719-34
[41] Hansford BG, et al. Dynamic Contrast-enhanced MR Imaging Curve-type Analysis: Is It Helpful in the Differentiation of Prostate Cancer from Healthy Peripheral Zone? Radiology. 2015; 275(2):448-57
[42] **Barrett T**, Turkbey B, Choyke PL. PI-RADS version 2: what you need to know. Clin Radiol. 2015; 70(11):1165-76
[43] Turkbey B, et al. Multiparametric 3T prostate magnetic resonance imaging to detect cancer: histopathological correlation using prostatectomy specimens processed in customized magnetic resonance imaging based molds. J Urol. 2011; 186(5):1818-24

[44] Mowatt G, et al. The diagnostic accuracy and cost-effectiveness of magnetic resonance spectroscopy and enhanced magnetic resonance imaging techniques in aiding the localisation of prostate abnormalities for biopsy: a systematic review and economic evaluation. Health Technol Assess. 2013; 17(20):vii-xix, 1-281

[45] National Prostate Cancer Audit First Year Annual Report – Organisation of Services and Analysis of Existing Clinical Data. London: The Royal College of Surgeons of England, 2014. http://www.npca.org.uk/wp-content/uploads/2014/11/NPCA-Annual-Report-FINAL-10_11_14.pdf *Last accessed May 12, 2017*

[46] Langer DL, et al. Intermixed normal tissue within prostate cancer: effect on MR imaging measurements of apparent diffusion coefficient and T2-sparse versus dense cancers. Radiology. 2008; 249(3):900-8

[47] Gaziev G, Wadhwa K, **Barrett T**, et al. Defining the learning curve for multiparametric magnetic resonance imaging (MRI) of the prostate using MRI-transrectal ultrasonography (TRUS) fusion-guided transperineal prostate biopsies as a validation tool. BJU Int. 2016; 117(1):80-6

[48] Puech P, et al. How are we going to train a generation of radiologists (and urologists) to read prostate MRI? Curr Opin Urol. 2015; 25(6):522-35

[49] Barentsz JO, et al; European Society of Urogenital Radiology ESUR prostate MR guidelines 2012. Eur Radiol. 2012; 22(4):746-57

[50] Weinreb JC, et al. PI-RADS Prostate Imaging - Reporting and Data System: 2015, Version 2. Eur Urol. 2016; 69(1):16-40

[51] Lemaitre L, et al. Dynamic contrast-enhanced MRI of anterior prostate cancer: Morphometric assessment and correlation with radical prostatectomy findings. Eur Radiol. 2009; 19:470–8

[52] Woo S, et al. Diagnostic Performance of Prostate Imaging Reporting and Data System Version 2 for Detection of Prostate Cancer: A Systematic Review and Diagnostic Meta-analysis. Eur Urol. 2017; 72(2):177-188

[53] **Barrett T**. MRI in prostate cancer diagnosis. RAD Magazine 2016; 488(42): 13-14

[54] Turkbey B, et al. Imaging localized prostate cancer: current approaches and new developments. AJR Am J Roentgenol. 2009; 192(6):1471-80

[55] de Rooij M, et al. Accuracy of multiparametric MRI for prostate cancer detection: a meta-analysis. AJR Am J Roentgenol. 2014; 202(2):343-51

[56] Rosenkrantz AB, et al. Interobserver Reproducibility of the PI-RADS Version 2 Lexicon: A Multicenter Study of Six Experienced Prostate Radiologists. Radiology 2016; 280:793–804

[57] Muller BG, et al. Prostate Cancer: Interobserver Agreement and Accuracy with the Revised Prostate Imaging Reporting and Data System at Multiparametric MR Imaging. Radiology. 2015; 277(3):741-50

[58] Moldovan, et al. What Is the Negative Predictive Value of Multiparametric Magnetic Resonance Imaging in Excluding Prostate Cancer at Biopsy? A Systematic Review and Meta-analysis from the European Association of Urology Prostate Cancer Guidelines Panel. Eur Urol. 2017; 72(2):250-266

Chapter 2: Optimising patient preparation for prostate mpMRI

2.1 Introduction

The difficulty of performing and interpreting prostate mpMRI has been highlighted and may related to patient, tumour, MR scanner and radiologist factors. Patient-related factors may be partially mitigated by ensuring patient preparation is optimised, however, the current version of the PI-RADS guidelines states that:

"At present, there is no consensus concerning all patient preparation issues." [1]

Nevertheless, three potentially controllable areas are highlighted:

- Use of antispasmodic agents to reduce motion artefact from bowel peristalsis
- Presence of air and/or stool in the rectum that may induce distortion on DWI
- Refraining from ejaculation prior to MRI to maximise seminal vesicle distention

In order to inform whether these factors impact on MR image quality we assessed the first two of these issues in a retrospective study of clinical mpMRI and the third by means of a prospective normal volunteer study.

2.2 Retrospective assessment of patient preparation on prostate multiparametric MRI image quality

A retrospective study was designed to assess for effect of both hyoscine butylbromide (HBB) and rectal loading on image quality [2, 3].

2.2.1 Study population

This single-institution retrospective study was approved as part of a prostate MRI service evaluation, with the need for informed consent for data analysis waived by the local ethics committee (study registration CUH/15/5126). The study comprised 173 patients undergoing 3T prostate MRI for any indication during a 12 month window, from March 2015 – February 2016. Exclusion criteria included previous treatment for prostate cancer and presence of pelvic metalwork.

HBB is routinely administration for prostate MRI unless clinically contraindicated. During the study period, approximately four times as many patients received HBB, therefore every fourth patient was selected to match numbers, with 87 in the HBB group and 86 in the non-HBB group. Patients in the HBB group were administered 20 mg of intravenous hyoscine butylbromide (Buscopan®, Boehringer, Ingelheim, Germany) on the table, immediately prior to scanning.

2.2.2 Magnetic Resonance Imaging

Patients underwent MRI at 3T (MR750, GE Healthcare) using a 32 channel phased array cardiac coil. Sequences included axial T1 weighted FSE (fast spin echo) pelvic images and

high resolution T2 weighted fast recovery FSE images of the prostate in the axial, sagittal, and coronal planes. T1 weighted parameters: TR/TE 561/11ms, FOV 24 × 24 cm, resolution 1.1 x 1.0mm. T2 weighted parameters: TR/TE 4273/102ms, FOV 22 x 22 cm, resolution 0.8 x 0.7mm, 1.5 signal averages. Axial diffusion-weighted imaging (DWI) was performed using a dual spin-echo planar pulse sequence: TR/TE 3775/70ms, FOV 28 × 28 cm, resolution 2.2 x 2.2mm, with 6 signal averages; b-values of 150, 750, 1400 and 2000 s/mm^2, with automated ADC maps. Axial 3D dynamic contrast-enhanced (DCE) images were acquired using a fast-spoiled gradient echo sequence (TR/TE 4.088/1.788ms; FOV 24 x 24 cm) with a temporal resolution of 7s. After 28s a bolus of Gadobutrol (Gadovist, Schering AG) was injected via a power injector at 3 mL/s (dose 0.1 mmol/kg) followed by a 25 mL saline flush at 3 ml/s. The axial T2-w, DWI and DCE sequences were spatially matched, with a 3 mm thickness and 0-mm gap.

2.2.3 Image analysis

Images were reviewed for image quality by two radiologists, blinded to the clinical details. Planimetry rectal volumes were derived using maximal axial and sagittal dimensions (anal canal to peritoneal reflection), and a subjective assessment of rectal distension was made using a 5-point Likert scale: 1 = no stool/gas, 2 = minimal, 3 = small amount, 4 = moderate, 5 = large amount of stool/gas. T2-weighted imaging was qualitatively assessed for image sharpness (based on the sharpness of the neurovascular bundle, seminal vesicles, and prostatic capsule compared to periprostatic fat) and motion artefact (ghosting or movement). DW image quality was scored on the highest b-value imaging (b=2000 s/mm^2) using a 5-point scale: poor = 1, suboptimal = 2, adequate = 3, above average = 4, excellent = 5. DWI was also assessed for artefact and distortion using 4-point scales; artefact: none = 1,

mild, not/mildly impacting diagnosis = 2, artefact moderately impacting diagnosis = 3, marked artefact/non-diagnostic = 4; distortion: none = 1, <5mm mismatch to T2WI = 2, ≥5 mm mismatch to T2WI *or* mild warping = 3, significant warping = 4. DCE images were assessed based on the number of corrupt data points, using a region-of-interest of ≥0.2cm^3 in normal appearing peripheral zone, and recording the number of corrupted data points from the contrast curve (defined as any >10%, between-point, signal intensity changes during the wash-out phase).

2.2.4 Statistics

The Shapiro-Wilks test was used to assess distributional normality. Non-parametric distributions were reported using median and inter-quartiles (IQ). Chi-square test (X2) was performed to compare MRI indications against HBB grouping. Wilcoxon signed ranked tests were performed to assess differences between binary criteria (T2 motion and sharpness) and the ordinal image quality scales. Fisher's exact test was used to compare targeted biopsy outcomes between groups of patients with differing rectal distension. Spearman's correlation was performed to assess the relationship between ordinal variables. A p-value <0.05 was defined as statistically significant. Weighted Cohen's Kappa was performed to assess inter-rater agreement using the following rules of thumb (0–0.20 = slight, 0.21–0.40 fair, 0.41–0.60 moderate, 0.61–0.80 substantial, and 0.81–1 almost perfect agreement). The statistical analysis was performed using R (version 3.1.1, The R Foundation for Statistical Computing, Vienna, Austria).

2.2.5 Results

A total of 173 patients were included with a median age of 65 years (mean 63.8, range 59 - 69) and a median PSA of 6.57 (mean 6.78, range 4.17 - 10.02).

2.2.5.1 Hyoscine butylbromide administration

Administration of HBB significantly improved the image quality of T2-weighted images compared to the non-HBB group (3.63±1.11 versus 2.84±0.899); p<0.001 (**Table 2.1**, **Figure 2.1**). The HBB group showed significantly less T2W motion and blur than the non-HBB group (23.0% and 51.7% versus 53.5% and 83.7%, respectively; p<0.001). However, there was no significant improvement in DWI/ADC image quality, distortion or artefact. There was a trend towards fewer corrupted DCE data points in the HBB group (2.47±2.44 versus 3.68±2.64), but this did not reach significance (p=0.052). There was no difference in rectal volumes or planimetry measurements between the groups (p = 0.141 - 0.206).

	HBB	No HBB	p-value
T_2W Imaging	(n=87)	(n=86)	
Image Quality (± SD)	3.63±1.11	2.84±0.89	<0.001*
Motion Present	20 (23.0%)	46 (53.5%)	<0.001*
Blur Present	45 (51.7%)	72 (83.7%)	<0.001*
DWI	(n=87)	(n=86)	
Image Quality (± SD)	3.53±1.03	3.27±0.91	0.091
Distortion (± SD)	2.20±0.93	2.43±0.90	0.078
Artefact (± SD)	1.60±0.56	1.64±0.59	0.692
ADC			
Image Quality (± SD)	3.74±1.07	3.57±0.98	0.220
DCE	(n=34)	(n=33)	
Corrupt data points (± SD)	2.47±2.44	3.68±2.64	0.052

Table 2.1: Image Quality scoring comparing hyoscine N-butybromide versus non-HBB groups for different MRI sequences. * Denotes a significant difference. SD = standard deviation.

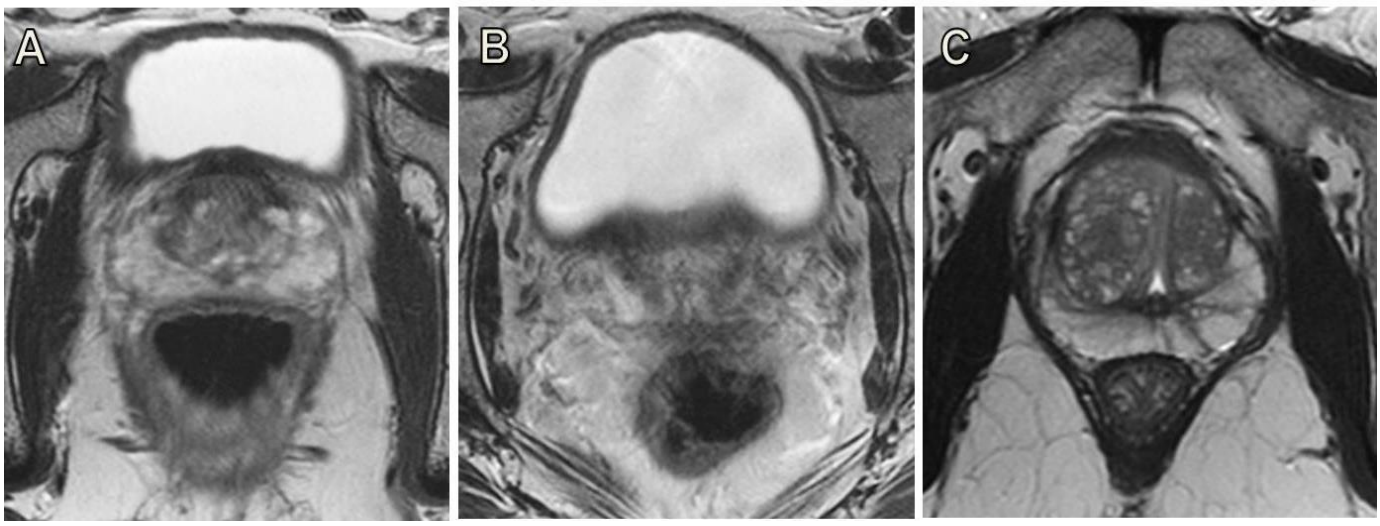

Figure 2.1: MR image quality relating to HBB administration. (A) Image blur on T2WI: 57 year old, Gleason 3+3 disease on active surveillance, PSA 2.7 ng/ml. Indistinct capsule and prostatic zone interface. No HBB given due to history of cardiac arrythmia. (B) Image motion on T2WI: 58 year old, PSA 5.3, MRI pre-biopsy. HBB not given due to lack of medical cover. Ghosting artefact noted within the bladder. (C) T2W image of good quality: 64 year old, PSA 5.1, MRI performed pre-biopsy, HBB given. T2W image quality rated as 5/5 by both readers, with no blur and no motion.

2.2.5.2 Rectal loading

The inter-reader agreement for subjective scoring of rectal loading expressed using Cohen's kappa coefficient was 0.819 indicating excellent agreement between the two readers. A significant correlation was shown between increased rectal distension and both reduced DW image quality ($r = -0.628$, $p<0.001$), and increased DW image distortion ($r=0.814$, $p<0.001$). Increased rectal distension led to increased motion artefact on T2 ($p = 0.0096$), but there was no effect on DCE image quality (**Figure 2.2**). There was a strong correlation between subjective scoring of rectal loading and objectively measured AP diameter ($r = 0.882$) and rectal volume ($r = 0.82$), $p<0.001$

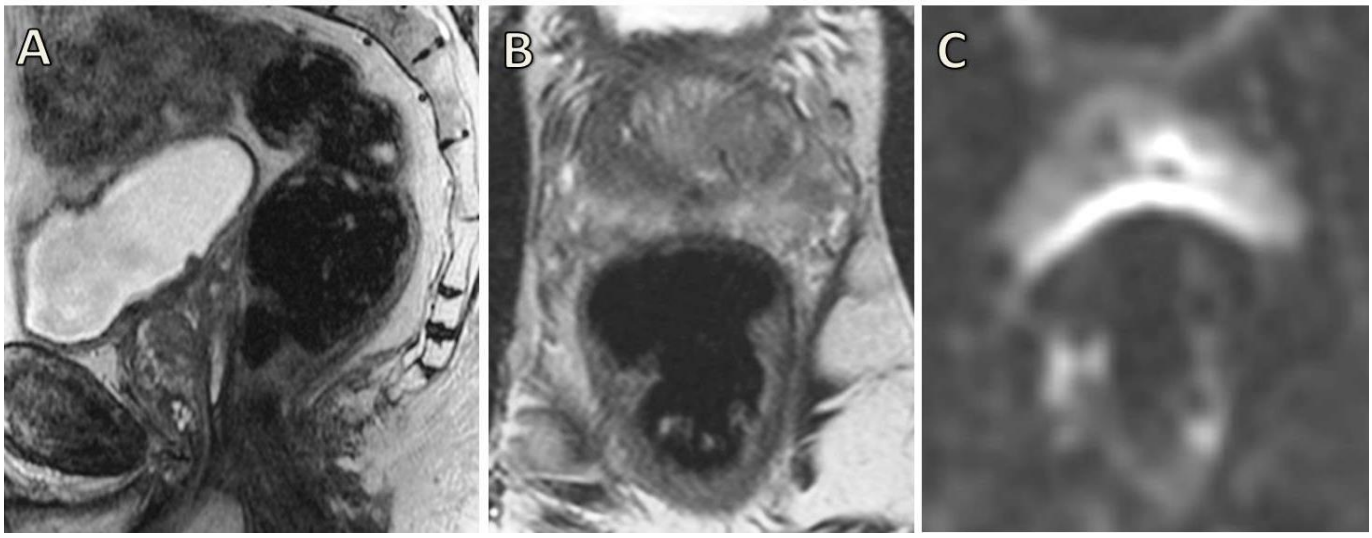

Figure 2.2: Marked rectal loading with significant effect on T2 and DW image quality. 66 year-old, PSA 5.63, MRI performed pre-biopsy. Subjective scores of severe rectal loading (A). B: T2 imaging scored as loss of sharpness and presence of motion artefact. C: DWI shows significant warping.

2.2.6 Discussion

The results of our study show that the quality of T2W images was significantly improved patients receiving hyoscine butylbromide. In addition, increasing rectal distension has been shown to have a significant negative effect on the quality of both T2W and DW images.

The results for HBB administration improving T2W image quality are concordant with the study by Kier et al at 1.5T showing significantly less artefacts when the glucagon was given as an anti-spasmotic agent (7% vs. 45%) [4]. Similarly, Johnson et al reported better visualization of the prostate in approximately 45% of patients after HBB administration at 1T [5]. Roethke et al demonstrated a non-significant effect of HBB on the quality of T2W images in 70 patients, scanned at 3T without an ERC [6]. However, despite not reaching significance, they demonstrated an improvement for all image quality categories and a reduction in artefacts with HBB administration. Conversely, a study by Wagner et al did not demonstrate a significantly improved visualization of the prostate at 1.5T MRI using an endorectal coil (ERC), and argued the low position of the prostate, remote from the small bowel, reduced the effects of peristalsis [7]. However, an endorectal coil is not routinely used in most centres performing prostate MRI. The effect of DCE acquisition is likely to be more complicated, but the lower TR employed and *k*-space sampling strategy used will help reduce intra-acquisition motion artefact. Interestingly, our study shows that HBB has a significant effect on the anatomical but not on the functional sequences. The Echo planar imaging (EPI) readout of DWI typically samples all of *k*-space in one to two TR periods, dependent on the number of shots, which acts to reduce the effects of motion. DWI The timing of the DCE acquisition, approximately 30 mins post HBB injection, means the effects of HBB may well have worn off, negating any HBB-related differences between the groups.

There are a limited number of previously studies looking at the issue of rectal distension and prostate MRI quality. Lim et al [8] showed no improvement in the quality of DWI, T2W or DCE prostate images in a retrospective study of 28 patients receiving a cleansing enema prior to imaging. Despite showing a significant correlation of stool volume to motion artefact on T2 and the presence of less stool in the enema group, there was no significant difference to a control group with no enema. Of note however, only a minority of patients (16%) in the non-enema group had moderate or large amounts of stool, compared to 38.2% in our cohort. Another confounding factor may be the introduction of air post-enema, as the induced susceptibility artefact may have counteracted the effect of stool distension. Classical susceptibility artefact occurs at the interface of two substances which have different magnetic susceptibilities, in this case the interface of air within the rectum and the prostate. The echo planar readouts used within diffusion weighted imaging are particularly susceptible to magnetic field in-homogeneities which are prevalent at air tissue boundaries due to accumulated phase errors in the readout.

2.2.7 Limitations

The study has some limitations, including its retrospective nature. Future prospective studies would ideally allow paired analysis comparing patients pre- and post-HBB, for direct comparison. Cancer detection rates were not directly assessed as part of this study as the main purpose was to evaluate image quality, this could form the basis of future work, in order to better determine whether HBB administration and/or rectal distension have a clinical impact.

2.2.8 Conclusions

In terms of patient preparation, these findings support the use of spasmolytic agents to improve T2 image quality and suggest measures to limit rectal loading will help to optimise DW image quality and limit motion artefact on T2 weighted-imaging. Clearly patient-related factors can be controlled and optimised.

2.3 The longitudinal effect of ejaculation on seminal vesicle fluid volume and whole prostate ADC as measured on prostate MRI

2.3.1 Background

A primary purpose of mpMRI remains staging of prostate cancer, and determining seminal vesicle (SV) involvement (T3b disease) has implications for risk stratification, management and long-term prognosis. Optimal assessment of T3b disease is thought to require maximal SV distension [9] and some centres recommend that patients refrain from ejaculation for 3 days prior to MRI to achieve this [10, 11]. However, evidence for this practice is lacking, with only one prospective MRI study documenting SV volume change in relation to ejaculation, with a 41% mean reduction immediately post-ejaculation [12]. Scanning at this time point is not representative of a clinical list and it may be that fluid replacement occurs relatively rapidly. A normal volunteer study was therefore designed to prospectively investigate the longitudinal effect of ejaculatory abstinence on MRI measured seminal vesicle volume and whole prostate ADC over consecutive days [13].

2.3.2 Methods

15 healthy male volunteers (mean age 35.9 years, range 27-53) were included in this prospective, institutional review board-approved study (CUH/15/YH/0570). MR imaging was performed on 4 consecutive days. The subjects were instructed to refrain from ejaculation for ≥3 days prior to first MRI, to perform ejaculation after scan 1 and prior to scan 2, then abstain from ejaculation until completion of the study. Scans 2, 3, and 4 were therefore performed 1-24, 48, and 72 hours post-ejaculation, respectively.

2.3.3 Magnetic Resonance Imaging

MRI was performed on a 3T MR750 magnet (General Electric Healthcare, Waukesha, USA) using a 32-channel phased array cardiac coil. Sequences: high resolution axial T2 weighted fast recovery fast spin echo imaging, TR/TE 3663/102 ms field-of-view (FOV) 22x22 cm, 3/0 mm slice thickness/gap, in-plane resolution 0.85x0.57 mm, and 3 signal averages; sagittal T2 cube sequence, 1 mm slice thickness with no gap, in-plane resolution 1.0x0.8 mm. Axial DWI acquired as a dual spin-echo planar pulse sequence with TR/TE 3775/70ms, FOV 28×28 cm, resolution 2.2x2.2 mm, 6 signal averages and b-values of 150/750/1000/1400 s/mm^2 with automated ADC maps generated.

2.3.4 MR Segmentation

Seminal vesicle (SV) and prostate volumes were calculated using whole volume segmentation on T2-weighted images using in-house software programmed in Matlab (Mathworks, MA, USA). Whole gland ADC measurements were acquired after outlining the prostate using the relevant T2-weighted axial sequence as an anatomical reference. Outlines were drawn in a random order, blinded to the timing pre or post-ejaculation. For SV volume, a separate calculation was made of fluid volume by excluding the wall volume which is expected to remain constant, but contributes proportionately more to the overall volume when the seminal vesicles are collapsed or under-filled. A thresholding method was applied and set to a fraction (f) of the maximum pixel intensity (S_{max}) calculated as the 95% percentile in the SV ROI intensity histogram. The maximum signal in the centre slice was found and the threshold set to $S > (S_{max} \times f)$, where the fraction f was set at 0.7 or 0.8 (depending on the presence of motion-induced 'blurring'); **Figure 2.3**.

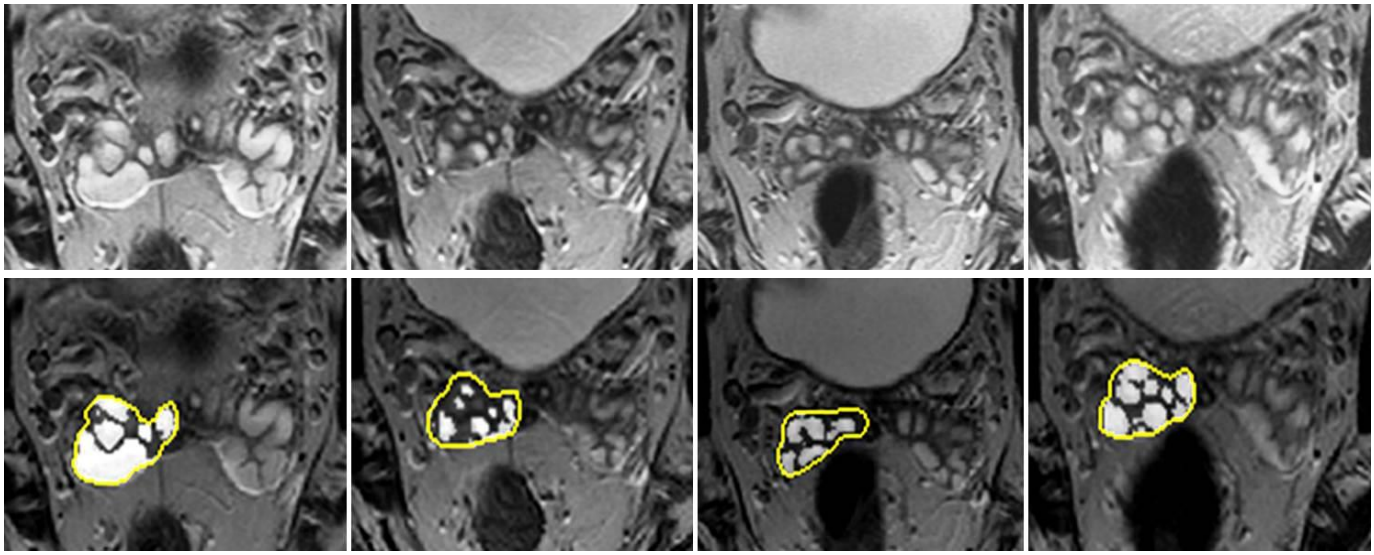

Figure 2.3: Example of seminal vesicle volume change over time. Top row: Axial T2-weighted MR imaging performed at baseline (minimum 3 days post-ejaculation), and post ejaculation on days 1, 2 and 3. Top row: subject 5 (aged 27) shows significant reduction in volume from a baseline of 9.7 cm^3 to 3.6 cm^3 on day 1 and subsequently 4.7 cm^3, 6.9 cm^3 on days 2 and 3, respectively. Bottom row: Manual regions-of-interest (yellow) were drawn outlining SVs on all slices for segmentation. To remove the SV wall component, the maximum signal in the central outlined was identified and a threshold applied for inclusion of pixels >($S_{max} \times f$).

2.3.5 Statistics

A linear mixed effects model was fitted to the seminal vesicle fluid volume and whole prostate ADC observations. Each model included fixed effects for the time of the observation (baseline, day 1, day 2 or day 3) and random effects for each individual to account for correlation within individuals. A log transform was applied to the data to ensure homoscedastic error variance. Spearman's correlation was performed to assess any relationships. Statistical analyses were performed using Stata®14 (StataCorp LP, Texas, USA). P-values of <0.05 were considered to be statistically significant.

2.4 Results

All 15 volunteers completed each of the 4 scans at the appropriate time. For one subject, there was a technical failure of diffusion-weighted imaging on the day-1 scan and the results were excluded from the ADC analysis.

2.4.1 Volume measurements

The mean prostate volume measured on the final scan was 22.45 cm^3 (median 23.28 cm^3, range 13.04 - 31.21 cm^3). There was no change in whole gland prostate volume between the 4 studies, baseline: 22.46 cm^3, day-1: 22.47 cm^3, day-2: 22.53 cm^3, and day-3: 22.45 cm^3 (P = 0.89 - 0.99).

There was no significant difference in overall average volume of the right (6.35 cm^3) and left (6.13 cm^3) seminal vesicles, with difference ranging from 0.21 – 2.17 cm^3; P = 0.50. As expected, there was no change in SV wall volume between the studies, baseline: 6.31 cm^3, day-1: 6.61 cm^3, day-2: 6.59 cm^3, and day-3: 6.65 cm^3; P = 0.38 - 0.49.

The average seminal vesicle fluid volume on the final scan was 5.82 cm^3 (median 5.25 cm^3, range 2.1 - 14.52 cm^3). There was a reduction in SV fluid volume in 13/15 subjects from baseline to day-1. SV fluid volume significantly reduced from an average of 6.45 cm^3at baseline to 4.80 cm^3at day-1 (25.6% reduction, P < 0.001) and to 5.28 cm^3 at day-2 (18.1% reduction, P = 0.002). There was a significant increase in volume from 4.80 cm^3at day-1 to 5.82 cm^3 at day-3 post-ejaculation (35.1% increase, P = 0.006); **Figure 2.4, Table 2.1**.

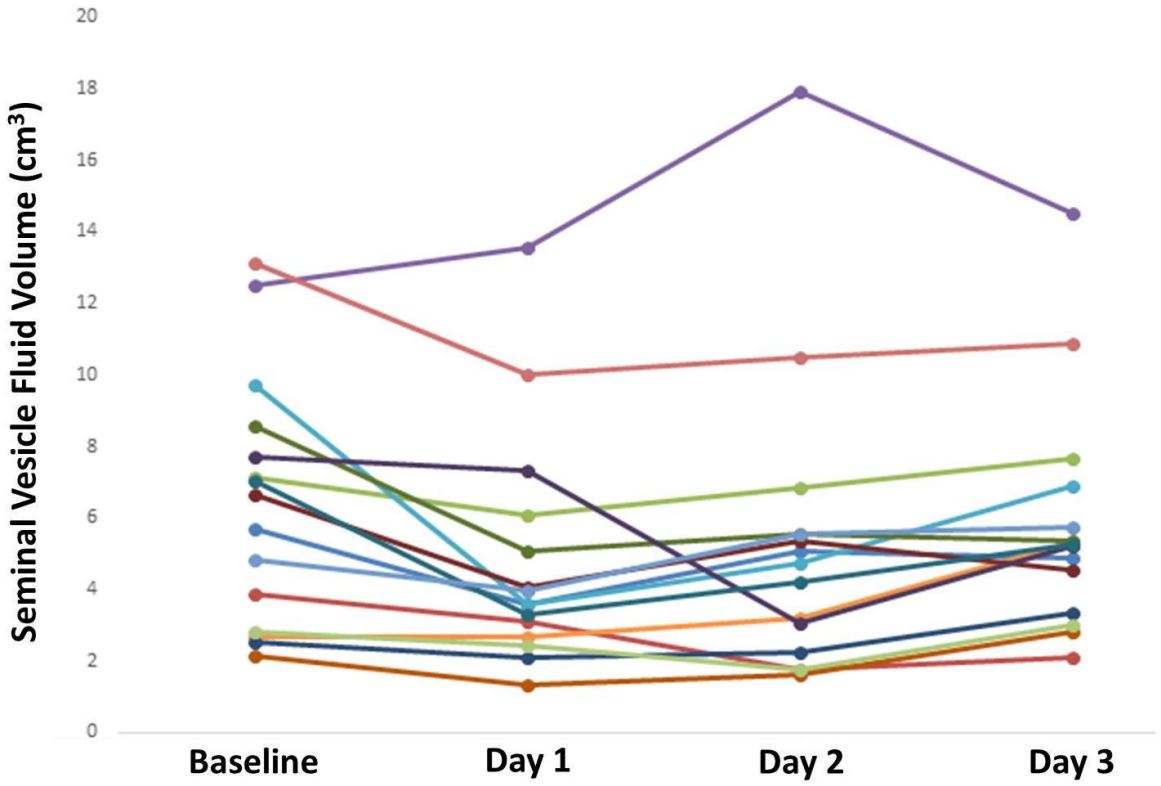

Figure2.4: Seminal vesicle fluid volumes between each of the 4 scans. Fluid volumes measured on T2-weighted images for all 15 normal volunteers at baseline and at 1, 2, and 3 days post-ejaculation.

Comparison	Absolute change (cm^3)	Percentage change (%)	p-value
Baseline vs day 1	-1.65 (1.85)	-25.1 (19.9)	**<0.001***
Baseline vs day 2	-1.18 (2.5)	-19.5 (29.3)	**0.002***
Baseline vs day 3	-0.63 (1.86)	-9.77 (38.0)	0.38
Day 1 vs Day 2	0.48 (1.81)	10.0 (30.2)	0.59
Day 1 vs Day 3	1.02 (1.33)	21.3 (43.3)	**<0.006***
Day 2 vs Day 3	0.55 (1.41)	10.2 (34.0)	**0.022***

Table 2.2: Comparison of mean Seminal Vesicle fluid volumes between studies. Standard deviation in parentheses; * $P < 0.05$, denoting significance.

2.4.2 Quantitative whole gland ADC measurements

There was a reduction ADC value in 10 of 14 subjects from baseline to day-1, with a significant mean reduction from 1.105 x 10^{-3} mm^2/s at baseline to 1.056 x 10^{-3} mm^2/s at day-2 (4.3% reduction, P = 0.009). There was a general trend for ADC values to subsequently increase from day 2 to 3, but this was not significant (**Figure 2.5, Table 2.2**).

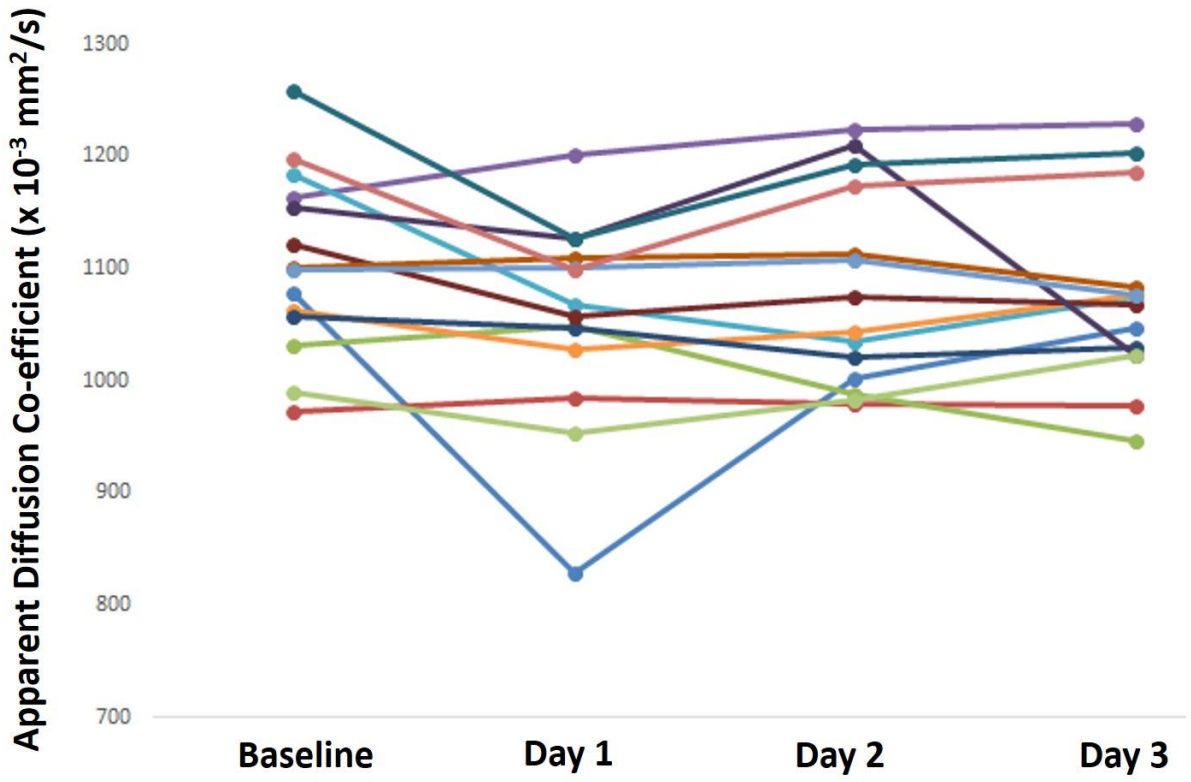

Figure 2.5: Whole-gland prostate ADC values between each of the 4 scans. ADC values for 14 normal volunteers at baseline and at 1, 2, and 3 days post-ejaculation.

Comparison	Absolute change (10^{-3} mm^2/s)	Percentage change (%)	p-value
Baseline vs day 1	-0.049 (0.078)	-4.29 (6.97)	**0.009***
Baseline vs day 2	-0.023 (0.054)	-2.06 (4.68)	0.20
Baseline vs day 3	-0.031 (0.054)	-2.66 (4.77)	0.10
Day 1 vs Day 2	0.026 (0.059)	2.67 (6.44)	0.15
Day 1 vs Day 3	0.019 (0.082)	2.19 (8.84)	0.28
Day 2 vs Day 3	-0.007 (0.058)	-0.77 (5.69)	0.71

Table 2.3: Comparison of mean whole prostate ADC values between scans. Standard deviation in parentheses; * $P < 0.05$, denoting significance.

2.5 Discussion

This study demonstrates the longitudinal MR measurements of seminal vesicle fluid volume following ejaculatory abstinence for the first time. There was a significant reduction in SV fluid volume within a day of ejaculation and maintained at day-2. This was confirmed by an increase in volume on successive days post-ejaculation, with significantly higher volumes observed at day-3 compared to day-1 and 2, suggesting a minimum 3-day period of abstinence is required for maximal SV distension. A similar effect was seen for ADC values, with a significant reduction in values at day-1 post-ejaculation.

Although many centres recommend abstinence from ejaculation prior to prostate MRI, evidence to support this practice is lacking. The rationale may be based on practice for the investigation of male fertility, where abstinence of 2-7 days is recommended for sperm analysis [14]. Semen volume (by 24%) and sperm density are reduced in men with abstinence of only 1 day compared to ≥4 days [15, 16]. It should be noted that although seminal vesicle fluid makes up 60-85% of the ejaculate [17], there are also contributions from the prostate gland (15-30%), testis (<5%) and bulbourethral glands (1-5%), thus ejaculate volume alone may not provide an accurate indication of changes in SV volume. Early work using vesiculography [18] and ultrasound [19, 20] and subsequently confirmed by a more recent MRI study [6] showed 30-40% reductions in seminal vesicle volume immediately post-ejaculation. However, these studies are not representative of an out-patient MR patient population. A more recent study demonstrated lower SV volumes in patients imaged less than 3 days post last ejaculation, compared to more than 3 days [21]. This study only looked at the binary cut-off of 3-days and was additionally limited by use of SV planimetry measurements rather than image-segmentation volumetry. Furthermore, the

same patients were not directly compared, and inter-patient variation, in which SV length may vary up to 11-fold [22], may therefore have affected their results.

A significant reduction was demonstrated in whole prostate ADC measurements within 24 hours of ejaculation, and a non-significant increase in ADC was seen between days 2 and 3. This is consistent with earlier work in the immediate post-ejaculatory phase [12]. ADC reduces with increasing Gleason grade [23, 24], which partly relates to loss of fluid in the glandular lumen [25]; higher grade tumours also have also been shown to have a reduced luminal space [26]. The prostate gland contributes a small amount of fluid to the ejaculate [17] and although we did not demonstrate any appreciable change in prostate volume between studies, this fluid loss may be sufficient to have a dehydrating effect on the gland fluid, and thus reduce the ADC value. The effect of ejaculatory time on prostate ADC values is potentially of more clinical significance than the effect on SV volume, as this may affect lesion conspicuity and assessment, particularly in the PZ where DWI is the key mpMRI sequence. Standardization of patient preparation prior to prostate MRI may help to reduce inter-patient variations in ADC measurements and improve quantitative analysis, as well as addressing intra-patient variation in the context of follow-up in patients on active surveillance programs. Morgan et al [27] suggested that in patients on active surveillance, a reduction in the whole-gland ADC of >10% was associated with progression to radical treatment and that non-progressors also showed a less marked decrease in ADC. However, in a small cohort of prostate cancer patients, Fedorov A, et al [28] showed that ADC repeatability varied up to 40% for small lesions that would be appropriate for AS, which would call into question the use of the parameters quantifiably.

We did not look at the question of dynamic contrast-enhanced MRI, as multiple repeat Gadolinium injections in normal volunteers could not be justified, however, it is possible that this may also be affected by post-ejaculatory status, with a previous ultrasound study showing ejaculation affected the clinical assessment of prostatitis by increasing prostatic blood flow for at least 24 hours [29].

2.5.1 Limitations

There were several limitations to the study. The study population was a small cohort of healthy volunteers who were of a younger age than typical patients with prostate cancer. It has been demonstrated that SV volume in healthy patients decreases after the age of 60 years [30]; however, this may be partially off-set by an increase in volume in patients with BPH [31]. Although these results should hold regardless of baseline volume, it is unclear whether they would be affected by an underlying disease process, or indeed whether diagnostic interpretation would be hindered. It has been suggested that the replenishment of seminal fluid in younger patients is more rapid and therefore the effects of abstinence may be less apparent [21]; while there is no direct evidence for this, it would suggest that the results demonstrated here in young volunteers would be more marked if repeated in an older age group, and further strengthens the argument for a period of abstinence prior to scanning. Larger studies in patients with prostate cancer, ideally incorporating age-appropriate healthy controls, would serve to overcome these limitations and would also help address whether the observed variation in ADC values affects lesion conspicuity and detection.

2.5.2 Conclusions

In conclusion, the longitudinal effect of ejaculation on seminal vesicle volume as measured by MR imaging has been demonstrated in a young cohort without prostate cancer. Seminal vesicle volume is significantly reduced at days 1 and 2 post-ejaculation and increases to day-3. Whole-gland prostate ADC values also significantly reduced at day-1 post-ejaculation. The results require confirmation in an age-appropriate cohort, but support the rationale for a 3-day period of abstinence from ejaculation prior to diagnostic prostate MRI.

2.6 Chapter Summary

It is apparent that preparation and patient-related factors can affect the quality of images and attempts should therefore be made to control these in order to optimise the MRI study and outcomes. The effect of ejaculatory abstinence on whole-gland ADC is potentially more clinically significant than SV volume as this may affect lesion conspicuity and detection, whilst T3b involvement can be assessed by other secondary signs such as asymmetry or bulging and focal areas of enhancement and/or restricted diffusion. However, further testing of lesion detection is needed in the clinical MRI setting. A local (unpublished) questionnaire study (ethics: CUH/16/WM/0253) of 185 patients undergoing prostate MRI indicated that only 22/185 (11.9%) of patients had ejaculated within the preceding 24 hours, with the majority (113/185; 61.1%) observing an ejaculatory free period of ≥72 hours. Therefore, even if ADC is affected within one day of ejaculation this may be less of a clinical issue in this patient context, with the majority (almost 90%) having not ejaculated within this period, even without any prior instruction.

2.7 References

[1] Weinreb JC, et al. PI-RADS Prostate Imaging - Reporting and Data System: 2015, Version 2. Eur Urol. 2016; 69(1):16-40

[2] Caglic I, Hansen NL, Slough RA, Patterson AJ, **Barrett T**. Evaluating the effect of rectal distension on prostate multiparametric MRI image quality. Eur J Radiol. 2017; 90(5):174-80

[3] Slough R, Caglic I, Hansen N, Patterson A, **Barrett T**. Effect of hyoscine butylbromide on prostate multiparametric MRI anatomical and functional image quality. Clin Radiol. 2017 Aug 10. pii: S0009-9260(17)30388-4. doi: 10.1016/j.crad.2017.07.013.

[4] Kier R, et al. Fast Spin-Echo MR Images of the Pelvis Obtained with a Phased- Array Coil: Value in Localizing and Staging Prostatic Carcinoma. AJR Am J Roentgenol. 1993; 161:601-6

[5] Johnson W, et al. The value of hyoscine butylbromide in pelvic MRI. Clin Radiol. 2007; 62:1087-93

[6] Roethke MC, et al. Prostate magnetic resonance imaging at 3 Tesla: Is administration of hyoscine-N-butyl-bromide mandatory? World J Radiol. 2013; 5:259-63

[7] Wagner M, et al. Effect of butylscopolamine on image quality in MRI of the prostate. Clin Radiol. 2010; 65:460-4

[8] Lim C, et al. Does a cleansing enema improve image quality of 3T surface coil multiparametric prostate MRI? J Magn Reson Imaging 2015; 42:689-97

[9] de Rooij M, et al. Accuracy of Magnetic Resonance Imaging for Local Staging of Prostate Cancer: A Diagnostic Meta-analysis. Eur Urol. 2016; 70(2):233-245

[10] Bloch BN, et al. The role of magnetic resonance imaging (MRI) in prostate cancer imaging and staging at 1.5 and 3 Tesla: the Beth Israel Deaconess Medical Center (BIDMC) approach. Cancer Biomark. 2008; 4(4-5):251-262

[11] Sankineni S, et al. Functional MRI in prostate cancer detection. Biomed Res Int. 2014:590638

[12] Medved M, et al. MR imaging of the prostate and adjacent anatomic structures before, during, and after ejaculation: qualitative and quantitative evaluation. Radiology. 2014; 271(2):452-460

[13] **Barrett T**, Tanner J, Gill AB, Slough RA, Wason J, Gallagher FA. The longitudinal effect of ejaculation on seminal vesicle fluid volume and whole prostate ADC as measured on prostate MRI. Eur Radiol. 2017; 27(12):5236-5243[14] WHO laboratory manual for the examination and processing of human semen. 5th ed. WHO Laboratory Manual for the Examination and Processing of Human Semen. Geneva: WHO Press; 2010

[15] Marshburn PB, et al. Influence of ejaculatory abstinence on seminal total antioxidant capacity and sperm membrane lipid peroxidation. Fertil Steril. 2014; 102(3):705-710

[16] De Jonge C, et al. Influence of the abstinence period on human sperm quality. Fertil Steril. 2004; 82(1):57-65

[17] Lundquist F. Aspects of the biochemistry of human semen. Acta Phys Scand. 1950; 19(66):53-78

[18] Ichijo S, et al. Vasoseminal vesiculography before and after ejaculation. Urol Int. 1981; 36:35-45
[19] Fuse H, et al. Evaluation of seminal vesicle characteristics by ultrasonography before and after ejaculation. Urol Int. 1992; 49(2):110-113
[20] Lotti F, et al. Seminal vesicles ultrasound features in a cohort of infertility patients. Hum Reprod. 2012; 27(4):974-982
[21] Kabakus IM, et al. Does Abstinence From Ejaculation Before Prostate MRI Improve Evaluation of the Seminal Vesicles? AJR Am J Roentgenol. 2016; 207:1-5
[22] Gofrit ON, et al. The dimensions and symmetry of the seminal vesicles. J Robot Surg. 2009; 3(1):29-33
[23] Hambrock T, et al. Relationship between apparent diffusion coefficients at 3.0-T MR imaging and Gleason grade in peripheral zone prostate cancer. Radiology 2011; 59:453–461
[24] Donati OF, et al. Prostate cancer aggressiveness: assessment with whole-lesion histogram analysis of the apparent diffusion coefficient. Radiology 2014; 271:143–152
[25] Epstein JI, et al; ISUP Grading Committee. The 2005 International Society of Urological Pathology (ISUP) Consensus Conference on Gleason Grading of Prostatic Carcinoma. Am J Surg Pathol 2005; 29(9):1228–1242
[26] Lawrence EM, Warren AY, Priest AN, **Barrett T**, et al. Evaluating Prostate Cancer Using Fractional Tissue Composition of Radical Prostatectomy Specimens and Pre-Operative Diffusional Kurtosis Magnetic Resonance Imaging. PLoS One. 2016; 11(7):e0159652
[27] Morgan VA, et al. Diffusion weighted magnetic resonance imaging for monitoring prostate cancer progression in patients managed by active surveillance. Br J Radiol 2011; 84:31-37
[28] Fedorov A, et al. Multiparametric Magnetic Resonance Imaging of the Prostate: Repeatability of Volume and Apparent Diffusion Coefficient Quantification. Invest Radiol. 2017; 52(9):538-546
[29] Keener TS, et al. Prostate vascular flow: the effect of ejaculation as revealed on transrectal power Doppler sonography. AJR Am J Roentgenol 2000; 175(4): 1169-1172
[30] Terasaki T, et al. Seminal vesicle parameters at 10-year intervals measured by transrectal ultrasonography. J Urol. 1993; 150(3):914-916
[31] Hayakawa T, et al. Significant changes in volume of seminal vesicles as determined by transrectal sonography in relation to age and benign prostatic hyperplasia. Tohoku J Exp Med. 1998; 186(3):193-204

Chapter 3: Evaluation of Magnetization Transfer and Diffusion Kurtosis MR imaging for prostate cancer detection in a re-biopsy population

3.1 Introduction

Having described the utility but limitations of standard clinical sequences used in mpMRI of the prostate, this chapter looks at the potential use of further functional sequences to aid cancer detection. The most recent version of the PI-RADS guidelines strongly supports the continued development of novel sequences, including diffusion tensor (DTI), diffusional kurtosis imaging (DKI), multiple b-value assessment of fractional ADC, and intravoxel incoherent motion (IVIM) [1]. In this study diffusion kurtosis imaging (DKI) and magnetization transfer imaging (MTI), two novel MR sequences that do not require administration of any exogenous contrast agents were assessed.

Definitive pre-treatment diagnosis of prostate cancer still relies on the results of systematic transrectal ultrasound (TRUS) guided biopsies of the prostate, the limitations of which have already been described. In patients with an initial negative biopsy but continued clinical suspicion of prostate cancer, national guidelines in the UK recommend further assessment to exclude or confirm the presence of tumour [2]. Additionally, TRUS-biopsy may misclassify lesions as low grade due to sampling error, necessitating a repeat biopsy. Prostatic biopsy using MR targeting in such patients has been shown to improve pre-treatment risk stratification by reducing sampling error [3]. This re-biopsy population of patients was identified as potentially benefiting from improved MRI sequences, and formed the study cohort. The route of repeat biopsy chosen was fused US-MRI targeted biopsy via a transperineal approach.

3.1.1 Transperineal prostatic biopsy

Biopsies performed using the transperineal approach are often considered in re-biopsy patients and offer certain advantages over standard TRUS-guided biopsy. Transperineal ultrasound (TPUS) guided biopsy utilizes a sterile technique, reducing the risk of biopsy associated infection, and also has an increased ability to detect cancers located in the anterior and apical regions of the prostate, two areas that are frequently under sampled through TRUS biopsy. Factors limiting its use include increased time, limited availability of equipment, and the need for general anaesthesia [4]. Further improvements in pre-biopsy MR imaging by incorporation of newer and more novel techniques could enable more accurate targeting of TPUS biopsy, minimising the cores acquired and thus help to limit some of the disadvantages of the technique by reducing morbidity, surgical time, and the cost of the procedure. In theory initial TRUS biopsy could be replaced by TPUS in certain patients with suspicion for anterior or apical tumours, reducing the overall rate of negative biopsies.

3.1.2 Diffusion Kurtosis Imaging

Conventional diffusion-weighted imaging quantifies water diffusion within tissue by acquiring a number of b-value images at different gradient strengths and then applying a mono-exponential mathematical model to the signal decay in order to produce an apparent diffusion coefficient (ADC) map. The mono-exponential model assumes that the diffusion of water molecules follows a Gaussian (normal) distribution. However, while this assumption may hold for pure liquids, it is not true for complex biological tissues with compartments and barriers to diffusion [5]. At lower b-values with short measurement times, most molecules will not have enough time to reach cell membranes or other boundaries, and a

mono-exponential model may suffice. However, at higher b-values, with increasing diffusion time, a higher proportion of molecules strike the boundaries, resulting in a deviation of diffusion from normal Gaussian behaviour [5, 6]; **Figure 3.1**. Diffusion kurtosis imaging (DKI) is a form of diffusion-weighted imaging that exploits the degree to which water diffusion in tissues differs from what would be expected under a normal (Gaussian) distribution of displacements [7].

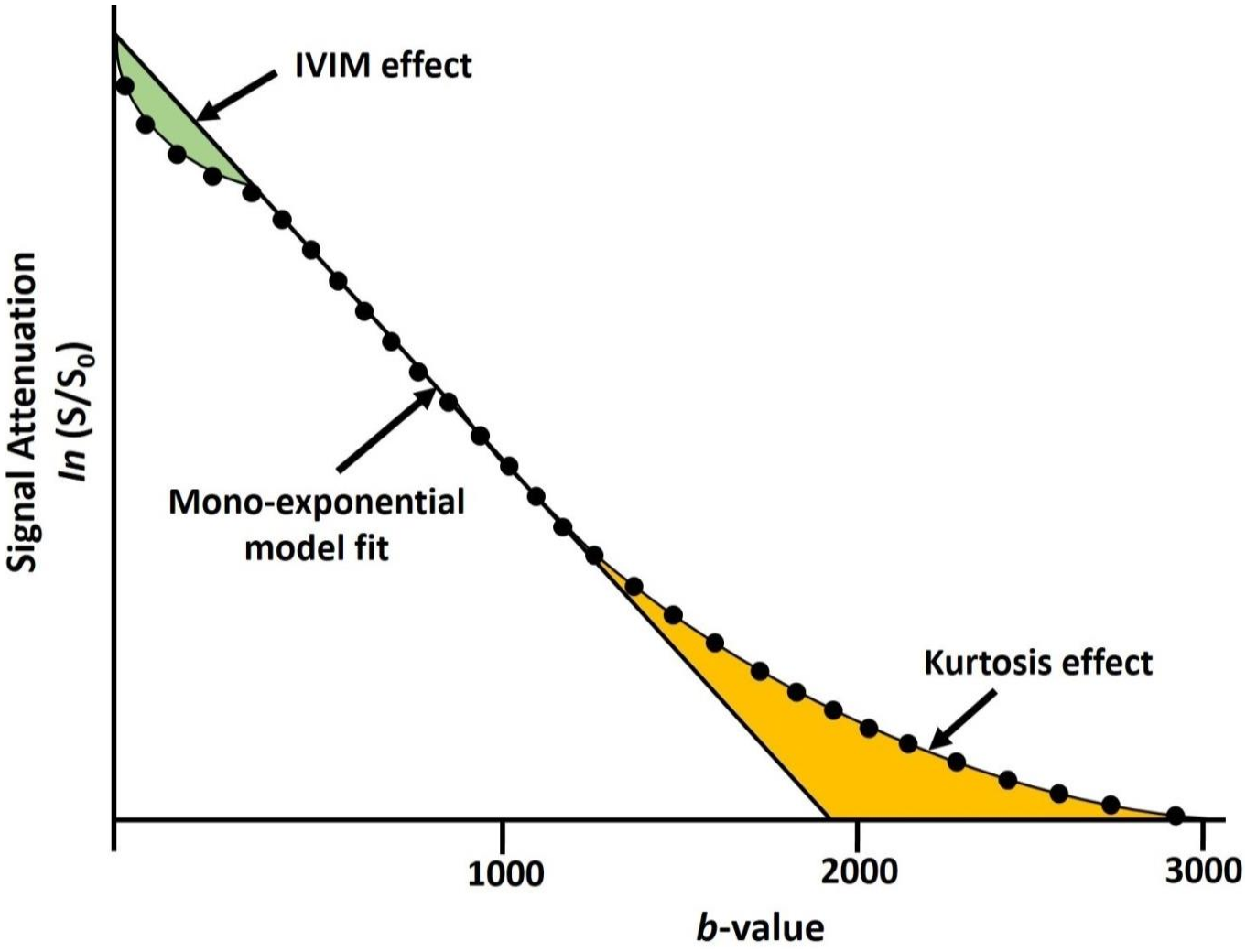

Figure 3.1. Deviation of the DWI signal from a mono-exponential model. At low b-values intravoxel incoherent motion (IVIM) perfusion in capillaries caused a deviation (green), at high b-values Kurtosis produces a deviation of the graph in the opposite direction, resulting in lower than expected apparent diffusion coefficient values (yellow).

Theoretically, kurtosis values may quantify the variability in tissue structure within the region of interest, providing a measurement of tissue heterogeneity, which may be useful for assessing structural abnormalities in pathologic regions. DKI measures two parameters, the apparent diffusivity D_{app} quantifies the exponential component of signal decay and is similar to the Apparent Diffusion Coefficient (ADC) in the standard monoexponential model. The apparent kurtosis K_{app} measures the first-order deviation from monoexponential decay and is thus a simple measurement of the deviation from a Gaussian distribution of displacements. Previous retrospective studies have suggested a possible correlation between K_{app} and prostate cancer aggressiveness [8, 9], although a recent large retrospective study showed that despite good independent results for DKI, no added value was observed over standard DWI sequences [10].

3.1.3 Magnetization Transfer Imaging

Another potential functional sequence is magnetization transfer imaging (MTI), which images the interaction of free and bound water molecules. MTI quantifies the transfer of nuclear spin polarisation between the “bound” and “free” pool of water within tissues. The “free” pool consists of relatively mobile protons, and provides the majority of the visible MR signal. The “bound” pool incorporates both macromolecules and the “hydration layer” of water molecules bound to their charged surface by hydrogen bounds. The protons associated with macromolecules are relatively immobile, as such their T2 relaxation times are very short (≈10 - 15 μs) and their decay time too rapid for an MR signal to be detected [11]. However, the hydration layer of water is able to interact with the “free” pool on its outer surface, and is able to modulate the relaxation properties of free water via dipole-dipole interactions, thereby affecting its MR signal.

This effect is exploited in MTI, where an off-resonance radiofrequency pulse is applied to saturate the hydration layer of the bound pool, with this saturation then being transferred (magnetization transfer) to the water protons in the free pool. Depending on the exchange rate between the two pools, the free pool of protons will become partially saturated and, if subsequently imaged, its signal will be reduced. The change in signal intensity pre- and post-application of the MT pulse for a given voxel can be defined and computed as the magnetization transfer ratio (MTR), according to the equation:

$$\text{MTR (\%)} = \frac{\text{MToff} - \text{MTon}}{\text{MToff}}\ x\ 100$$

Where MT_{off} represents the baseline reference signal intensity and MT_{on} represents the intensity following the saturation pulse

MTR relates to the organization of macromolecular protons in the tissue and is thought to be an indicator of the structural integrity of tissues and the microstructural changes induced by pathological processes [12]. MTR has been shown to increase in malignancy, with changes thought to derive from a combination of abnormal cell membrane structures or changes in cell number or size [13, 14]. Preliminary work in prostate cancer demonstrated higher MTR within the whole PZ in patients with known prostate cancer, compared to normal appearing tissue in biopsy-negative patients [15]. These results supported earlier work in MTR, where a subset of 22 patients with localised prostate cancer demonstrated higher MTR in cancer compared to controls, with a reduction in values following hormone therapy [16].

Advanced functional imaging with DKI and MTI may provide insight into the tissue structure of prostate cancer and help us to better understand the complicated micro-environment of tumours. We therefore aimed to evaluate whether the addition of these two novel MR quantification parameters to standard MRI sequences could aid prostate cancer detection in a TPUS re-biopsy population.

3.2 Methods

3.2.1 Patient population

30 patients with a clinical suspicion of undiagnosed prostate cancer were prospectively enrolled into this institutional review board and ethics committee approved single-institution study (CUH/13/EE/0100) [17]. Participants were recruited between November 2013 and June 2016, with written informed consent obtained in all cases. Inclusion criteria included negative biopsy with continued suspicion of prostate cancer (for example, high and/or rising PSA levels) and a suspicious lesion on MRI (n = 24), or a previous diagnosis of low-grade cancer with MRI suspicious for a new lesion in a remote location of the gland (n = 6). Patients subsequently underwent an MR-TRUS fusion template transperineal biopsy, including target cores from any MRI suspicious lesion/s.

3.2.2 MR Imaging

All patients underwent 3T MRI (MR 750, GE Healthcare, Waukesha, WI, USA) using a 32-channel phased-array body coil. The protocol included three-plane localizer images followed by multiplanar T2-weighted fast recovery fast spin-echo (FSE) images of the prostate and axial T1-weighted FSE images of the pelvis. The high resolution T2-weighted axial parameters were: TE 99-106ms; TR 3000-5000ms; field-of-view (FOV) 22x22 cm; acquisition matrix 384x288 (giving in plane resolution 0.6 x 0.8 mm); 3 signal averages; no-phase-wrap; slice thickness 3.0 mm/gap 1.0 mm; echo-train length (ETL) 16; receiver bandwidth ±50Hz.

Standard clinical axial DWI was performed using both single spin-echo and dual spin-echo echo-planar imaging (EPI) pulse sequences: TE 67-72ms (single SE) or 90ms (dual SE); TR

4000ms; FOV 28×28 cm; acquisition matrix 144x144 (giving resolution 1.9 x 1.9mm^2); slice thickness 4mm (no gap); receiver bandwidth ±111 kHz; parallel imaging (ASSET) factor 2; 8 signal averages; b values of 100 and 1000 s/mm^2, with ADC maps automatically generated by the scanner software, using monoexponential fitting. Additional data was acquired with b-value of 1400 s/mm^2 with the same acquisition parameters except: acquisition matrix 128x128 (resolution 2.2x2.2 mm^2) and a slightly increased TE of 70-75ms.

DKI was performed as a single-shot dual-spin-echo EPI pulse sequence: TE/TR = 94/6000 ms; 6 signal averages; parallel imaging (ASSET) factor 2; FOV 28 x 28 cm^2; acquisition matrix 128x96 (giving resolution 2.2x2.9 mm^2); slice thickness 3.6 mm/gap 0.4 mm; b-values of 150, 450, 800, 1150, 1500 s/mm^2; receiver bandwidth ±111 kHz. The DKI model used second-order approximation to the exponential dependence of DWI signal *S* with b-value (*b*):

$$S = S_0 * \exp(-bD_{app} + 1/6 * b^2 D_{app}^2 K_{app})$$

Where S_0 is the signal when b = 0 s/mm^2

Magnetization transfer imaging volumes covering the prostate were acquired with two 3D spoiled gradient recalled-echo acquisitions (SPGR) which were acquired with- and without an MT saturation pulse with the following scan parameters: TR=24ms, TE= 2.4ms, flip angle= 5°, acquisition matrix= 256 x 160 and FOV=22cm, slices=22 with slice thickness matched to the T2 axial series. The saturation pulse consisted of a 400° Fermi shape pulse, of 10ms duration and 800 Hz bandwidth at 2.5 kHz off-resonance frequency. DKI (D_{app} and K_{app}) and magnetization transfer ratio (MTR) parameter maps were calculated offline using custom software written in Matlab (Mathworks, MA, USA).

DCE images were acquired as an axial 3D fast-spoiled gradient echo (GRE) sequence: TR/TE 5.4/2.4ms; flip angle 17°; FOV 22x22 cm^2; acquisition matrix 192x160x22-26; slice thickness 4mm; 0.75 Nex; receiver bandwidth ± 31 kHz; 85–100 dynamic phases with temporal resolution 7s. Gadobutrol (Gadovist, Schering AG) was injected i.v. as a bolus, via a power injector (rate 3 mL/s, dose 0.1 mmol/kg) followed by a 25 mL saline flush, with a total scan duration of approximately 10 minutes.

3.2.3 Image analysis

The MRIs were prospectively read by 1 of 2 uro-radiologists with more than 4 years' experience of clinical prostate MRI reporting at a high-volume tertiary referral centre. Images were analysed according to the Prostate Imaging-Reporting and Data System (PI-RADS) version 1 criteria [18] prior to February 2015 and subsequently using criteria as described in PI-RADS version 2 [4]. In all cases, interpretation of the images was based on the following Likert scoring scale for tumour probability: 1 = very low (clinically significant cancer is highly unlikely to be present), 2 = low (clinically significant cancer is unlikely to be present), 3 = intermediate (the presence of clinically significant cancer is equivocal), 4 = high (clinically significant cancer is likely to be present), 5 = very high (clinically significant cancer is highly likely to be present). Although similar to the scoring system subsequently adopted in PI-RADS version 2, a size criterion was not used to determine lesion probability. Thus whilst category 1, 2, 3 and 5 are equivalent, PI-RADS category 4 lesions will differ and, depending on size or lesion conspicuity, may be categorised as scores 3, 4 or 5 using the Likert system. The DKI and MTR values did not inform biopsy decision making. For the purposes of the study, a positive MRI lesion was defined as a score of ≥3; targets were prospectively drawn on the Biopsee™ platform, using T2W as primary, and ADC as

secondary source images.

3.2.4 Biopsy procedure

The Biopsee™ MRI/TRUS-fusion biopsy system biopsy system v.1 or v.2 (Medcom, Darmstadt, Germany) was used for all biopsies. It includes computer hardware and software for image fusion and an ultrasound machine. A transrectal BK Medical (Peabody, Massachusetts, USA) FlexFocus™ ultrasound probe was sited, the biplanar probe is fixed on a stepping unit and sagittal images of the prostate were aligned with MR images using fusion software. All patients underwent systematic transperineal biopsies according to the Ginsburg protocol, using a spring-loaded biopsy gun and 18G needle via a brachytherapy template grid [19]; **Figure 3.2**. In all cases, 2 biopsy cores were taken from each lesion(s) first, with 24 background systematic biopsies subsequently acquired. All procedures were performed by 1 of 3 urologists with several years' experience of transperineal biopsy.

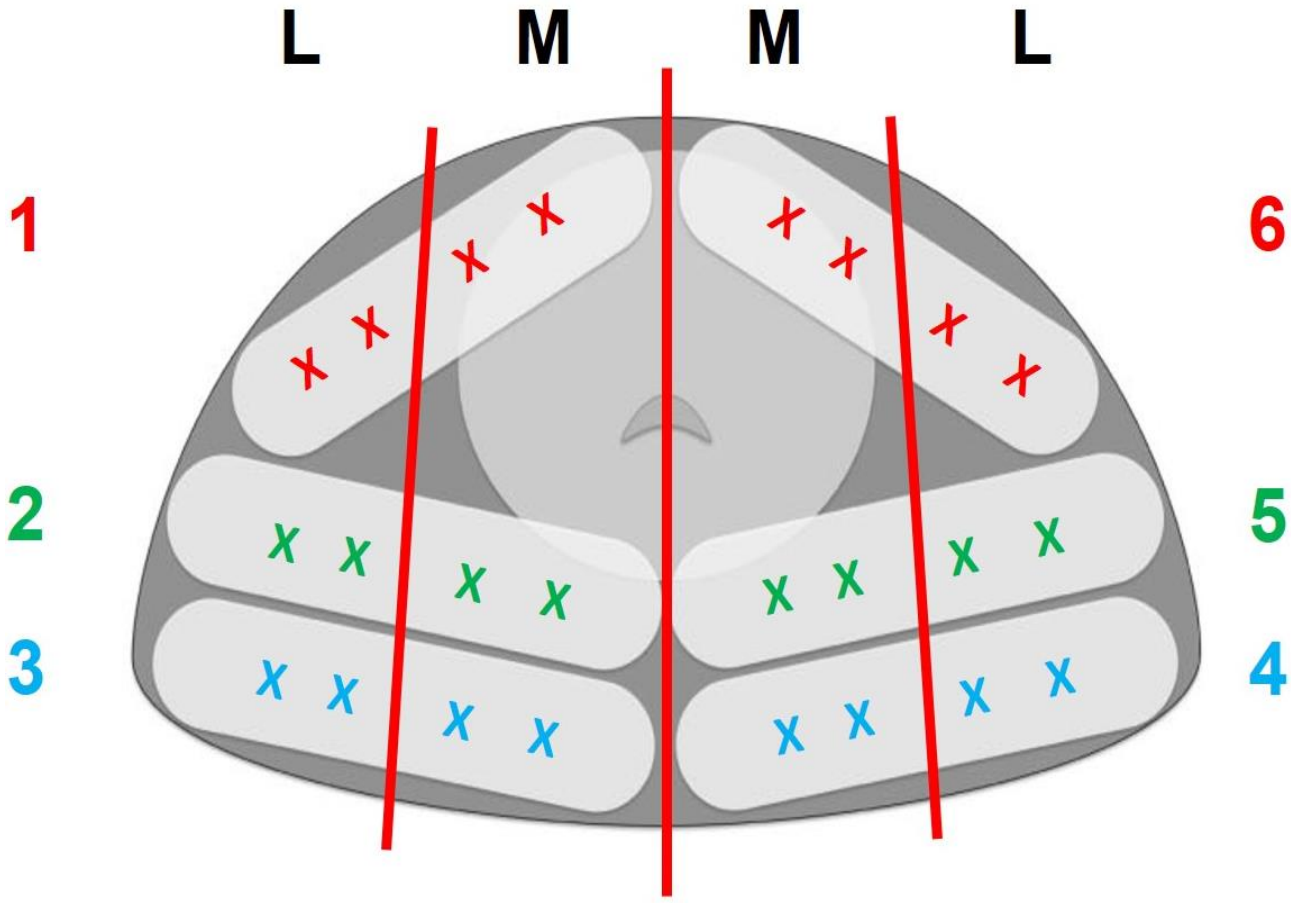

Figure 3.2. Ginsburg Transperineal biopsy protocol. Background areas of the prostate gland are systematically sampled according to the above template, using a transperineal brachytherapy grid.

3.2.5 Histopathology

All biopsies were graded with a Gleason score following the ISUP 2005 recommendations [20] by a specialist uropathologist. The final histology result from this assessment was used as data for the study.

3.2.6 Retrospective analysis

Prospectively defined target outlines are stored on the local clinical picture archiving and communication system (PACS, GE Healthcare) as part of the standard clinical workflow. A fellowship-trained radiologist with 7 years of clinical prostate MR reporting experience reviewed the original outlines and re-drew freehand regions-of-interest (ROIs)

corresponding to the target outline on T2-weighted axial images and avoiding inclusion of the urethra or extra-prostatic tissue where relevant, using in-house software programmed with Matlab (MathWorks, Natick, MA). Additional ROIs were drawn in regions of benign PZ and TZ. Benign ROIs were defined as "normal appearing" on standard mpMRI sequences, on the side contralateral to the target, and with corresponding negative cores on biopsy, drawn where possible over 3 consecutive MR slices, with a minimum volume of 0.5 cm^3. All ROIs were stored and secondarily transposed onto the ADC, DKI, and MTR maps; in cases of significant distortion, the ROIs were adjusted to allow for this, using the T2-weighted images for reference. DKI (D_{app} and K_{app}) and magnetization transfer ratio (MTR) parameter maps were calculated offline using custom software written in Matlab. For DKI, the noise-only images were used to reduce and partially compensate for noise-floor bias which could otherwise artificially enhance the kurtosis measurement [10]. A small proportion of DKI fit-failure pixels were excluded. The mean ROI values of ADC, D_{app} and K_{app}, and MTR maps were used for analysis.

3.2.7 Statistical analysis

Medians and ranges were used to summarize continuous variables. Wilcoxon signed-rank test was performed to assess the relationships between parameters and benign tissue versus tumour tissue and between tumour grades, for both the PZ and TZ. Receiver operating characteristic (ROC) analyses were used to assess the diagnostic utility of the metrics, alone and in combination, for the detecting tumour and for discriminating different Gleason grades of tumour. An optimal threshold was determined for each metric for discriminating tumour from benign tissue. Pearson's correlation was performed to assess the relationship between the different metrics assessed, where -1.0 to -0.75 is considered a

strong negative association, -0.75 to -0.5 moderate negative, -0.5 to -0.25 weak negative, -0.25 to +0.25 no linear association, +0.25 to +0.5 a weak positive association, +0.5 to +0.75 moderate positive, and +0.75 to +1.0 a strong positive association. All statistical analysis was performed in R (version 3.1.1, The R Foundation for Statistical Computing, Vienna, Austria); $p < 0.05$ was considered statistically significant.

3.3 Results

Thirty patients were included in the study group, with a median age of 65.5 years (mean 64.7, range 50 - 76 years) and a median pre-biopsy PSA level of 7.67 ng/mL (mean 8.9, interquartile range 6.12 - 11.98 ng/mL). The median time from MRI to biopsy was 26 days (mean 37.5, IQR: 7.25 - 48.25 days). 26 patients had a least 1 previous biopsy, with interval from most recent biopsy to MRI at least 3 months (median 13 months, range 3 - 114 months, interquartile range 4 - 26 months).

Prostate cancer was detected in 24/30 patients including targeted and background cores and in 20 patients within at least 1 target core. In the 4 patients with only background cores positive all had Gleason score (GS) 3+3 in 1-5% of 1 core only. The remaining 20 patients had 26 separate MRI lesions with positive target cores (4 patients with 2 targets, 1 with 3), of which 13 were in the peripheral zone (PZ) and 13 in the transition zone (TZ). The final pathology of the 26 targets was GS 3+3 (n=8), 3+4 (n=12), 3+5 (n=1), 4+3 (n=2), and ≥4+4 (n=3); **Table 3.1**.

Gleason Grade	Overall	Peripheral Zone	Transition Zone
Benign	10	3	7
3+3	8	4	4
3+4	12	8	4
3+5	1	0	1
4+3	2	0	2
4+4	1	1	0
4+5	2	0	2

Table 3.1. Target biopsy outcomes for MRI defined lesions

Mean tumour ADC (PZ: 0.902, TZ: 0.845 x $10^{-3}mm^2s^{-1}$) and D_{app} (PZ: 1.167, TZ: 0.951 x $10^{-3}mm^2s^{-1}$) values were significantly lower than normal PZ (ADC 1.579, D_{app} 2.221 x $10^{-3}mm^2s^{-1}$) and benign TZ (ADC 1.270, D_{app} 1.808 x $10^{-3}mm^2s^{-1}$); **Figure 3.3**. Conversely, mean K_{app} and MTR values were significantly higher for PZ tumour (716, 25.0%, respectively) and TZ tumour (871, 30.0%, respectively) compared to normal PZ (507, 20.0%, respectively) and TZ (615, 26.9%, respectively). Normal TZ had lower ADC and D_{app} and higher K_{app} and MTR than normal PZ tissue, with cystic BPH demonstrating higher ADC and D_{app} and lower K_{app} and MTR compared to normal TZ. For all parameters there was a significant difference between both normal and tumour tissue and cystic BPH and normal TZ ($p = 0.005 - <0.001$); **Table 3.2**.

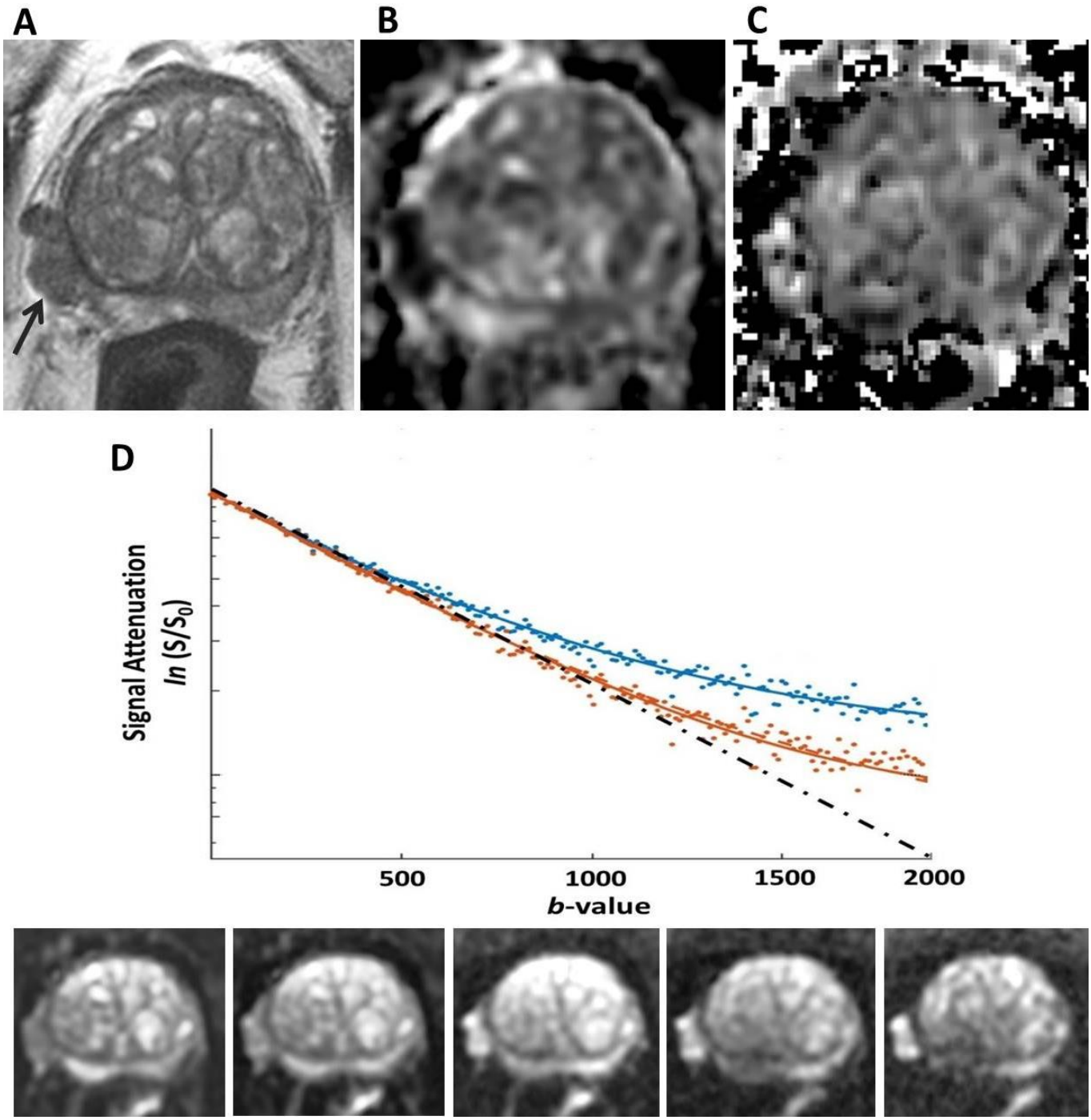

Figure 3.3. Raw b-value image data and fitting of the DKI model.
65 year old man, PSA 17.15 ng/ml. A: T2WI shows a lesion in the right base PZ (arrow), target biopsy Gleason 4+4 tumour in 50% of both cores. B: ADC map shows restricted diffusion (0.894 x 10-3 mm^2s^{-1}). C: K_{app} map shows average tumour value of 697.6. D: Signal intensity decay plotted against b-value for normal (red) and tumour (blue) using a diffusion kurtosis compared to a mono-exponential (dashed line) model, showing improved fitting of the data at the higher b-values. Bottom row: source b-values images acquired (left to right) at 150, 450, 800, 1150, and 1500 s/mm^2.

Parameter	Normal Tissue	Tumour Target	Cystic BPH	p-value (normal vs tumour)	p-value (normal vs cystic BPH)
ADC (x 10^{-3} mm^2s^{-1})					
Peripheral Zone	**1.579 [1.363 – 1.794]**	**0.902 [0.869 – 0.974]**	**N/A**	**<0.001**	**N/A**
Transition Zone	**1.270 [1.244 – 1.355]**	**0.845 [0.813 – 0.885]**	**1.955 [1.669 – 2.031]**	**<0.001**	**<0.001**
D_{app} (x 10^{-3} mm^2s^{-1})					
Peripheral Zone	**2.221 [2.039 – 2.446]**	**1.167 [0.910 – 1.366]**	**N/A**	**<0.001**	**N/A**
Transition Zone	**1.808 [1.712 – 1.895]**	**0.951 [0.853 – 1.062]**	**2.152 [2.113 – 2.258]**	**<0.001**	**<0.001**
K_{app} (unitless)					
Peripheral Zone	**507 [426-550]**	**716 [621-869]**	**N/A**	**0.004**	**N/A**
Transition Zone	**615 [548 - 653]**	**871 [663 - 1034]**	**374 [303 - 501]**	**0.004**	**0.001**
MTR (%)					
Peripheral Zone	**20.0 [15.5 – 22.9]**	**25.0 [24.0 – 28.1]**	**N/A**	**<0.001**	**N/A**
Transition Zone	**26.9 [23.5 - 28.0]**	**30.0 [28.2 - 32.0]**	**15.2 [6.9 - 21.3]**	**0.005**	**<0.001**

Table 3.2. Target biopsy outcomes for MRI defined lesions and contralateral normal (benign) tissue. Mean values listed, Interquartile range in parentheses

ADC was able to distinguish any Gleason-grade tumour from benign tissue with sensitivity and specificity of 92.3% and 100% in the PZ and 100% and 100%, respectively in the TZ. K_{app} differentiated tumour in the PZ with 76.9% sensitivity and 83.3% specificity and 69.2% and 100%, respectively in the TZ. MTR distinguished tumour from benign tissue with sensitivity and specificity of 76.9% and 86.7% in the PZ and 76.9% and 76.7%, respectively in the TZ; **Figures 3.4 – 3.5**. **Tables 3.3** demonstrates the diagnostic utility of the metrics, with receiver operating characteristic (ROC) area under the curve (AUC) values ranging from 0.767 to 1.000 for separating tumour from benign tissue (**Figure 3.6**).

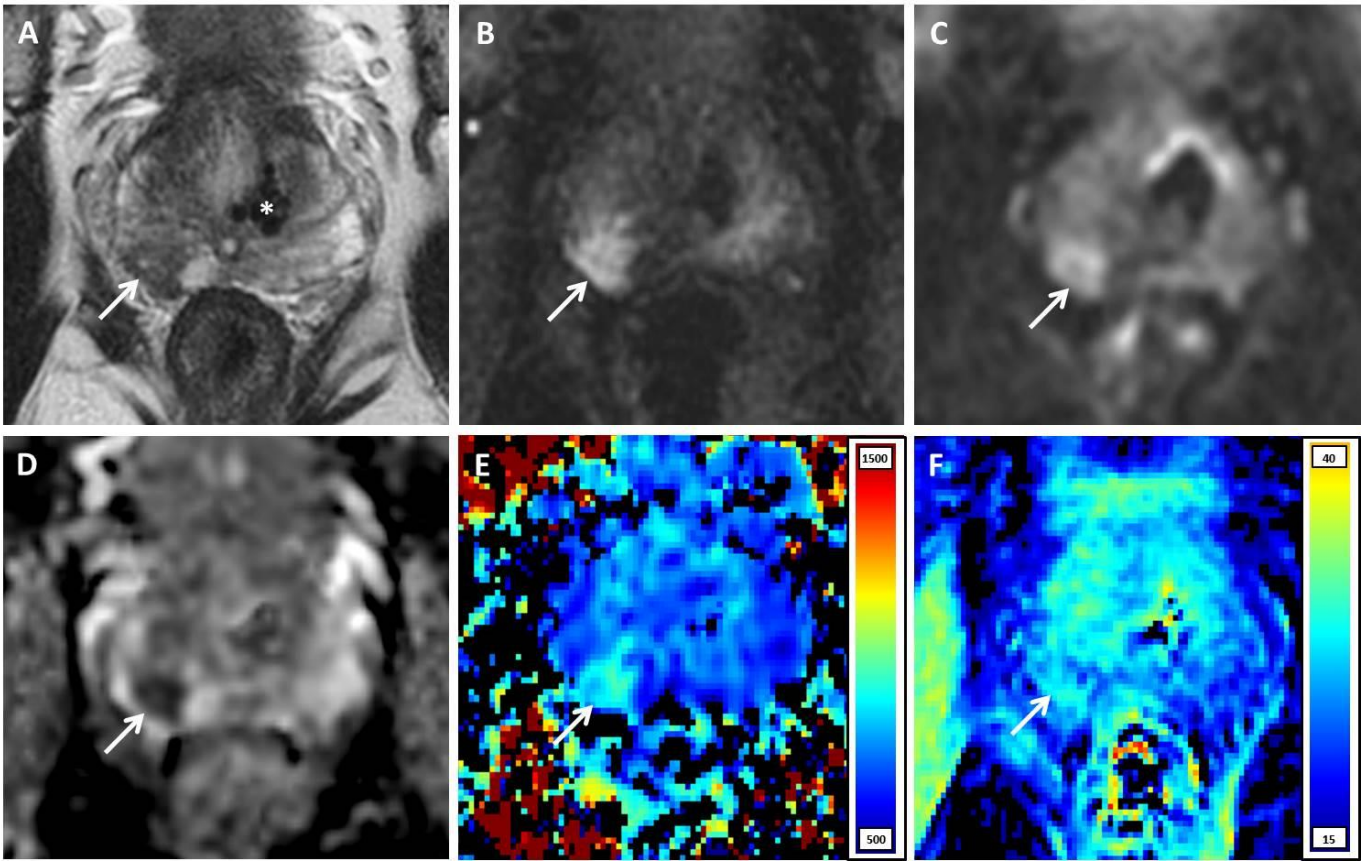

Figure 3.4. Peripheral zone target lesion. 64 year old with PSA of 6.5 ng/ml. Top row, clinical mpMRI sequences: T2w image (A), early time point DCE image (B) and b=1400 s/mm^2 diffusion-weighted image (C). Bottom row, assessed sequences: ADC map, value 0.902 x 10^{-3} mm^{2}s^{-1} (D), K_{app}, value 867.2 (E) and MTR, value 27.5% (F). The target in the right base PZ posteriorly (arrows) was prospectively defined. Note calcification in the left base TZ (* in A) with corresponding artefact on all other sequences. Target biopsy: 3+4=7 (35% pattern 4) in 60% cores.

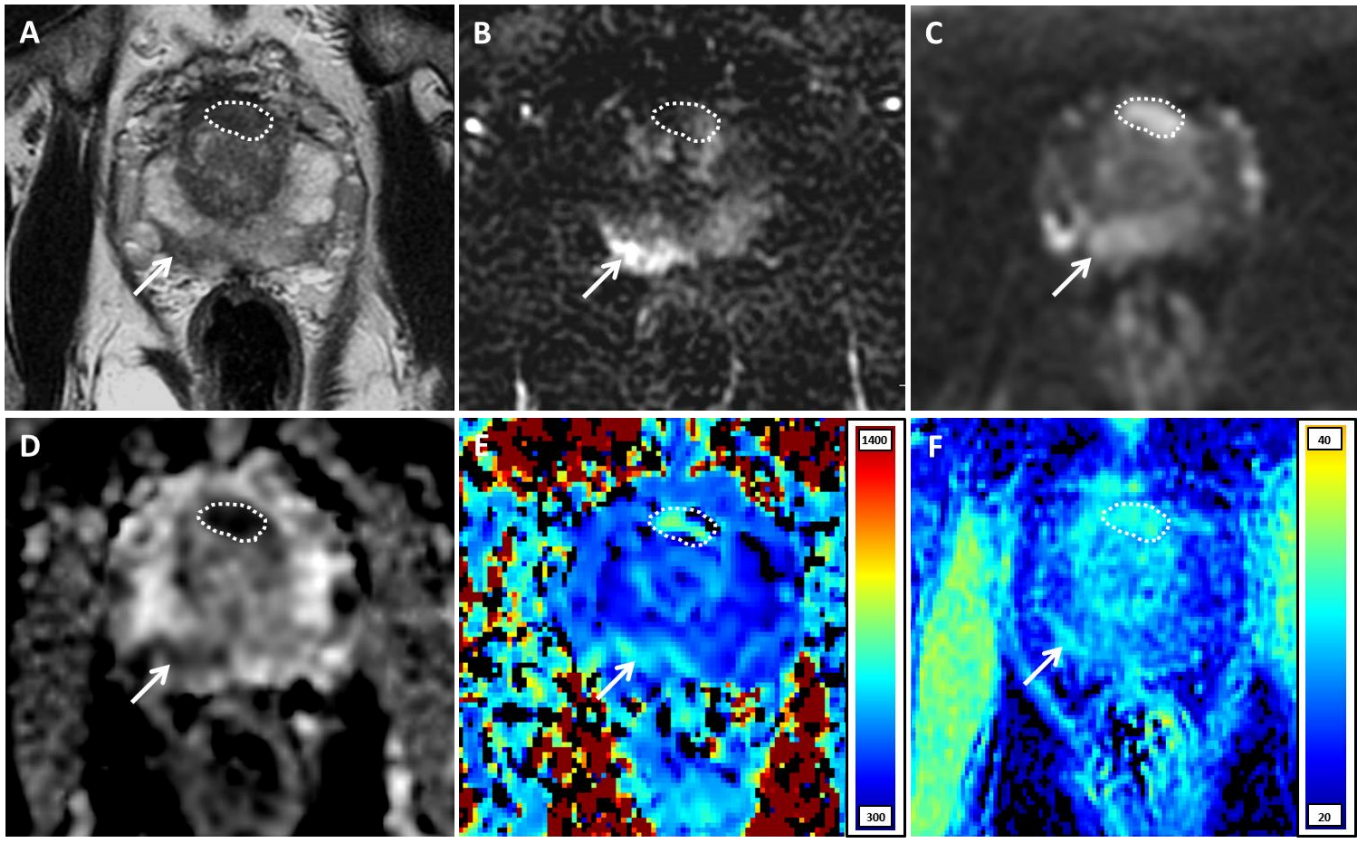

Figure 3.5. Peripheral and transition zone target lesions. 69 year old with PSA of 12.31 ng/ml. Top row, clinical mpMRI sequences: T2w image (A), early time point DCE image (B) and b=1400 s/mm^2 diffusion-weighted image (C). Bottom row, assessed sequences: (D): ADC map (values: PZ lesion 1.037 x 10^{-3} mm^{2}s^{-1}, TZ lesion 0.885 x 10^{-3} mm^{2}s^{-1}), (E): K_{app} (values PZ lesion 715.6, TZ lesion 518.5) and (F): MTR (values PZ lesion 24.4%, TZ lesion 31.7%). Targets prospectively drawn in the anterior mid gland TZ (outlines) and right mid PZ posteriorly (arrows). Both lesions positive on K_{app} and MTR maps, note clear zonal differentiation seen on MTR maps. Target biopsy, PZ lesion: Gleason 3+4 in 2/2 cores 50%, up to 8 mm; TZ lesion: Gleason 3+3 in 2/2 cores 50%, up to 4 mm.

	Cut-Off	AUC	Sensitivity (%)	Specificity (%)
ADC x 10^{-3} mm^{2}s^{-1}				
Transition Zone	1.076	1.000	100.0	100.0
Peripheral Zone	1.037	0.979	92.3	100.0
D_{app} x 10^{-3} mm^{2}s^{-1}				
Transition Zone	1.524	1.000	100.0	100.0
Peripheral Zone	1.481	0.990	100.0	96.7
K_{app} (Unitless)				
Transition Zone	819.9	0.772	69.2	100.0
Peripheral Zone	621.2	0.772	76.9	83.3
MTR (%)				
Transition Zone	28.2	0.767	76.9	76.7
Peripheral Zone	24.0	0.828	76.9	86.7

Table 3.3. Diagnostic utility of each respective metric in separating normal tissue versus tumours

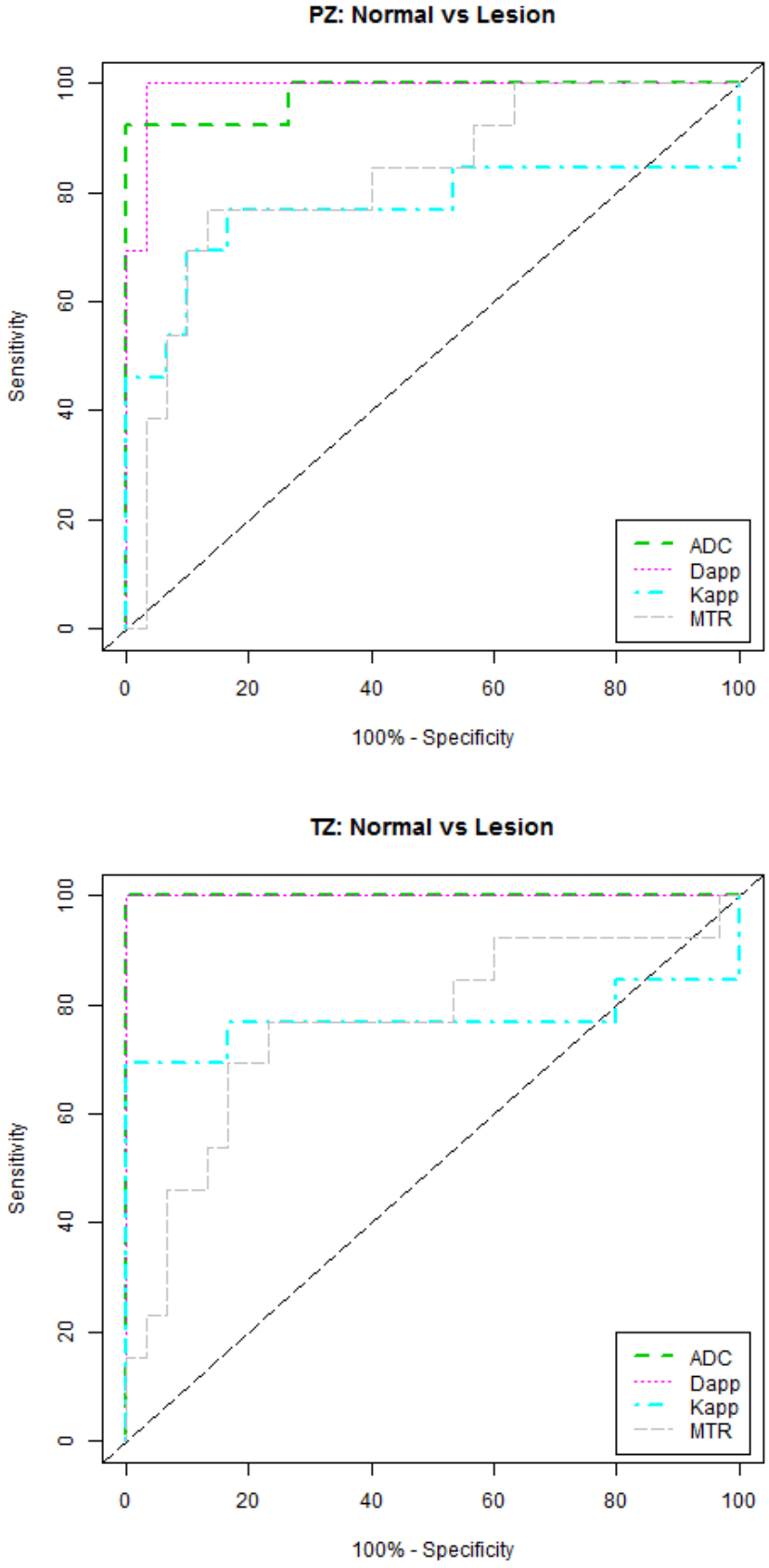

Figure 3.6. Receiver operating characteristic curves of the performance of ADC, D_{app}, K_{app}, and MTR for differentiating benign tissue and tumour in the peripheral zone (top) and transition zone (bottom).

The ability of the parameters to distinguish lower grade (Gleason 3+3) from higher grade (Gleason ≥3+4) was assessed. The different values derived for normal and tumour tissue for all metrics in the PZ and TZ necessitated a separate analysis by tissue type. The Gleason 3+3 group included 4 PZ and 4 TZ tumours, the GS ≥3+4 included 9 PZ and 9 TZ tumours. All measured parameters were poor at separating lower and higher grade disease for both PZ (p = 0.414 - 0.825) and TZ (p = 0.148 - 0.825); **Figures 3.7 and 3.8 and Table 3.4**.

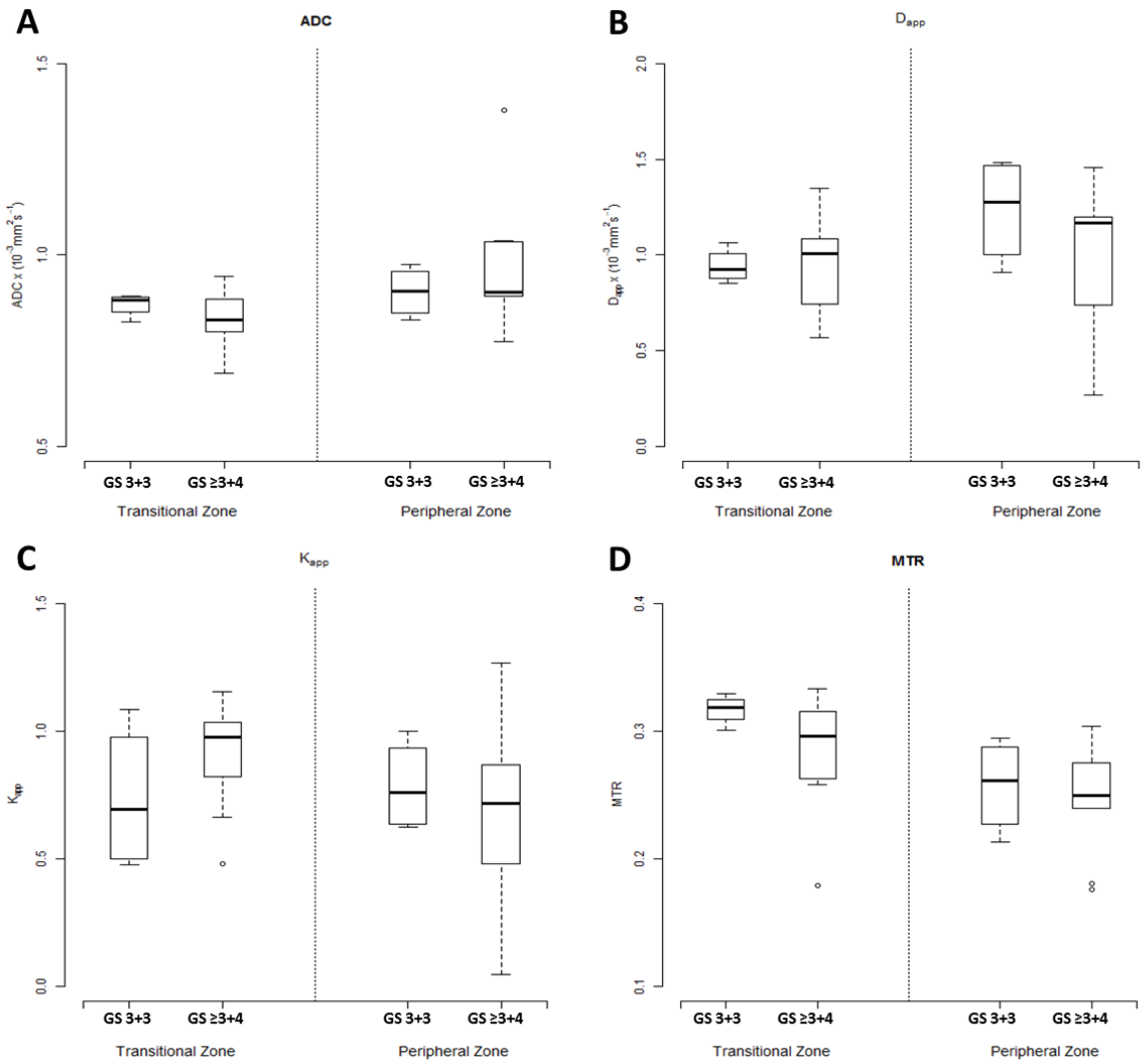

Figure 3.7. Box and whisker plots for distinguishing Gleason (GS) 3+3 from GS ≥3+4 tumours for ADC (a), D_{app} (B), K_{app} (C) and MTR (D). Top and bottom of boxes represent 25th and 75th percentiles of data, line in boxes represents the median value and bars representing data within 1.5 times interquartile range. Circles denote outliers.

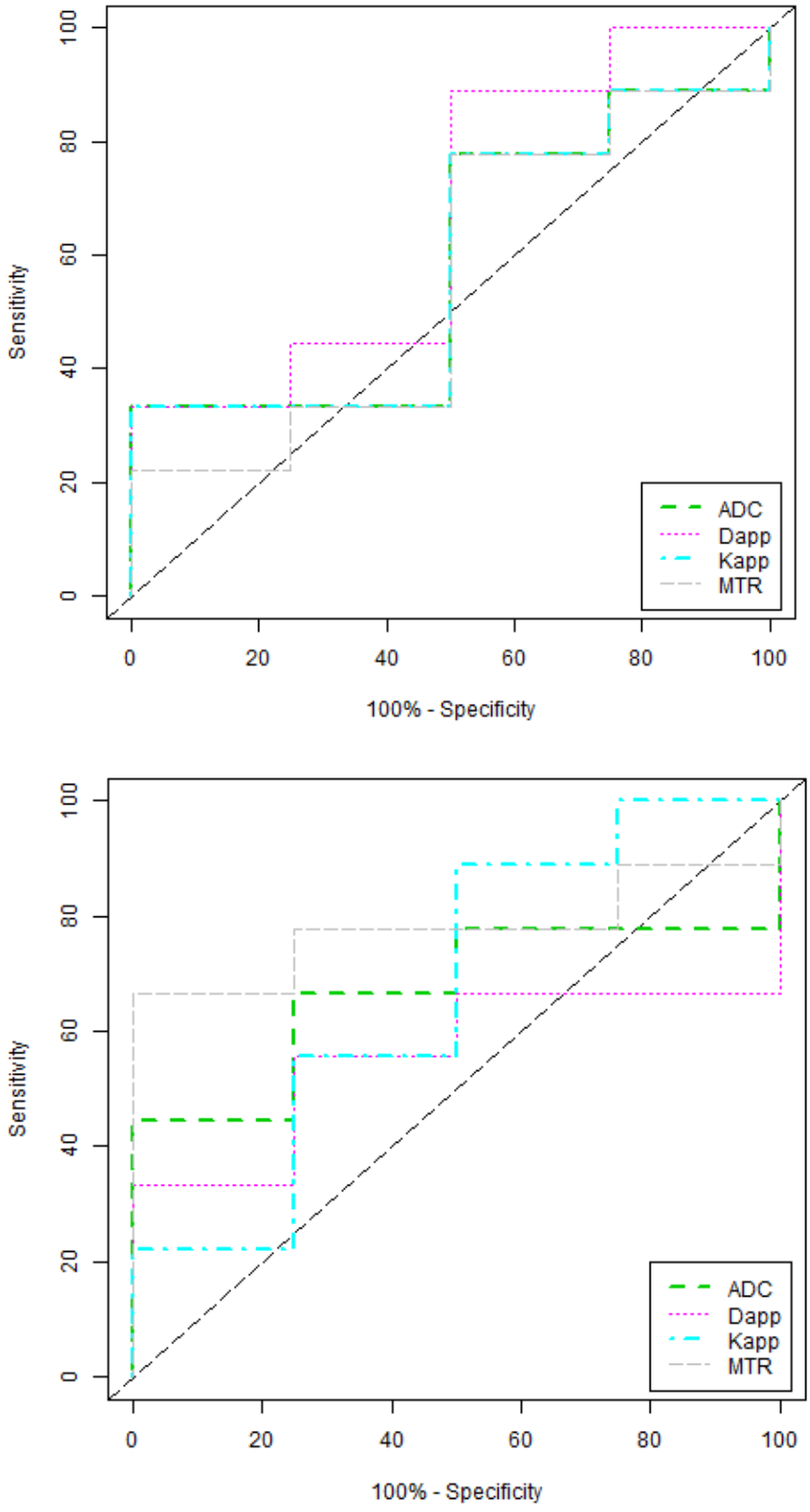

Figure 3.8. Receiver operating characteristic curves of the performance of ADC, D_{app}, K_{app}, and MTR for differentiating lower grade (Gleason 3+3) from higher grade (Gleason ≥3+4) tumour in the peripheral zone (top) and transition zone (bottom).

	Gleason 3+3	Gleason ≥3+4	p-value
Peripheral Zone	*n = 4*	*n = 9*	
ADC x 10^{-3} mm^2s^{-1}	905 [860 - 949]	902 [893 - 1036]	0.711
D_{app} x 10^{-3} mm^2s^{-1}	1275 [1047 - 1463]	1167 [740 - 1196]	0.414
K_{app} (Unitless)	759 [643 - 902]	716 [480 - 867]	0.711
MTR (%)	26.1 [23.4 - 28.4]	25.0 [24.0 - 27.5]	0.825
Transition Zone	*n = 4*	*n = 9*	
ADC x 10^{-3} mm^2s^{-1}	881 [864 - 887]	830 [799 - 884]	0.414
D_{app} x 10^{-3} mm^2s^{-1}	926 [889 - 979]	1006 [745 - 1083]	0.825
K_{app} (Unitless)	695 [508 - 924]	975 [820 - 1035]	0.414
MTR (%)	31.9 [31.3 - 32.2]	29.6 [26.3 - 31.5]	0.148

Table 3.4. Ability of metrics to distinguish lower grade (Gleason 3+3) from higher grade (Gleason ≥3+4) tumours. Mean values listed, interquartile range in parentheses

ADC showed a strong overall correlation to D_{app} (r = -0.862), as expected. ADC showed moderate inverse correlation to MTR (r = -0.618) and an inverse correlation to K_{app} (r= -0.767) in normal tissue, with a weak positive correlation in tumour tissue (r= -0.459 and -0.444, respectively); details are given in **Table 3.5**. MTR showed a moderate correlation to both K_{app} (r=0.570) and D_{app} (r=-0.537) in normal tissue, but conversely showed no correlation to K_{app} (r=0.141) and D_{app} (r=-0.024) in tumour tissue (**Figure 3.9 and 3.10**).

Comparators	Tumour Tissue (TZ + PZ)	Normal Tissue (TZ + PZ)	Normal + Tumour Tissue (TZ + PZ)
ADC vs K_{app}	-0.444	-0.767	-0.641
ADC vs D_{app}	-0.041	-0.790	0.862
ADC vs MTR	-0.459	-0.618	-0.633
K_{app} vs D_{app}	0.646	-0.532	-0.359
K_{app} vs MTR	0.141	0.570	0.429
D_{app} vs MTR	-0.024	-0.537	-0.531

Table 3.5. Correlation between assessed metrics (Pearson's Rho)

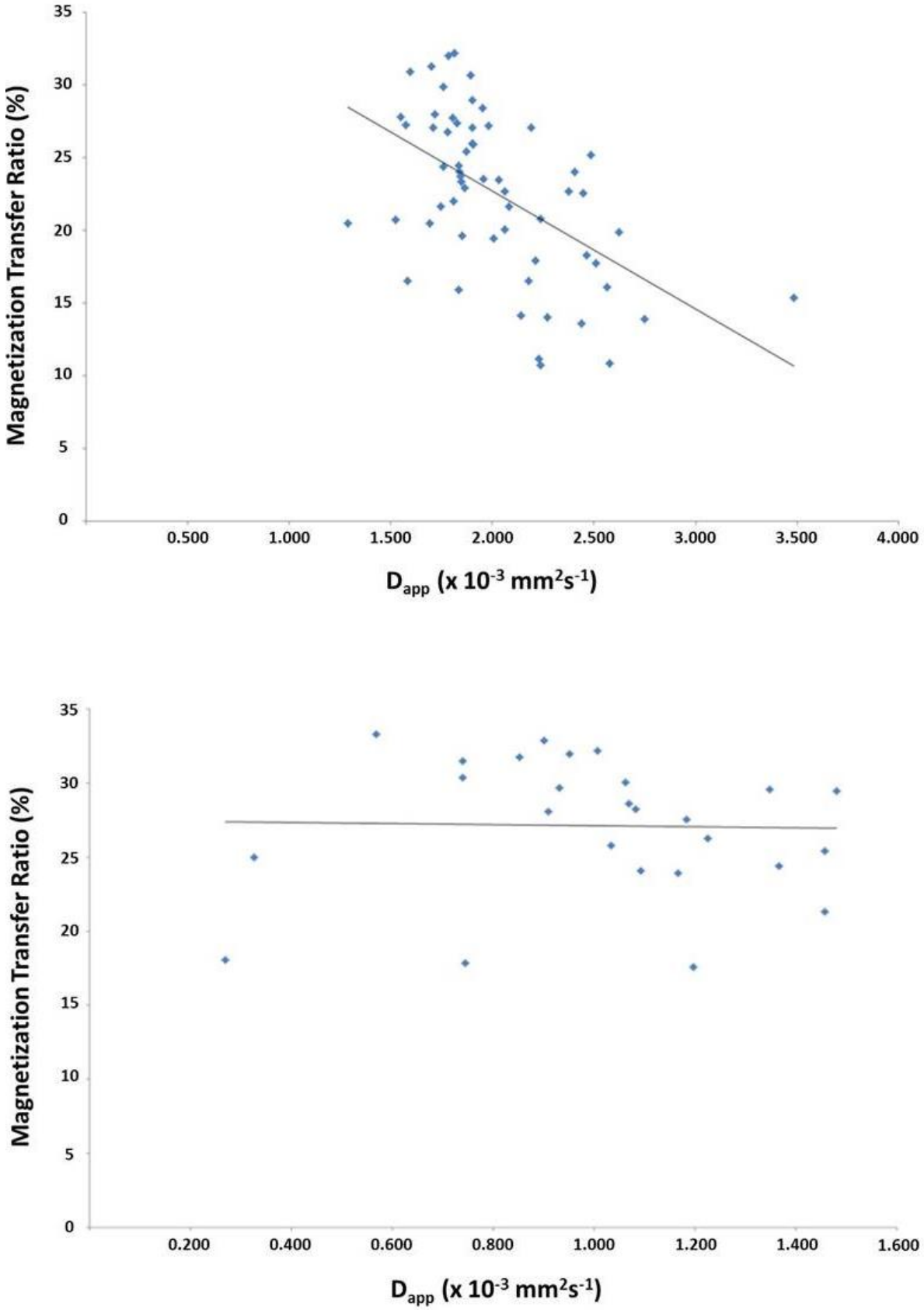

Figure 3.9. Correlation plots between assessed MTR and D_{app}. Top: MTR compared to D_{app} in normal PZ and TZ (Rho = -0.537). Bottom: MTR compared to D_{app} in PZ and TZ tumours (Rho = -0.024).

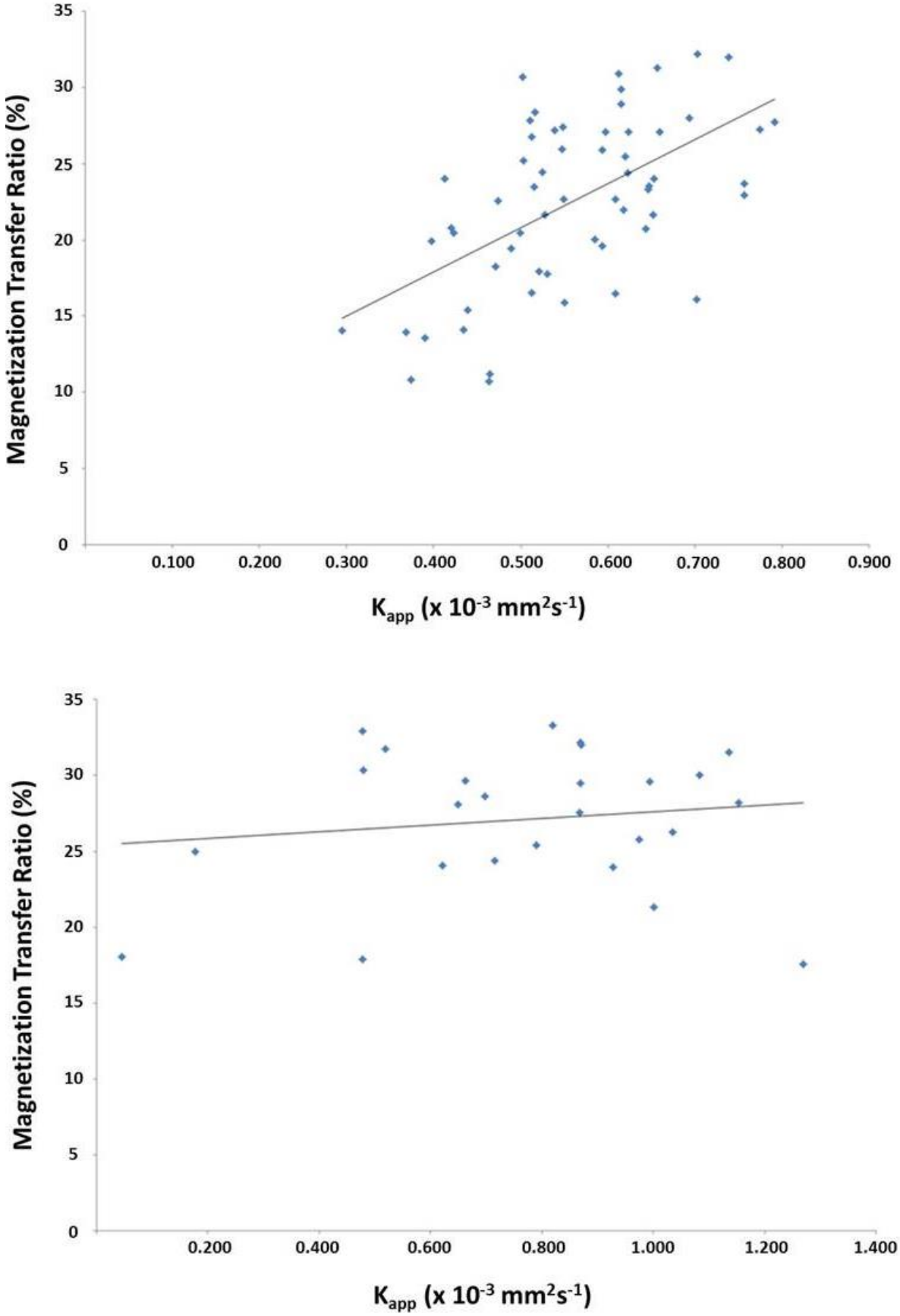

Figure 3.10. Correlation plots between assessed MTR and K_{app}. Top: MTR compared to K_{app} in normal PZ and TZ (Rho = 0.570). Bottom: MTR compared to K_{app} in PZ and TZ tumours (Rho = 0.141).

Additional incidental findings that could be appreciated on the MTR maps and source MT images were haemorrhage, calcification, and utricle cysts (**Figure 3.11**).

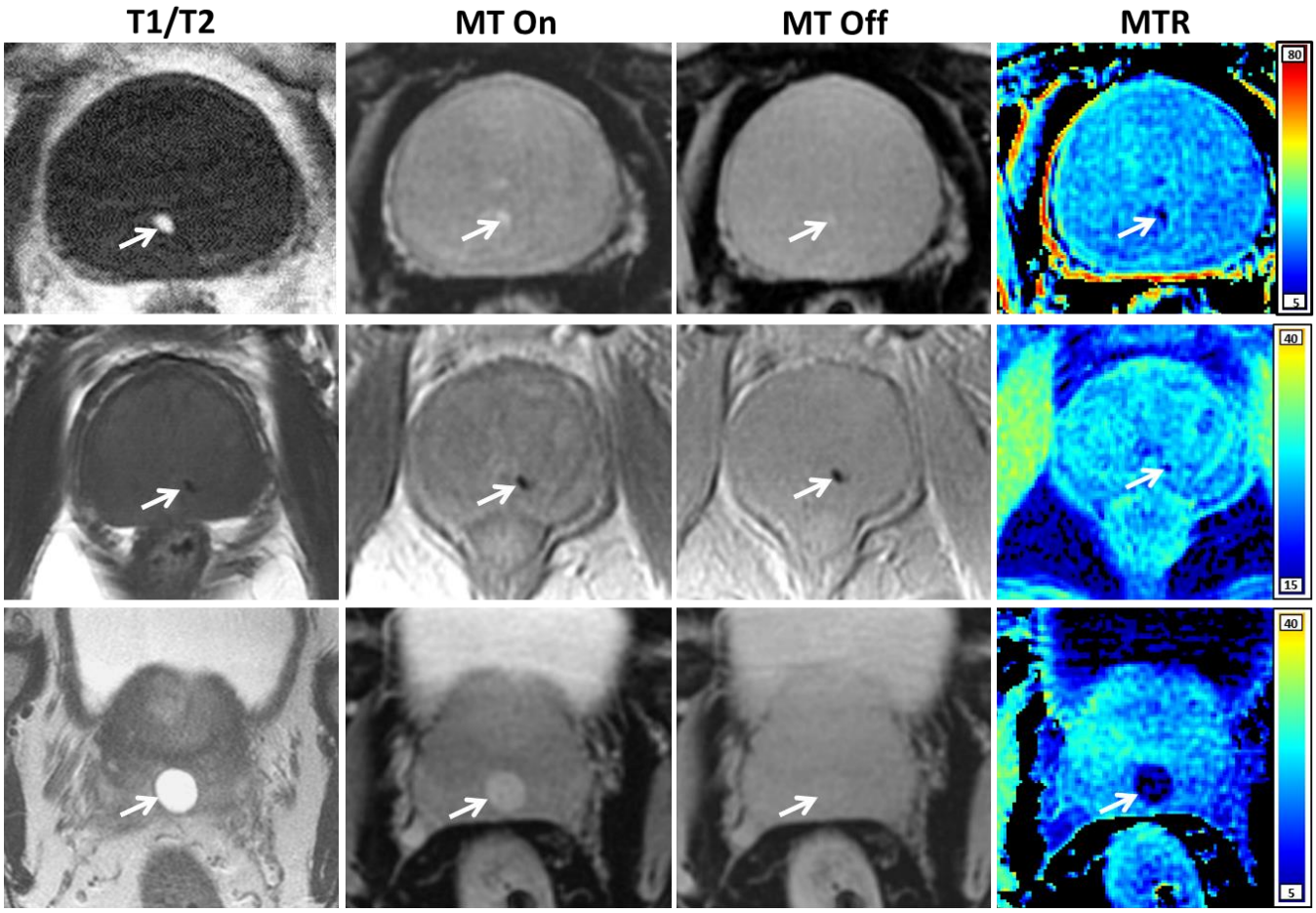

Figure 3.11. Features demonstrated by Magnetization Transfer Imaging. Top row: haemorrhage shown as high signal on T1 weighted imaging (arrows) appears as high signal on MT on and off imaging and low signal on MTR. Middle row: calcification appears as low signal on T1, MT on, MT off and MTR maps (arrows). Bottom row: Utricle cyst in the midline at the base shown as high signal fluid structure on T2 weighted imaging (arrows) appears as high signal on MT on, isointense on MT off and low on MTR.

3.4 Discussion

In this study we compared magnetization transfer imaging and non-Gaussian diffusion kurtosis imaging to conventional mpMRI sequences for the detection of prostate cancer in a re-biopsy population, using targeted transperineal biopsy as the reference standard. All 4 measured parameters were able to distinguish benign from tumour tissue, but performed poorly at differentiating low (GS 3+3) from higher grade (GS ≥3+4) disease. Standard diffusion-weighted imaging ADC maps showed a moderate overall inverse correlation with both K_{app} and MTR, but there was no observable correlation between MTR maps and DKI parameters within tumours.

A number of previous studies have looked at the ability of DKI to differentiate tumour grade compared to benign tissue in comparison with standard diffusion-weighted imaging with monoexponential modelling. DKI parameters have repeatedly been shown to distinguish benign from tumour tissue, with several studies suggesting that the kurtosis metric K outperforms ADC for differentiating low and higher grade tumours [8, 9, 21-23]. Additionally, these studies also note a strong inverse correlation of K with ADC, as supported in our data (r = -0.641), raising the question of the additional clinical benefit over existing DWI sequences, given the increased technical complexity of DKI, particularly regarding the need for complicated post-processing and interpretation. Indeed, more recent work and a large retrospective study using prostatectomy as a reference standard suggested no additional benefit of DKI sequences [10, 24]. A possible explanation is the use of a clinically-derived ADC map (using a high b-value of 1000) in these studies, in contrast to earlier work where the ADC map was derived from the DKI sequences with high b-values ranging from 1400-2000 s/mm^2. Current guidelines caution against using such high b-values

for ADC calculation due to the non-monoexponential decay at higher b-values, and due to concerns about reduced signal-to-noise ratio and noise-floor bias [4], which may have affected the performance of the ADC measurements in these studies. We also derived ADC maps from standard clinical DWI sequences, which may explain the lack of added benefit of DKI parameters.

There have been two previous studies investigating the utility of MTI in prostate cancer [15, 16]. Both were performed at 1.5T, assessed only PZ tumours, used systematic TRUS biopsy as a reference standard, and did not differentiation between Gleason grade. Of note the former study reported whole peripheral zone MTR values for tumour in the 12 patients with PCa. Our results support the findings of these studies that normal TZ and PZ tumour have a higher MTR than normal PZ. The difference in MTR between normal PZ and benign TZ is to be expected given the difference in composition of the tissue types, and the lower value may be explained by the PZ having a relatively loose stroma, a larger extracellular space, and a fluid-filled glandular cavity [25]. The mean MTR values derived here are comparable to the Arima et al study [16] for both normal TZ (26.9% vs 25.5%) and PZ tumour (25.0% vs 30.6%), but higher than the Kumar et al study (7.01% and 8.29%, respectively) [15]. Conversely our results for normal PZ (20.0%) were much higher than these two studies (8.0% and 6.15%, respectively). This discrepancy may relate to the fact that MTR is an arbitrary measure and depends on the characteristics of the pulse sequence, the Kumar study differed to ours in being a 2D sequence, with a long TR. In addition, the earlier studies may have differences **r**elate to residual haemorrhage post biopsy, which will predominantly affect the PZ rather than the TZ when systematic TRUS biopsy is performed, but will typically be excluded from areas containing cancer [26], thus only normal PZ rather than TZ or PZ

tumour will be affected. As expected, given the different values between normal PZ and TZ, zonal differentiation was readily distinguished in the majority of cases (**Figures 3.1 and 3.2**).

A number of previous studies have shown ADC to decrease as tumour Gleason grade increases, however, there tends to be a degree of overlap of values between grades [27-29]. Although there was a trend for lower ADC values in higher grade (Gleason ≥3+4) tumours in our cohort this was non-significant which may relate to the relatively small sample size, particularly within the PZ. MTR showed moderate correlation to both K_{app} (r=0.570) and D_{app} (r=-0.537) in normal tissue, yet no correlation in tumour tissue (r=0.141 and -0.024, respectively). Of note, there was a non-significant trend for increasing K_{app}, but conversely lower MTR in higher grade transition zone tumours. These divergent results combined with the poor correlation of MTI and DKI, suggest that the techniques offer different but perhaps complementary information on the tumour microenvironment. Interestingly both tumour K_{app} and MTR showed a higher inverse correlation to ADC (r=-0.444 and -0.459, respectively), suggesting that cellularity is contributing to these metrics, whilst other factors are contributing to their divergent values. At higher Gleason grades, the glandular structure of the prostate is progressively disrupted with increased cellularity and a reduction in the stromal matrix and luminal space [30]. This increased heterogeneity can therefore help to explain a trend for higher K_{app} values observed in higher grade tumours [8]. Higher grade prostate cancer is expected to result in an increased amount of intracellular bound water molecules due to increased cellular density [31], but this will be counteracted by a breakdown of the normal extensive extracellular matrix [32]. These competing processes may balance, leading to no overall change in MTR. However, histological studies directly assessing cellularity, stroma and luminal spaces would be required in order to confirm these

theories.

3.4.1 Limitations

Our study has a number of limitations. Although benefiting from a prospective design, the analysis was performed in a retrospective nature and DKI and MTI values did not inform biopsy decision making. The numbers within the cohort were relatively low, this may have particularly affected attempts to differentiate low and higher grade tumours, where further sub-division became necessary. The added value of DKI and MT imaging was not directly assessed as this would require application of a multivariate model, which was not performed due to limited numbers. The statistical testing was performed without Bonferroni corrections and the correlations described should therefore only be considered as hypothesis generating. Targeted biopsy ensured that tissue was sampled from the outlined lesion, however, as with any biopsy technique this is prone to sampling error and may misclassify grade compared to the more robust gold standard of prostatectomy. Targets were prospectively chosen based on standard clinical mpMRI sequences, this may have led to a bias towards lesions with restricted diffusion and low ADC, particularly within the PZ where this is considered the key diagnostic sequence.

We used a kurtosis model, however, other methods can be used to characterize the diffusion signal decay curve, including bi-exponential and stretched exponential models [5, 6]. The bi-exponential model separates water diffusivity into two pools, one with fast and one with slow diffusion, whilst the stretched model views water diffusion as multiple Gaussian compartments with a wide diffusivity distribution [33-35]. However, given the increased noise apparent in clinical datasets, the DKI model was chosen as this is considered

more robust, and only contains two unknown parameters (D_{app} and K_{app}) that need to be estimated [5, 36, 37]. Another consideration would be the use of multidirectional diffusion tensor imaging, which assesses the anisotropic directionality of diffusion kurtosis but requires diffusion images in at least 15 different directions [38]. Given the prohibitive scan time, this approach has been considered unnecessary for oncologic imaging in the body, with DKI typically being performed based on a directionless "trace" of the diffusion tensor [5].

3.4.2 Conclusions

In conclusion, ADC, MTI and DKI readily distinguished benign tissue from tumour, but none of the measured parameters reliably differentiated lower and higher-grade disease. Differences between DKI and MTI at higher Gleason grades may be explained by the balance between changes in cellularity, stromal matrix, and luminal space. DKI and MTI may therefore offer different but potentially complimentary information on the tumour microenvironment, with the former sensitive to alterations in tissue heterogeneity and the latter to changes in composition of the extracellular space.

3.5 References

[1] **Barrett T**, Turkbey B, Choyke PL. PI-RADS version 2: what you need to know. Clin Radiol. 2015; 70(11):1165-76

[2] National Institute for Health and Care Excellence. Prostate cancer: diagnosis and treatment. Clinical guideline 175. 2014: https://www.nice.org.uk/guidance/cg175
Last accessed 10/5/2017

[3] Hambrock T, et al. Prospective assessment of prostate cancer aggressiveness using 3-T diffusion-weighted magnetic resonance imaging-guided biopsies versus a systematic 10-core transrectal ultrasound prostate biopsy cohort. Eur Urol. 2012; 61(1):177-84

[4] Chang DT, et al. Transperineal biopsy of the prostate-is this the future? Nat Rev Urol. 2013; 10(12):690-702

[5] Rosenkrantz AB, et al. Body diffusion kurtosis imaging: Basic principles, applications, and considerations for clinical practice. J Magn Reson Imaging. 2015; 42(5):1190-202

[6] Le Bihan D. The 'wet mind': water and functional neuroimaging. Phys Med Biol. 2007; 52(7):R57-90

[7] Jensen JH, et al. Diffusional kurtosis imaging: the quantification of non-gaussian water diffusion by means of magnetic resonance imaging. Magn Reson Med. 2005; 53(6):1432-40

[8] Lawrence EM, Warren AY, Priest AN, **Barrett T**, et al. Evaluating Prostate Cancer Using Fractional Tissue Composition of Radical Prostatectomy Specimens and Pre-Operative Diffusional Kurtosis Magnetic Resonance Imaging. PLoS One. 2016; 11(7):e0159652

[9] Wang Q, et al. Histogram analysis of diffusion kurtosis magnetic resonance imaging in differentiation of pathologic Gleason grade of prostate cancer. Urol Oncol. 2015; 33(8):337e15-24

[10] Tamada T, et al. Prostate Cancer: Diffusion-weighted MR Imaging for Detection and Assessment of Aggressiveness-Comparison between Conventional and Kurtosis Models. Radiology. 2017; 284(1):100-10

[11] Henkelman RM, et al. Magnetization transfer in MRI: A review. NMR Biomed. 2001; 14(2):57-64

[12] Wolff SD, Balaban RS. Magnetization transfer imaging: practical aspects and clinical applications. Radiology 1994; 192:593-9

[13] Kurki T, et al. MR classification of brain gliomas: value of magnetization transfer and conventional imaging. Magn Reson Imaging 1995; 13:501-11

[14] Lundbom N. Determination of magnetization transfer contrast in tissue: an MR imaging study of brain tumors. AJR Am J Roentgenol 1992; 159:1279–85

[15] Kumar V, et al. Evaluation of the role of magnetization transfer imaging in prostate: a preliminary study. Magn Reson Imaging. 2008; 26(5):644-9

[16] Arima K, et al. The progress in diagnostic imaging for staging of bladder and prostate cancer:

endorectal magnetic resonance imaging and magnetization transfer contrast. Hinyokika Kiyo. 1999; 45(8):553-7
[17] **T. Barrett**, M. McLean, A. Priest, et al. Diagnostic evaluation of magnetization transfer and diffusion kurtosis imaging for prostate cancer detection in a re-biopsy population. Eur Radiol. 2017 Dec 8. doi: 10.1007/s00330-017-5169-1. [Epub ahead of print]
[18] Kuru TH, et al., Definitions of terms, processes and a minimum dataset for transperineal prostate biopsies: a standardization approach of the Ginsburg Study Group for Enhanced Prostate Diagnostics. BJU Int. 2013; 112(5): 568-77
[19] Barentsz JO, et al.; European Society of Urogenital Radiology. ESUR prostate MR guidelines 2012. Eur Radiol 2012; 22:746–757
[20] Epstein JL, et al. ISUP Grading Committee. The 2005 international society of urological pathology (ISUP) consensus conference on Gleason grading of prostatic carcinoma. Am J Surg Path 2005; 29:1228-1242
[21] Rosenkrantz AB, et al. Prostate cancer: feasibility and preliminary experience of a diffusional kurtosis model for detection and assessment of aggressiveness of peripheral zone cancer. Radiology. 2012; 264(1):126-35
[22] Suo S, Chen X, Wu L, et al. Non-Gaussian water diffusion kurtosis imaging of prostate cancer. Magn Reson Imaging 2014; 32(5):421–427
[23] Tamura C, et al. Diffusion kurtosis imaging study of prostate cancer: preliminary findings. J Magn Reson Imaging. 2014; 40(3):723-9
[24] Roethke MC, et al. Evaluation of Diffusion Kurtosis Imaging Versus Standard Diffusion Imaging for Detection and Grading of Peripheral Zone Prostate Cancer. Invest Radiol. 2015; 50(8):483-9
[25] Wang XZ, et al. Diffusion-weighted imaging of prostate cancer: correlation between apparent diffusion coefficient values and tumor proliferation. J Magn Reson Imaging 2009; 29:1360-6
[26] **Barrett T**, Vargas HA, Akin O, Goldman DA, Hricak H. Value of the hemorrhage exclusion sign on T1-weighted prostate MR images for the detection of prostate cancer. Radiology. 2012; 263(3):751-7
[27] Hambrock T, et al. Relationship between apparent diffusion coefficients at 3.0-T MR imaging and Gleason grade in peripheral zone prostate cancer. Radiology. 2011; 259(2):453-461
[28] **Barrett T**, Priest AN, Lawrence EM, et al. Ratio of Tumor to Normal Prostate Tissue Apparent Diffusion Coefficient as a Method for Quantifying DWI of the Prostate. AJR Am J Roentgenol. 2015; 205(6):W585-93
[29] Donati OF, et al. Prostate Cancer Aggressiveness: Assessment with Whole-Lesion Histogram Analysis of the Apparent Diffusion Coefficient. Radiology. 2014; 271(1):143-145
[30] Epstein JI, et al; ISUP Grading Committee. The 2005 International Society of Urological Pathology (ISUP) Consensus Conference on Gleason grading of prostatic carcinoma. Am J Surg Pathol

2005;29(9):1228-42
[31] Jia G, et al. Amide proton transfer MR imaging of prostate cancer: a preliminary study. J Magn Reson Imaging. 2011; 33(3):647-54
[32] Takayama Y, et al. Amide proton transfer (APT) magnetic resonance imaging of prostate cancer: comparison with Gleason scores. MAGMA. 2016; 29(4):671-9
[33] Niendorf T, et al. Biexponential diffusion attenuation in various states of brain tissue: implications for diffusion- weighted imaging. Magn Reson Med 1996; 36(6):847-857
[34] Bourne RM, et al. Information theoretic ranking of four models of diffusion attenuation in fresh and fixed prostate tissue ex vivo. Magn Reson Med 2014; 72:1418-1426
[35] Toivonen J, et al. Mathematical models for diffusion-weighted imaging of prostate cancer using b values up to 2000 s/mm: Correlation with Gleason score and repeatability of region of interest analysis. Magn Reson Med. 2015; 74(4):1116-24
[36] Le Bihan D. Apparent diffusion coefficient and beyond: what diffusion MR imaging can tell us about tissue structure. Radiology 2013; 268:318-322
[37] Iima M, et al. Quantitative non-Gaussian diffusion and intravoxel incoherent motion magnetic resonance imaging: differentiation of malignant and benign breast lesions. Invest Radiol 2015; 50:205-211
[38] Jensen JH, et al. Diffusional kurtosis imaging: the quantification of non-Gaussian water diffusion by means of magnetic resonance imaging. Magn Reson Med 2005; 53: 1432-1440

Chapter 4: Quantification of total and intracellular tumour sodium concentration in prostate cancer patients

4.1 Introduction

Standard clinical MRI provides information about the distribution and environment of hydrogen nuclei, and is termed ^{1}H-MRI. As hydrogen in tissues is most abundant in water, ^{1}H-MRI largely measures the distribution of water in tissues. However, MRI can also be used to detect several nuclei other than hydrogen which are MR-active, for example: ^{13}C, ^{15}N, ^{31}P, ^{19}F. The images produced from these different nuclei (known generically as "X-nuclei" MRI) allow for other physical and metabolic processes to be studied in the human body.

Sodium (^{23}Na) MRI is a technique which aims to image this vital intra- and extracellular ion. ^{23}Na produces the second strongest MRI signal among all nuclei present in biological tissues given the abundance of sodium in vivo. However, the MRI sensitivity for sodium is around 9.2% of protons and sodium concentration in vivo is around 2,000 times lower than the concentration of protons, resulting in signal-to-noise (SNR) ratios up to 20,000 times lower than ^{1}H-MRI [1]. In addition, the short biexponential transverse relaxation time arising from the 3/2 spin of the quadrupolar nucleus produces further challenges in acquiring images with sufficient SNR, making ^{23}Na-MRI a challenging technique [2]. This SNR deficit has been partly overcome by new techniques and higher-field strength magnets, allowing acquisition in a reasonable time frame (10 to 15 minutes) and with a resolution of a few millimetres, making ^{23}Na-MRI a viable addition to existing ^{1}H-MRI protocols [3]. Typically tissue sodium concentration (TSC) is measured, which represents a combination of the volume fraction weighted mean of the intracellular and extracellular sodium concentrations.

Sodium is an essential component of cellular metabolism and is actively exchanged via the Na/K and Na/H pumps to maintain intracellular pH. Normal intracellular levels of sodium are 10 fold lower than extracellular concentrations. Changes in tissue sodium have been shown to occur in a wide range of disease processes including inflammation, ischaemia and in several tumour types [4-6]. Typically tissue sodium concentration (TSC) is measured, which represents a combination of the volume fraction weighted mean of the intracellular sodium concentration and the extracellular sodium concentration. There are a number of reasons why tumours will demonstrate a high TSC, but mainly because many cellular processes and interactions in excitable tissues depend on the maintenance of a low intracellular and high extracellular sodium concentration [7]. This gradient is maintained by the transmembrane sodium-potassium pump, powered by adenosine triphosphate (ATP), as well as other transporters. If the supply of ATP is insufficient due to impaired cellular energy metabolism, or if the cell membrane integrity is disrupted, then the intracellular sodium concentration will rise [8, 9]. Furthermore, proliferating cells have high intracellular sodium content secondary to increased activity of the Na^+/H^+ exchanger in the presence of reduced pH secondary to hypoxia and increased lactate [10, 11]. In addition, extracellular sodium will increase due to tumour neovascularization and an increase in the tumour interstitial space [12]. Thus, increases in both intracellular sodium concentration and extracellular volume can contribute to an increase in TSC and the measurement is sensitive to changes in both the metabolic state of tissues and integrity of cell membranes.

Studying the sodium levels in prostate cancer could provide complementary information to traditional ^{1}H-MRI. Previous ^{23}Na-MRI studies on the prostate in man are limited, with only 3

published studies incorporating healthy volunteers and a further study investigating 3 patients with biopsy-proven prostate cancer which did not quantify the tumour sodium concentration [13-16]. The aim of this work was to measure the tissue concentration of sodium within tumours and background normal prostate in patients with prostate cancer, using pathology from prostatectomy as the gold standard.

4.2 Methods

4.2.1 Patient Population

The local institutional review board and ethics committee granted approval for this prospective study (CUH/16/EE/0205), with all participants signing written informed consent. 15 patients with biopsy-proven intermediate or high risk prostate cancer underwent a dedicated research MRI prior to treatment with radical prostatectomy. Exclusion criteria included previous treatment for prostate cancer, or a clinical contraindication to MRI.

4.2.2 Imaging of Phantoms

In order to quantify tissue sodium concentration (TSC), it is necessary to image calibration markers containing known sodium concentrations. Imaging was performed using a dedicated dual-tuned $^{1}H/^{23}Na$ receiver endorectal coil (ERC; GE Healthcare, Waukesha, WI) [17]. Initial phantom work was undertaken to determine the ERC reception profiles in order to inform interpretation of sodium maps in vivo, with a phantom replacement method used to create a calibration curve. The ERC was placed in the centre of an arrangement of 5 x 50 ml Falcon tubes, with the content of NaCl in 4 % agar phantoms varying between 7 and 160 mM/L NaCl. This was used to create a calibration curve which was applied to the in vivo data to create sodium maps [18]. Images were acquired using both ERC as “receive” coil for ^{23}Na and also a standard “body coil” as receive-coil for “^{1}H” (standard clinically-used proton imaging); **Figure 4.1**.

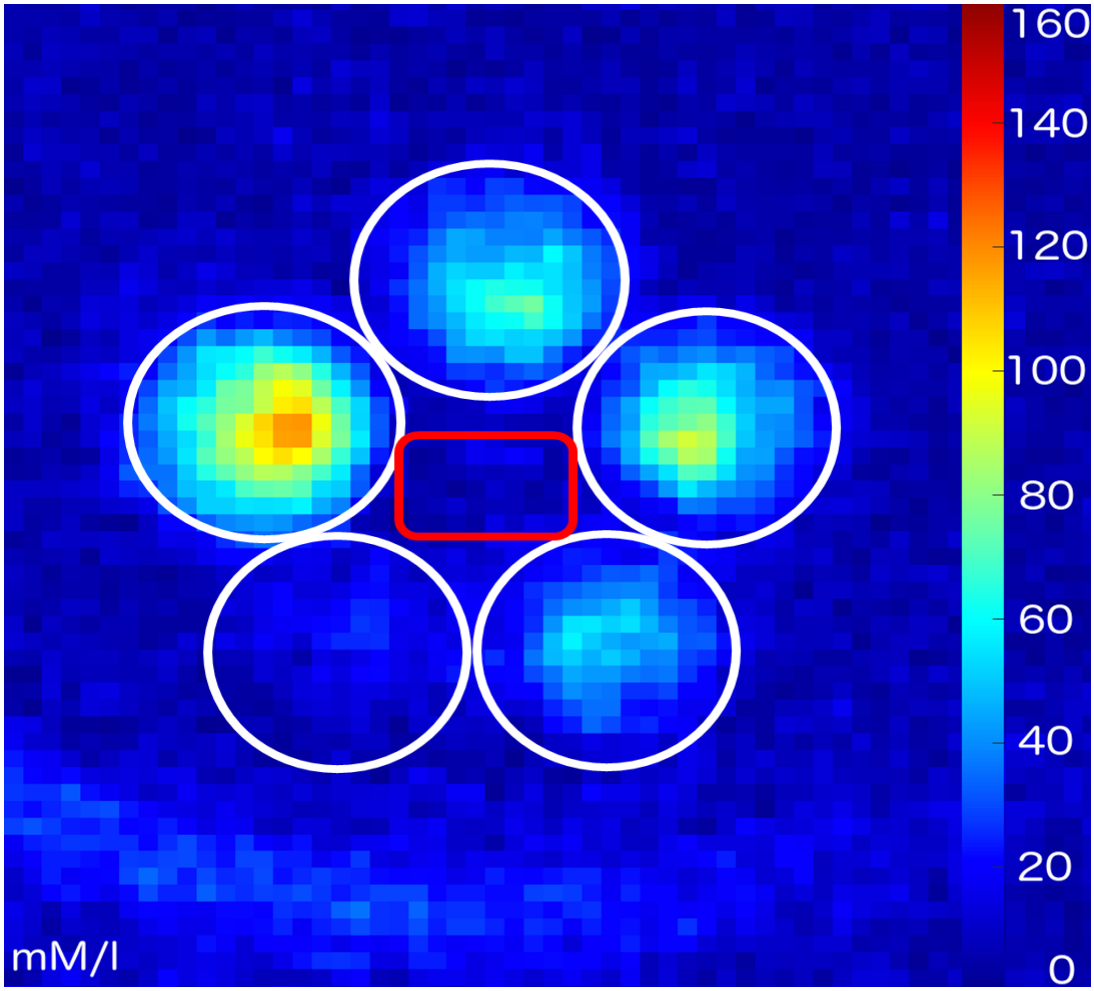

4.1 Phantom Imaging. A phantom replacement method was used to create a calibration curve against 5 NaCl in 4 % agar phantom tubes varying between 7 and 160 mM/l NaCl (indicated by circular outlines), with the sodium-endorectal coil placed centrally (red outline).

4.2.3 Magnetic Resonance Imaging

All phantom experiments and clinical imaging was performed on a clinical 3T system (GE MR750, GE Healthcare, Waukesha, WI) using a dedicated ^{13}C clamshell exciter (GE Healthcare, Waukesha, WI) and a dual-tuned $^{1}H/^{23}Na$ receiver ERC.

Sodium imaging was performed using a 3D cones [19, 20] sequence with the following imaging parameters: TE = 0.5 ms, TR = 60 ms, FOV = 30 cm, nominal resolution 2.35 x 2.35 x 4 mm, 12 NEX, 6468 total readouts, 7 minutes acquisition duration. For region of interest (ROI) outlining, ^{1}H FRFSE T2-weighted anatomical images were acquired using the following parameters: TE = 105 ms, TR = 2500 ms, FOV = 30 cm, resolution 0.5 x 0.5 x 4 mm.

4.2.3.1 Intracellular sodium measurements

For intracellular-weighted imaging, the sodium sequence was repeated with the addition of a 5.6 ms adiabatic inversion pulse with inversion time (TI) = 30 ms, TR = 120 - 210 ms, resolution and FOV as before, 10 NEX, 5390 total readouts, 11 – 19 minutes acquisition duration. For the inversion recovery sodium imaging, TR and therefore total acquisition duration was varied due to specific absorption ratio (SAR) limitations. Sodium images were corrected for receive sensitivity by dividing the images by a heavily smoothed duplicate of themselves (Gaussian kernel, sigma = 5) [21]; **Figure 4.2**.

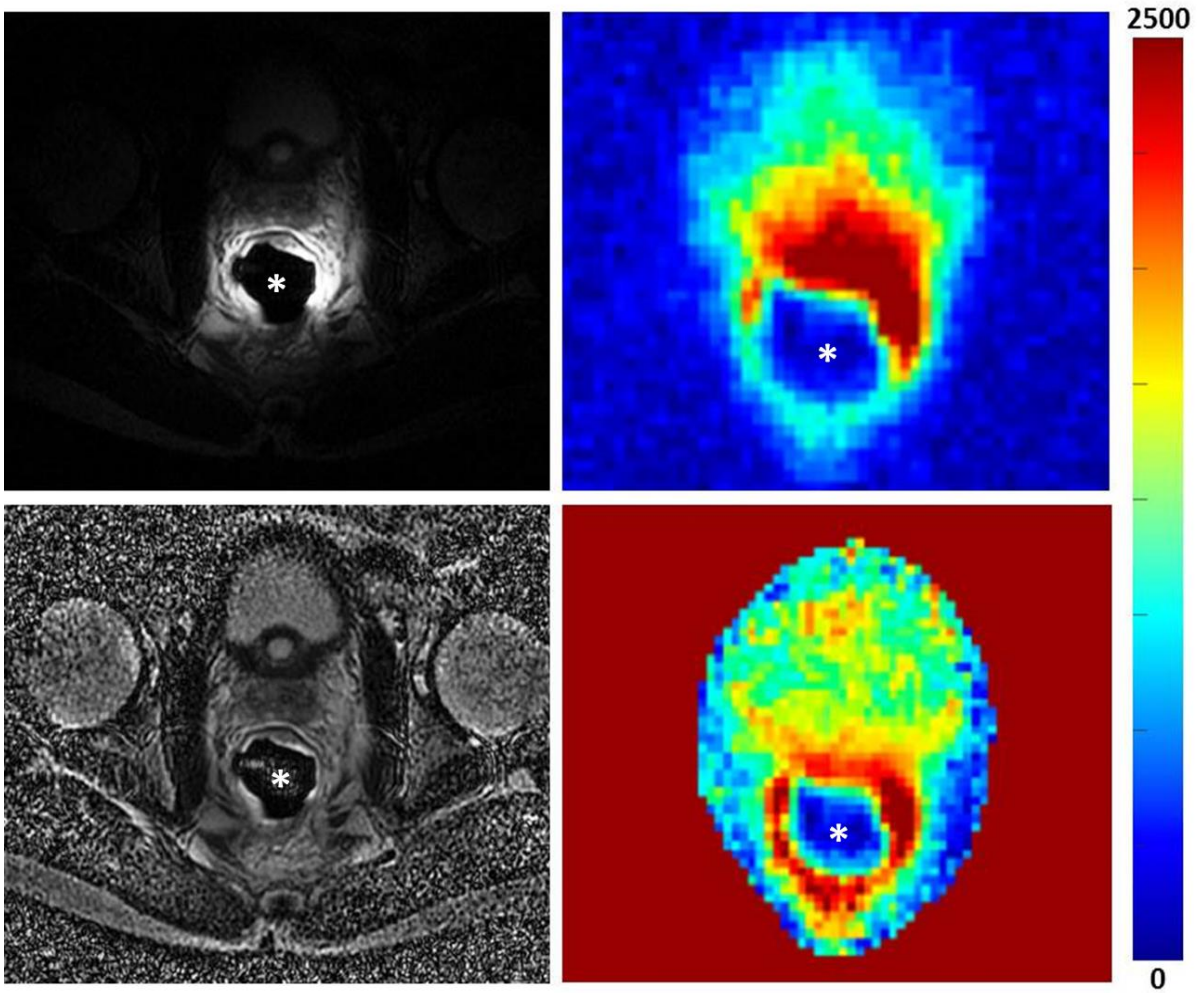

Figure 4.2. Sensitivity-corrected images. Proton T2-weighted image (top row) and TSC images (bottom row) of the prostate, with endorectal coil in situ (*). The uncorrected images (left) were adjusted for receive sensitivity by dividing the images by a heavily smoothed duplicate of themselves to create the corrected images (right). Images displayed at full dynamic range. Colour scale is an arbitrary measure of signal intensity due to sensitivity correction being performed prior to the maps being generated.

The Inversion Recovery (IR) technique for assessing intracellular sodium is based on sodium nuclei having a significantly longer T1 relaxation time in the extracellular fluid space as compared to intracellular sodium, meaning IR can be used to weight the contribution of sodium signal from either environment [22 - 24].

4.2.4 Histopathology assessment

Prostatectomy specimens were fixed in formalin and oriented by the location of the seminal vesicles, posterior surface of the prostate, and by the position of the urethra. The apical cone was amputated, and sliced into 4 mm sections from left to right, the remaining gland was cut transversely into 5 mm whole-mount parallel slices in the horizontal plane from inferior to superior. Representative 5 µm microtome slides were processed from each 5 mm whole-mount slices for histopathological analysis. Tumour was outlined on hematoxylin and eosin (H&E) stained sections from each slice by an experienced uropathologist specializing in prostate cancer.

4.2.5 Correlation of histopathology to imaging

A radiologist with 7-years' experience reporting clinical prostate MRI used the histopathological tumour maps in conjunction with the available diagnostic MRI datasets to outline the peripheral zone (PZ), transition zone (TZ) and tumour. The tumour location from histopathological slides was manually copied as a region-of-interest (ROI) onto the T2-weighted anatomical image acquired using the ERC. ROIs of a minimum volume of 0.5 cm^3 were additionally drawn on at least 3 consecutive slices for normal TZ and PZ, with care taken to avoid partial volume effects from the urethra, bladder, seminal vesicles, and extra-prostatic tissue, and at the zonal interface. Separately, in order to assess whether the

reduced SNR in the anterior gland affected estimates of sodium concentration, ROIs in all patients were drawn in the anterior half and posterior half of the TZ. ROIs based on these outlines were then copied to the co-localised sodium images using OsiriX 8.5.1 (Pixmeo SARL, Bernex, Switzerland).

4.2.6 Statistics

A balanced one-way ANOVA was performed to compare the results from each patient for normal PZ, normal TZ and tumour ROIs, using Tukey's test for multiple comparisons. A two-sided Wilcoxon rank sum test was used to assess for differences in sodium values between tumour grades. A p-value of < 0.05 was considered statistically significant.

4.3 Results

All scans were acquired without complications. 15 patients were included in the study group, with a median age of 59.5 years (mean 60.7, range 48 - 73 years) and a median pre-biopsy PSA level of 8.4 ng/mL (mean 9.79, interquartile range 6.125 - 11.6 ng/mL); **Table 4.1**. The average time between diagnostic prostate biopsy and MRI was 89.6 days (range 43 – 179 days). 8 patients underwent MRI scanning on the day of surgery, the mean time from MRI to surgery was 5 days (range 0 - 31 days).

Characteristic	**Value**
Patient age, years	59.5 (56.25 – 64.5)
PSA level, ng/mL	8.4 (6.125 – 11.6)
Pathological tumour volume, cm^3	3.25 (1.54 – 6.76)
Final lesion Gleason score (n = 17)	
3+3	1
3+4	7
4+3	5
3+5	2
4+4	0
≥9	2
Pathologic tumour stage (n = 15)	
T2a	0
T2b	1
T2c	3
T3a	10
T3b	1

Table 4.1. Patient Characteristics. Median values listed, Inter-quartile range in parenthesis

17 tumours were detected in the 15 patients imaged, with pathology Gleason score 3+3 (n = 1), 3+4 (n = 7), 3+5 (n = 2), 4+3 (n = 5), and 4+5 (n = 2). The mean tumour size at final pathology was 4.37 cm^3 (range 0.09 – 15.78 cm^3). Two patients had significant artefact on the sodium imaging and had to be excluded (Gleason 3+4 and 4+5 tumours), and in one further patient, intracellular weighted sodium data could not be acquired due to a software fault (Gleason 3+4 tumour).

The average tissue sodium concentration (TSC) was significantly higher in the normal peripheral zone at 39.2 mmol/L (range 34.2 – 42.5) compared to the normal transition zone 32.9 mmol/L (range 28.4 – 39.5); $p < 0.001$, **Figure 4.3**. The mean TSC for all tumours was 43.1 mmol/L and for PZ tumours was 45.0 mmol/L (range 38.5 – 50.9); **Table 4.2, Figure 4.4**. Overall 11/13 peripheral zone tumours demonstrated a higher TSC than the corresponding normal PZ on the contralateral side of the gland and there was a significant difference between PZ tumour compared to both the normal PZ ($p < 0.001$) and normal TZ ($p < 0.001$); **Figure 4.5**. 2 of 15 tumours were location in the TZ and demonstrated a mean TSC of 30.6 and 33.2 mmol/L, respectively with both TZ lesions having a slightly lower TSC than the corresponding normal TZ.

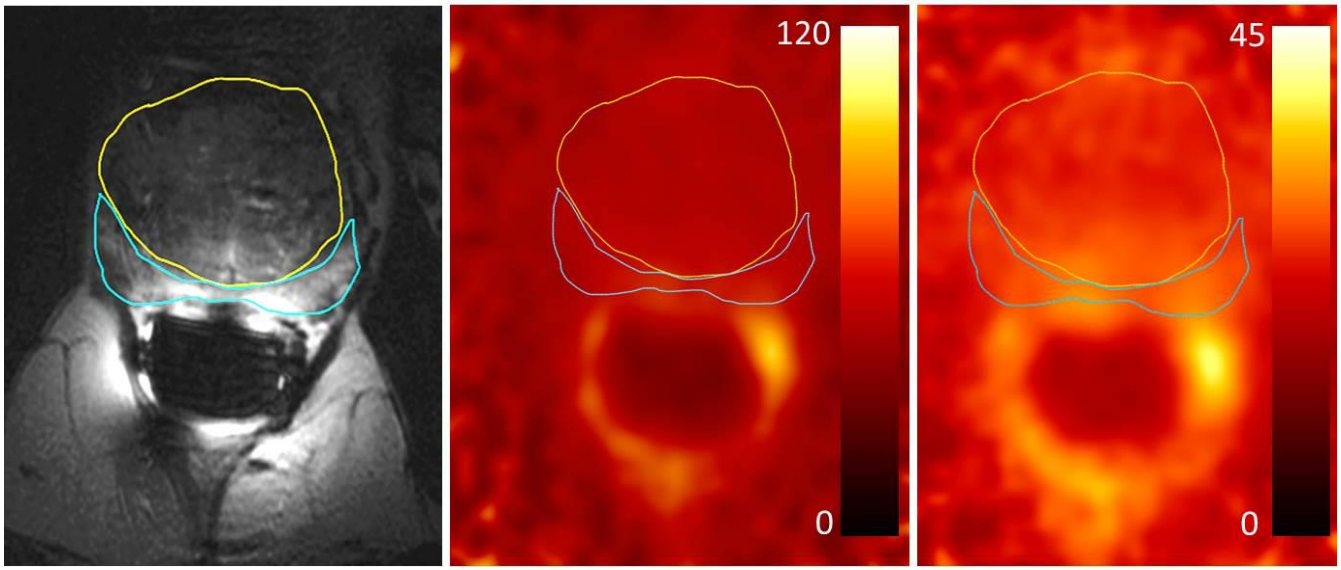

Figure 4.3. Sodium concentration in the normal PZ and TZ. 58 year old man, PSA 18.69 ng/mL with a pathologically proven Gleason 3+5 tumour in the left apex TZ (not shown). Regions of interest outline normal peripheral zone (blue) and normal transition zone (yellow) of the prostate; endorectal coil in situ. Left: T2-weighted axial image. Middle: Map of tissue sodium concentration (TSC). Right: Map of intracellular sodium concentration. The mean TSC and intracellular sodium concentrations were 40.6 and 10.2 mmol/L in the PZ, and 32.7 and 7.9 mmol/L in the TZ, respectively.

Patient	Normal TZ	Normal PZ	Tumour location	Tumour	Tumour volume	Gleason Grade
1	32.7 (± 0.8)	40.6 (± 2.6)	TZ	30.6 (± 1.0)	7.51	3+5
3	34.2 (± 0.8)	39.4(± 2.6)	PZ	49.4 (± 4.6)	2.29	3+4
4 (lesion 1)	33.4 (± 1.1)	41.7(±.3.0)	TZ	30.8 (± 1.8)	6.50	3+4
4 (lesion 2)	-	-	PZ	47.5 (± 5.7)	0.29	3+4
5	28.4 (± 1.4)	40.1 (± 2.2)	PZ	46.2 (± 1.4)	3.56	3+4
6	39.5 (± 1.1)	37.4 (± 1.5)	PZ	47.5 (± 1.4)	3.18	4+3
8	33.0 (± 2.0)	41.2 (± 2.2)	PZ	50.9 (±0.4)	3.25	4+3
9	29.1 (± 1.7)	36.2 (± 4.0)	PZ	38.5 (± 1.6)	0.79	3+4
10	32.7 (± 2.3)	39.4 (± 1.9)	PZ	44.6 (± 2.9)	0.70	4+3
11	33.5 (± 1.3)	37.9 (± 2.9)	PZ	41.1 (± 2.4)	15.78	3+4
12	31.5 (± 1.6)	37.9 (± 0.9)	PZ	41.8 (± 0.8)	2.29	4+3
13 (lesion 1)	32.1(± 1.4)	34.2 (± 2.0)	PZ	43.6 (± 3.8)	3.85	3+3
13 (lesion 2)	-	-	PZ	48.0 (± 2.7)	0.09	3+5
14	35.8(± 0.38)	42.4 (± 3.3)	PZ	46.9 (± 0.4)	1.12	4+5
15	32.2(± 2.4)	40.8 (± 1.7)	PZ	39.6 (± 2.2)	4.99	4+3
Group mean	32.9	39.2	-	43.1	3.75	-

Table 4.2. Tissue Sodium Concentration (in mml/L) for normal and tumour tissue; standard deviation in parenthesis. Patients 2 and 7 excluded due to artefact. TZ = transition zone, PZ = peripheral zone.

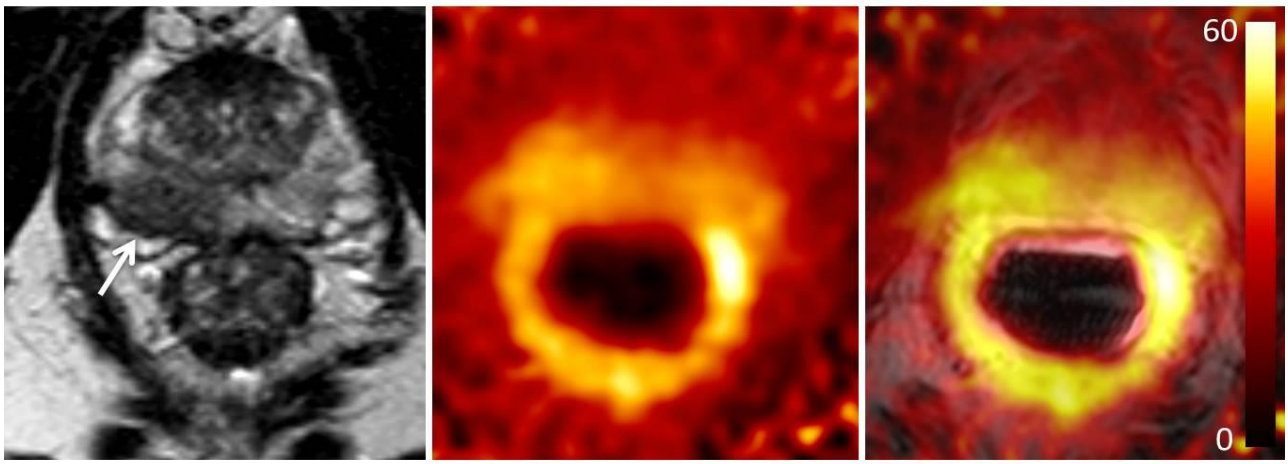

Figure 4.4. Sodium concentration in PZ tumour. 63 year old man, PSA 8.4 ng/mL with a 20 mm pathologically proven Gleason 4+3 tumour in the right mid PZ, with focal extracapsular extension (arrow in diagnostic T2-weighted image of the prostate, left); endorectal coil in situ. Middle: TSC map; right: TSC map overlaid on T2 image. The mean TSC and intracellular sodium concentrations in the lesion were 41.8 and 19.2 mmol/L, compared to 37.9 and 17.1 mmol/L in the normal PZ, respectively.

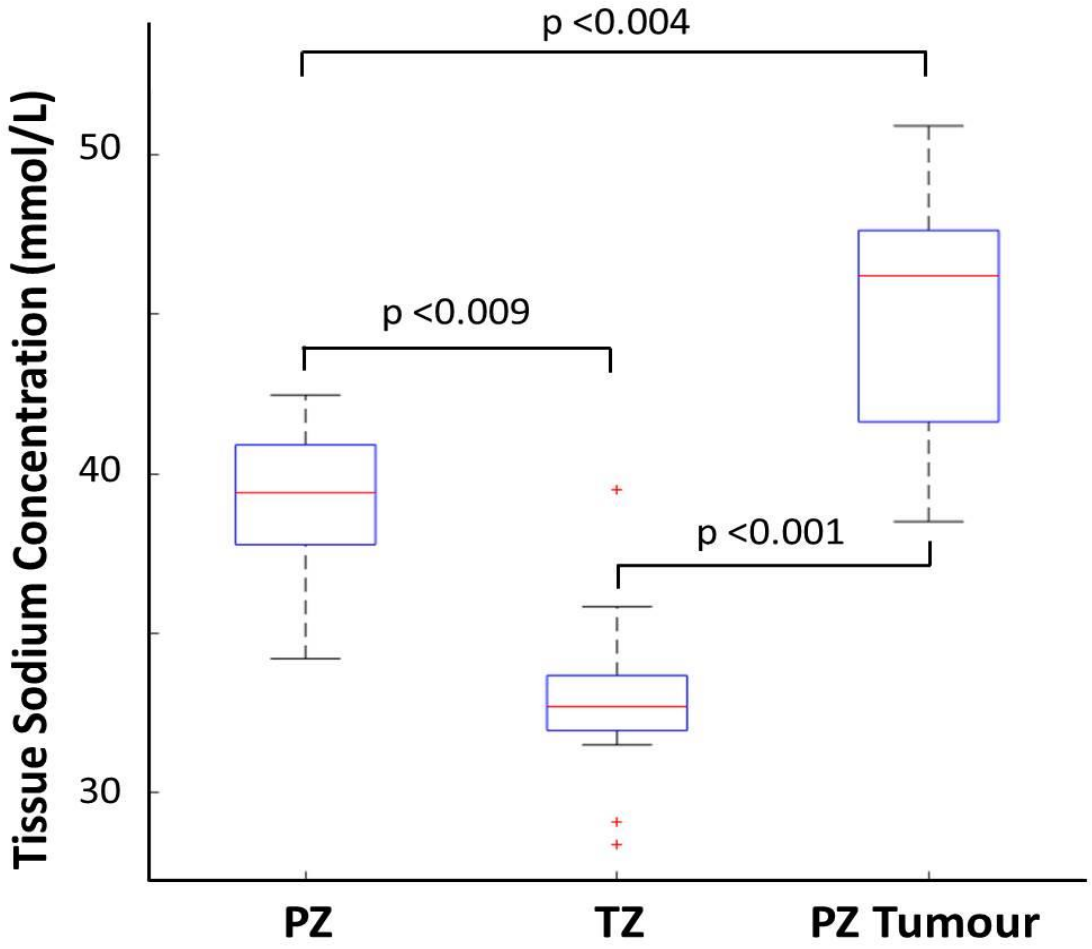

Figure 4.5. Box and whiskers plot of the tissue sodium concentration in normal and PZ tumour tissue. Top and bottom of boxes represent 25th and 75th percentiles of, lines in boxes represent the median value and bars represent the data within 1.5 times interquartile range, + denotes outliers. P-values between groups as indicated. PZ: normal peripheral zone; TZ: normal transition zone.

The mean intracellular-weighted sodium was also significantly higher in the normal PZ (17.5 mmol/L, range 10.2 – 21.4) compared to the normal TZ (14.7 mmol/L, range 7.9 – 18.0; p = 0.02). The average intracellular-weighted sodium for all tumours was 18.7 mmol/L and for PZ tumours was 19.9 mmol/L (range 15.8 – 22.3). Overall 9/12 PZ tumours demonstrated a higher intracellular sodium compared to the normal PZ on an individual patient level but this did not reach significance (p = 0.05); however, there was a significant difference between the PZ tumour tissue and the normal TZ (p < 0.001); **Figure 4.6**. Both TZ lesions had slightly higher intracellular sodium values than the normal TZ; **Table 4.3**.

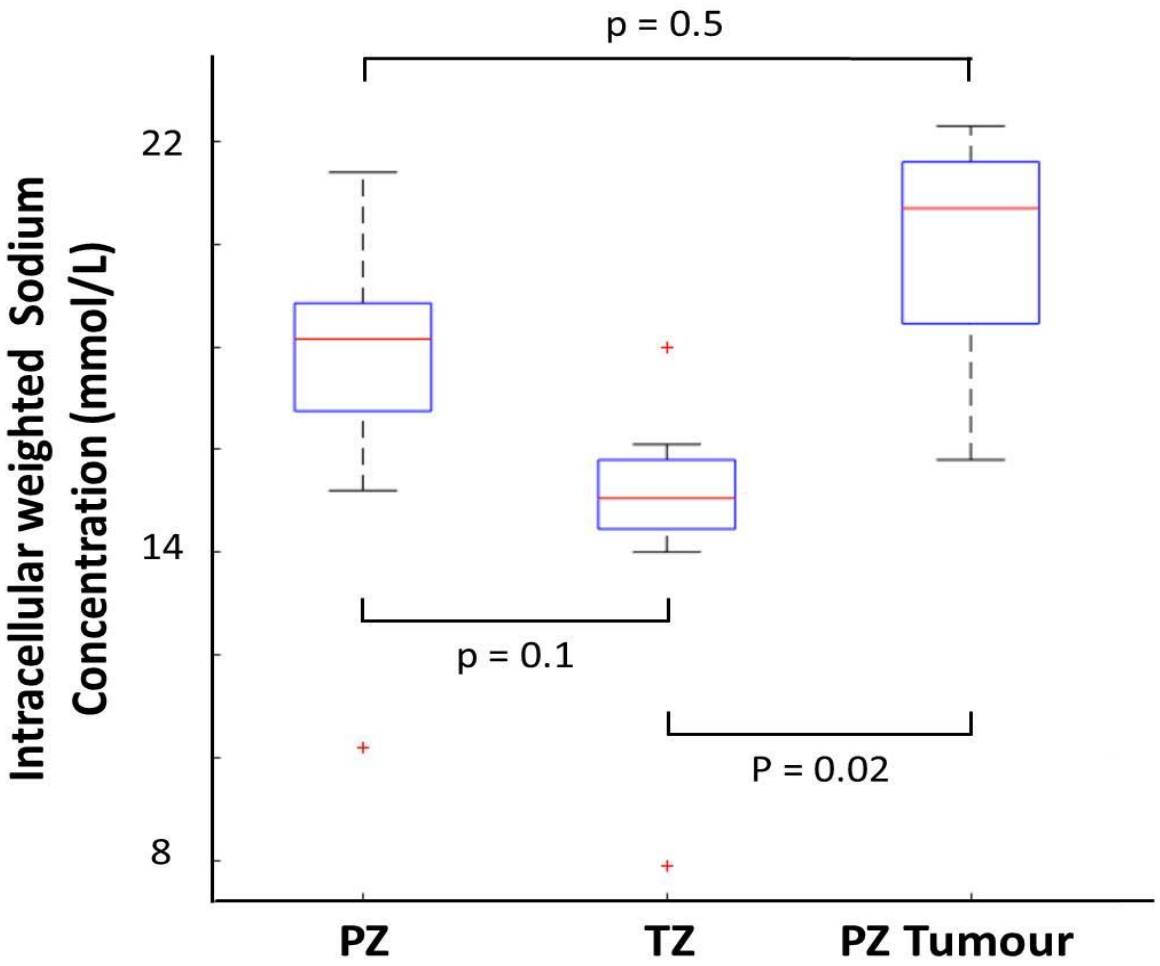

Figure 4.6. Box and whiskers plot of intracellular weighted sodium concentration in normal and PZ tumour tissue. Top and bottom of boxes represent 25th and 75th percentiles of data, lines in boxes represent the median value and bars represent the data within 1.5 times the interquartile range, + denotes outliers. P-values between groups as indicated. PZ: normal peripheral zone; TZ: normal transition zone.

Patient	Normal TZ	Normal PZ	Tumour location	Tumour	Tumour volume	Gleason Grade
1	7.9 (± 2.5)	10.2 (± 3.2)	TZ	8.6 (± 3.1)	7.51	3+5
3	16.1 (± 0.3)	18.1 (± 1.1)	PZ	21.5 (± 1.1)	2.29	3+4
4 (lesion 1)	14.6 (± 0.7)	18.4 (± 1.0)	TZ	14.7 (± 2.8)	6.50	3+4
4 (lesion 2)	-	-	PZ	20.8 (± 2.7)	0.29	3+4
6	16.0 (± 1.3)	18.2 (± 2.0)	PZ	20.6 (± 1.2)	3.18	4+3
8	14.7 (± 0.9)	16.4 (± 1.4)	PZ	21.9 (± 0.2)	3.25	4+3
9	14.0 (± 1.0)	15.2 (± 2.3)	PZ	15.8 (± 3.3)	0.79	3+4
10	15.6 (± 1.3)	19.0 (± 1.2)	PZ	19.2 (± 0.8)	0.70	4+3
11	15.1 (± 1.1)	21.4 (± 1.4)	PZ	17.7 (± 0.5)	15.78	3+4
12	14.3 (± 0.8)	17.1 (± 0.6)	PZ	19.2 (± 0.2)	2.29	4+3
13 (lesion 1)	15.0 (± 0.7)	17.6 (± 1.0)	PZ	21.7 (± 2.1)	3.85	3+3
13 (lesion 2)	-	-	PZ	21.2 (± 2.7)	0.09	3+5
14	18.0 (± 0.3)	17.6 (± 1.0)	PZ	22.3 (± 0.5)	1.12	4+5
15	15.3 (± 1.4)	17.6 (± 1.0)	PZ	17.3 (± 0.4)	4.99	4+3
Group mean	14.7	17.5	-	18.7	3.76	-

Table 4.3. Intracellular weighted Sodium Concentration (in mmol/L) for normal and tumour tissue; standard deviation in parenthesis. Patients 2 and 7 were excluded due to artefact; the intracellular weighted imaging was excluded for patient 5 due to software acquisition error. TZ: transition zone, PZ: peripheral zone.

Regional assessment of the differences in signal between the anterior and posterior gland showed a significant variation. The mean TSC value in the anterior TZ was 30.51 mmol/L (± 1.67) compared to 33.48 mmol/L (± 1.86) in the posterior TZ; p = 0.004. The mean intracellular sodium value was 14.32 mmol/L (± 0.82) in the anterior TZ, compared to 15.53 mmol/L (± 1.06) in the posterior TZ; p = 0.08.

A comparison between tumour grade and sodium concentration was also performed. For peripheral zone lesions, 7 patients had 3+3 or 3+4 tumours, and 6 patients had tumours with grade ≥Gleason 4+3. The mean TSC was lower in those with Gleason ≤3+4 (44.4 mmol/L) compared to those with ≥4+3 (45.6 mmol/L), but this was not statistically significant; p = 0.19. Likewise, there was no significant difference in mean intracellular sodium between low grade and higher grade tumours: 19.5 mmol/L (Gleason ≤3+4) and 20.2 mmol/L (≥4+3); p = 0.29.

4.4 Discussion

This study demonstrated the ability to quantify tissue sodium concentration (TSC) and intracellular sodium concentration in both tumours and normal prostate tissue. TSC has previously been quantified in the normal PZ and TZ of both volunteers and patients. Here we demonstrate sodium imaging at a higher spatial resolution than previously achieved and quantify both TSC and intracellular sodium concentrations within prostate tumours for the first time. We have shown a significant increase in total tissue sodium concentration in tumours compared to normal tissue, and a higher intracellular sodium in tumours compared to normal TZ.

We found a significant difference between intracellular sodium in normal PZ and TZ (17.5 and 14.7 mmol/L, respectively). The values measured are within the expected range for other tissues, with intracellular sodium concentration reported to be around 10 - 15 mmol/L [1, 25, 26]. It is possible that the higher values demonstrated in the normal PZ may reflect differences in cellularity and sodium gradients across the membrane between the tissues, with more metabolically active PZ cells requiring more nutrients [14]. Previous studies support our findings of a higher tissue sodium concentration in normal PZ compared to TZ [13, 14, 16]. These studies show a wide range in normal PZ TSC concentration from 40.4 - 70.5 mmol/L and TZ from 28.3 - 60.2 mmol/L, which may relate to technical differences, spatial resolution and/or the effects of partial voluming. We found the mean concentrations in the PZ and TZ of our study population to be at the lower end of this range (39.2 and 32.9 mmol/L, respectively). Physiologically, extracellular sodium concentration (140 - 150 mmol/L) is an order of magnitude higher than intracellular sodium concentration; however, the extracellular volume fraction (including vessels) accounts for only around 20% of total

tissue volume [1, 26]. The higher percentage contribution of intracellular sodium would therefore give an expected TSC in the range of 36 - 42 mmol/L within normal tissues and is therefore supportive of our measurements. It is not unexpected that TSC levels differ between normal PZ and TZ, given the differing composition of their respective tissues, with the normal PZ having a glandular structure with an extensive duct system, a relatively loose stroma, and a larger extracellular space [27 - 29]. Furthermore, Hausmann et al [13] showed that TSC measurements of the normal PZ and TZ correlated to their respective ADC measurements. Although the young age of the volunteers imaged (26 - 34 years) may limit the applicability of the findings in the TZ of this population to patients who are usually older, the results support a relationship between the increased extracellular space of the glandular PZ (and free diffusion of water) and higher concentrations of sodium in normal prostatic tissue. Of note, we found a small, but significant difference in TSC but not intracellular sodium between the posterior and anterior TZ, which may relate to reducing SNR with increasing distance from the coil.

We demonstrated significantly higher TSC in PZ tumours compared to both normal PZ and normal TZ. Such a result demonstrates that the change in sodium concentration in tumours is measuring more than a simple change in cellularity: tumours have a higher cell density compared to the normal PZ, as demonstrated by ADC, but given that intracellular sodium is significantly lower than extracellular sodium, cellular changes alone would lead to a reduction and not an increase in TSC. Intracellular sodium in peripheral zone tumours was higher than normal PZ and TZ, but only reached significance when compared to the TZ; this could be a reflection of changes in cellularity alone. Taken together, these results are suggesting that there is an increase in extracellular sodium concentration in PZ tumours.

Interestingly, the two TZ tumours imaged demonstrated lower sodium concentrations, this may be partly explained by the drop-off in SNR with increasing distance to the coil, with PZ tumours unlikely to be affected due to their relative proximity to the coil. However, the lower values relative to normal TZ suggest this is a genuine finding and indicative of a different sodium environment in TZ versus PZ tumours. Indeed, TZ tumours have been described as having morphological differences to PZ tumours, having well-differentiated glands of variable size and being lined by columnar cells with a clear cell histological pattern [30, 31]. However, the number of TZ lesions in the cohort is small and further investigation is warranted.

In healthy tissues, the large sodium concentration gradient between intra and extracellular sodium is maintained by several transporters and pumps, the most important being Na^+/K^+-ATPase [32]. Therefore, a potential advantage of sodium imaging over proton MRI is the ability to provide functional information relating to tissue viability, cell membrane integrity, and energetic status of the cellular environment. In tumours, changes in TSC may reflect both increases in intra- and extracellular sodium as well as changes in the size of each compartment. Increases in cell density will reduce the extravascular extracellular space and TSC will be weighted towards the low concentration sodium from the intracellular compartment. Conversely, an increased interstitial space will increase the extracellular weighting of the TSC measurement. Intracellular sodium in tumour cells may rise when demand for ATP exceeds production, limiting the ability of the Na^+/K^+-pump to maintain the sodium gradient or due to over-activity of the Na^+/K^+-pump to compensate for the low pH of the tumour microenvironment induced by hypoxia and increased lactate [1, 10, 11]. TSC has been shown to be elevated in several tumour types and has the potential to demonstrate

treatment response in a number of conditions such as breast cancer [33], murine models of prostate cancer [34], and successful ablation of uterine fibroids [35]. There may be several potential applications for sodium-MRI in prostate cancer, including primary tumour localization and characterization in select cohorts, monitoring treatment response to oncological agents and detecting local recurrence following radical therapy. Furthermore, any treatment that causes cell death or loss of membrane integrity such as ablative focal therapy techniques, several of which are being trialed in prostate cancer, could be monitored with sodium MRI.

4.4.1 Limitations

Our study has some limitations. The patient numbers were relatively small for this exploratory study, and TZ tumours were under-represented in the cohort. The selection bias of patients undergoing prostatectomy limits the ability to differentiate grade type in this cohort, with an over-representation of Gleason 3+4 and 4+3 disease. Patients were selected on the basis of lesions detectable on standard clinical prostate mpMRI and therefore the added value of the technique for detecting lesions de novo was not assessed. We did not correlate TSC with ADC measurements derived from diffusion-weighted imaging. Although previous work demonstrated a correlation between TSC and ADC in normal prostatic tissue, our results suggest that these values are likely to be divergent in tumour tissue, but warrants further investigation. The detection of sodium signal in vivo remains challenging and improvements in hardware and software and/or increasing magnet strength are needed to help improve SNR and resolution and reduce acquisition times and make this promising technique more clinically available.

4.4.2 Conclusions

In conclusion, we have successfully quantified the tissue and intracellular concentrations of prostate tumours in vivo, demonstrating a significant increase in TSC within PZ tumours, and highlighting the potential of this non-invasive functional imaging technique in the investigation of patients with prostate cancer.

4.5 References

[1] Madelin G, Regatte RR. Biomedical applications of sodium MRI in vivo. J Magn Reson Imaging. 2013; 38(3):511-29

[2] Thulborn KR, et al. Comprehensive MR imaging protocol for stroke management: tissue sodium concentration as a measure of tissue viability in nonhuman primate studies and in clinical studies. Radiology 1999; 213:156–166

[3] Ouwerkerk R. Sodium MRI. Methods Mol Biol. 2011; 711:175-201

[4] Ouwerkerk R, et al. Tissue sodium concentration in human brain tumors as measured with 23Na MR imaging. Radiology 2003; 227:529-37

[5] Ouwerkerk R, et al. Elevated tissue sodium concentration in malignant breast lesions detected with non-invasive 23Na MRI. Breast Cancer Res Treat. 2007; 106(2):151–60

[6] Grodd W, Klose U. Sodium-MR-Imaging of the Brain - Initial Clinical-Results. Neuroradiology. 1988; 30(5):399–407

[7] Murphy E, Eisner DA. Regulation of intracellular and mitochondrial sodium in health and disease. Circ Res. 2009; 104(3):292-303

[8] Rose AM, Valdes R. Understanding the Sodium-Pump and Its Relevance to Disease. Clin Chem. 1994; 40(9):1674-85

[9] Skou JC, Esmann M. The Na-K-Atpase. J Bioenergetics Biomembranes 1992; 24(3):249-261

[10] Cameron IL, et al. Intracellular concentration of sodium and other elements as related to mitogenesis and oncogenesis in vivo. Cancer Res 1980; 40:1493–1500

[11] Rotin D, et al. Requirement of the Na+/H+ exchanger for tumor growth. Cancer Res 1989; 49:205-21

[12] Hayes C, et al. Assessing changes in tumour vascular function using dynamic contrast-enhanced magnetic resonance imaging. NMR iomed 2002; 15:154–163

[13] Hausmann D, et al. Apparent diffusion coefficient and sodium concentration measurements in human prostate tissue via hydrogen-1 and sodium-23 magnetic resonance imaging in a clinical setting at 3T. Invest Radiol. 2012; 47(12):677-82

[14] Farag A, et al. Unshielded asymmetric transmit-only and endorectal receive-only radiofrequency coil for (23) Na MRI of the prostate at 3 tesla. J Magn Reson Imaging. 2015; 42(2):436-45

[15] Bae KT, et al. Proton and sodium MR imaging of in vivo human prostate using dual-tuned body and endorectal coils at 7 T. Proc. Intl. Soc. Mag. Reson. Med. 2010 (18):2693

[16] Paschke NK, et al. Mult-Parametric 1H/23Na Clinical Protocol of the Prostate at 3T using a Double Resonance Coil. Proc. Intl. Soc. Mag. Reson. Med. 2017 (25):1016

[17] Tropp J, et al. An endorectal dual frequency 13C-1H receive only probe for operation at 3.0 tesla. Proc. Intl. Soc. Mag. Reson. Med. 2006 (14): 2594

[18] Christensen JD, et al. Quantitative tissue sodium concentration mapping of normal rat brain. Magn Reson Med 1996; 36:83–9
[19] Riemer F, et al. Sodium (23Na) ultra-short echo time imaging in the human brain using a 3D-Cones trajectory. Magn Reson Mater Physics, Biol Med 2014; 27:35–46
[20] Gurney PT, et al. Design and analysis of a practical 3D cones trajectory. Magn Reson Med 2006; 55:575-82
[21] Axel L, et al. Intensity Correction Surface-Coil MR Imaging. Am J Roentgenol 1987; 148:418-420
[22] Stobbe R, Beaulieu C. In vivo sodium magnetic resonance imaging of the human brain using soft inversion recovery fluid attenuation. Magn Reson Med. 2005; 54(5):1305–10
[23] Madelin G, et al. Sodium inversion recovery MRI of the knee joint in vivo at 7T. J Magn Reson. 2010; 207(1):42–52
[24] Kline RP, et al. Rapid in vivo monitoring of chemotherapeutic response using weighted sodium magnetic resonance imaging. Clin Cancer Res. 2000; 6(6):2146–56
[25] Conway EJ. Nature and significance of concentration relations of potassium and sodium ions in skeletal muscle. Physiol Rev. 1957; 37(1):84-132
[26] Madelin G, et al. A method for estimating intracellular sodium concentration and extracellular volume fraction in brain in vivo using sodium magnetic resonance imaging. Sci Rep. 2014; 4:4763
[27] Wang XZ, et al. Diffusion-weighted imaging of prostate cancer: correlation between apparent diffusion coefficient values and tumor proliferation. J Magn Reson Imaging 2009; 29:1360-6
[28] Epstein JL, et al. The 2005 international society of urological pathology (ISUP) consensus conference on Gleason grading of prostatic carcinoma. Am J Surg Path 2005; 29:1228-1242
[29] Lawrence EM, et al. Evaluating Prostate Cancer Using Fractional Tissue Composition of Radical Prostatectomy Specimens and Pre-Operative Diffusional Kurtosis Magnetic Resonance Imaging. PLoS One. 2016; 11(7):e0159652
[30] Grignon DJ, Sakr WA. Zonal origin of prostatic adenocarcinoma: are there biologic differences between transition zone and peripheral zone adenocarcinomas of the prostate gland? J Cell Biochem. 1994; 19(Suppl):267–269
[31] McNeal JE, et al. Zonal distribution of prostatic adenocarcinoma: correlation with histologic pattern and direction of spread. Am J Surg Pathol. 1988; 12:897–906
[32] Murphy E, Eisner DA. Regulation of intracellular and mitochondrial sodium in health and disease. Circ Res. 2009; 104(3):292–303
[33] Jacobs MA, et al. Monitoring of neoadjuvant chemotherapy using multiparametric, ^{23}Na sodium MR, and multimodality (PET/CT/MRI) imaging in locally advanced breast cancer. Breast Cancer Res Treat. 2011; 128(1):119-26
[34] Sharma R, Katz JK. Taxotere chemosensitivity evaluation in mice prostate tumor: validation and

diagnostic accuracy of quantitative measurement of tumor characteristics by MRI, PET, and histology of mice tumor. Technol Cancer Res Treat. 2008; 7(3):175-85
[35] Jacobs MA, et al. Proton, diffusion-weighted imaging, and sodium (23Na) MRI of uterine leiomyomata after MR-guided high-intensity focused ultrasound: A preliminary study. J Magn Reson Imaging 2009; 29:649–656

Chapter 5: The value of ^{11}C-acetate PET-CT in identifying prostate cancer and differentiating tumour from benign prostatic hypertrophy

5.1 Introduction

Positron emission tomography (PET) using the tracer ^{18}F-FDG has become part of routine clinical practice for staging and the assessment of treatment response in a number of cancers. However, the use of ^{18} F-FDG is limited in prostate cancer due to the reduced glycolytic activity of low to intermediate Gleason grade tumours and artefact related to tracer activity in the adjacent bladder [1]. ^{11}C-acetate PET-CT has shown promise in detection of prostate cancer, nodal disease and bone metastases [2, 3]. The rationale is the preferential utilisation of fatty acid metabolism for energy production in prostate cancer, with acetate being a naturally occurring fatty acid pre-cursor which is rapidly metabolized into acetyl-CoA, and employed to build membrane fatty acids [4]. An added advantage is the respiratory route of excretion of the tracer (via breakdown into $^{11}CO_2$), with minimal bladder activity. However, exhalation of the agent brings additional challenges, with possible radiation exposure to staff, the potential to release a radioactive gas into the atmosphere and increased background noise leading to degradation of the images acquired.

Recent work by Jambor et al [5, 6] and Mena et al [7] has shown promise for the use of ^{11}C-acetate for local detection of prostate cancer. However, despite increased uptake in prostate tumours compared to normal prostate, there was significant overlap with benign prostatic hypertrophy (BPH), resulting in no overall benefit compared to mp-MRI. The half-life of ^{11}C is 20.38 minutes, and as such, imaging is typically performed 10-20 minutes after tracer injection [8]. However, later time-point imaging is feasible and has been shown to

help distinguish hepatocellular carcinoma from focal nodular hyperplasia in the liver [9], and may be beneficial in allowing clearance of the tracer from the background blood pool.

Acetate is a fatty acid precursor that is converted to acetyl-CoA and oxidised in the tricarboxylic acid (TCA) cycle. Injected ^{11}C-acetate is rapidly converted into TCA cycle intermediates and CO_2, but can also be used for fatty acid synthesis resulting in accumulation of ^{11}C into lipids [10, 11]; thus later imaging may preferentially show acetate uptake in cancer with an increased tumour-to-background ratio. Recent work in prostate cancer using murine C42b xenografts is supportive of this, with optimal contrast occurring at the 60-90 minute time-point [12]. Patlak analysis of dynamic data suggests that during the early time period, the reversibly labelled tumour pool, representing tricyclic acid cycle metabolites and bicarbonate was dominant, whereas after 17.5min, the irreversibly labelled pool representing tumour lipid dominance. This would be supported by clinical data which suggests that 50% - 80% of injected acetate is metabolized to bicarbonate by the 10-15 minute time point [3, 13]. Uptake of acetate by tumour cells may also depend on the tumour microenvironment, with tumour cells having an increased excretion of acetate under hypoxic conditions [14], and uptake of acetate tracers shown to increase when oxygen levels are reduced [15, 16].

It was therefore hypothesised that late (up to 90 minutes) ^{11}C-acetate PET-CT imaging in patients is feasible, and it may be that at later time-points prostate cancer foci will demonstrate tracer uptake in tumour lipids to enable improved tumour-to-background detection and further differentiation of tumour from BPH may be aided due to the blood-pool clearance of tracer from hypervascular BPH nodules.

5.2 Methods

5.2.1 Patient population

9 patients with biopsy-proven intermediate or high risk prostate cancer were prospectively enrolled and underwent a dedicated research PET/CT prior to treatment with radical prostatectomy. Participants were recruited between September 2016 and May 2017, with written informed consent obtained in all cases. Approval for the study was granted by the institutional review board, the local ethics committee (CUH/15/EE/0213), and the Administration of Radioactive Substances Advisory Committee (ARSAC, certificate reference RPC/83/400/33606).

5.2.2 Soda lime trap

In order to minimise the radiation expired into the room, a system was devised for trapping exhaled CO_2 gas. A face mask was fitted and a closed tubing system employed with no valves and a continuous flow pump drawing exhaled air through a soda lime trap at ~ 20 L/min (**Figure 5.1**).

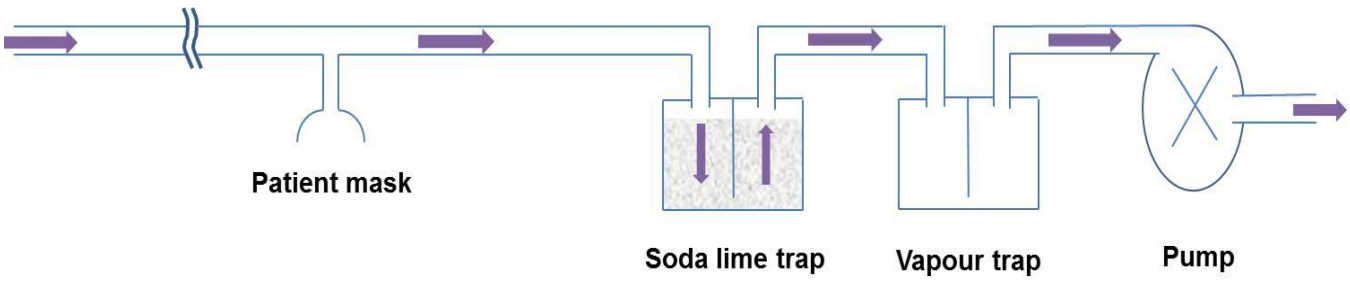

Figure 5.1 Schematic representation of the soda lime trap design.

A double medical grade disposable CO_2 absorber was employed (Spherasorb™; Intersurgical, Wokingham, UK), with each containing 500 g of soda lime, with a capacity of 120 L/kg. Average exhaled volume is predicted to be 6 L per minute, based on a respiratory rate of 12 breaths/minute and a tidal volume of approximately 0.5 L. Exhaled air contains approximately 4% CO_2, therefore during a 90 minute study, 21.6 L CO_2 will be expired; this requires 180g of soda lime absorbent (21.6L ÷ 120 L/kg capacity); **Figure 5.2**. There will also be a small contribution from CO_2 within room air (0.04%), based on the pump speed of 20 L/min over a 90 minute scan this will produce 0.72 L of CO_2 (0.04% of 1800 L) and require an extra 6 g of soda lime absorbent (total = 186 g).

Figure 5.2 Soda lime trap pre (left) and post (right) scanning.
The beads demonstrate a colour change from white to violet with CO2 absorption. Each canister contains 250g; the degree of colour change is expected given the predicted 186g required.

5.2.3 PET/CT Imaging

Subjects were scanned supine, with an oral-nasal face mask to collect respirated CO_2. PET/CT scans were performed on a GE Discovery 690 (GE Healthcare, Waukesha, WI, US) at Addenbrooke's Hospital, Cambridge, UK. Immediately following a low-dose CT of the abdomen and pelvis for attenuation correction and anatomical localisation, patients received an intravenous bolus injection of up to 1500 MBq ^{11}C-acetate [7]. Emission data were acquired in list-mode over 90 minutes in one bed position with the prostate centred axially in the FOV. List-mode data were binned in 54-time frames of increasing duration (12×5 s, 3×10 s, 6×15 s, 4×30 s, 5×60 s, 5×120 s, 10×150 s, 9×300 s) and reconstructed into a 192x192x47 matrix with 3.12×3.12×3.27 mm voxels, using time-of-flight ordered-subsets expectation maximisation (TOF-OSEM) with 4 iterations and 24 subsets. Corrections for attenuation, scatter, randoms, dead time, normalisation, sensitivity and isotope decay were applied, together with an isotropic 4-mm full-width at half maximum Gaussian filter post reconstruction. The attenuation correction CT acquisition parameters were: tube voltage 140kV, tube current 80mA, rotation time 0.5 seconds, pitch 1.375, slice thickness 3.75 mm reconstructed to 3.27 mm. Participants were not required to fast prior to their PET/CT examination. ^{11}C-acetate was provided by the Wolfson Brain Imaging Centre, Cambridge, UK.

The effective dose (ED) for ^{11}C-acetate has been estimated to be 0.0049 mSv/MBq [17], hence, for an administered activity of 1,500 MBq, the ED is 7.4 mSv. The ED for the low dose CT component of the examination was estimated at 0.7 mSv, giving a total estimated ED of 8.1 mSv for the protocol.

5.2.4 Magnetic Resonance Imaging

All participants underwent prostate MRI examinations as part of their clinical management, performed at 1.5-T or 3.0-T scanners using a surface coil and no endorectal coil. All studies met minimum PI-RADS version 1 sequence requirements [18] and included axial T1-weighted images of the pelvis, high resolution axial T2-weighted images of the prostate and DWI with a minimum of two b values, with a high b value of ≥800 - 1,000. To avoid bias in selection of ROIs with high uptake on PET, the T2-axial MR images were utilised for the definition of ROIs for use in the analysis of the PET data as described in the following section.

5.2.5 Image analysis

PET, CT and MR image registration: Image registration was performed blinded to the clinical data of the participants and utilised models implemented within the Advanced Normalization Tools registration software (ANTs; Penn Image Computing and Science Lab, University of Pennsylvania, USA). The attenuation correction CT component of the ^{11}C-acetate examination of each patient was used as the reference space for all registrations performed in this study.

To reduce the impact of patient motion during the ^{11}C-acetate PET acquisition, the 54 frames of the dynamic PET image series were non-rigidly registered to the time frame image corresponding to 55-60 min post tracer administration (frame 48). Registration was performed using a 4-level multi-scale approach with affine initialisation and utilising normalised cross-correlation as the similarity metric. Adjustment for local non-rigid deformations was performed using symmetric normalisation (SyN) with Gaussian

regularisation (3 voxels) of the update velocity fields and zero total field regularisation. The registered PET frames were averaged for the generation of a mean image, which was subsequently co-registered with the attenuation correction CT using affine transformation and a mutual information-based similarity.

Registration of T2 MR images and PET data was performed using the attenuation correction CT as the intermediate link for spatially registering the datasets. To avoid the registration process being influenced by pelvic bone anatomy and structures distant to the prostate, sub-volume encompassing the prostate gland alone were utilised. The quality of the results obtained by the registration process was visually inspected. The resulting transformation was subsequently applied to all 54 frames in the PET dynamic series. A schematic diagram of the registration process is presented in **Figure 5.3 and 5.4.**

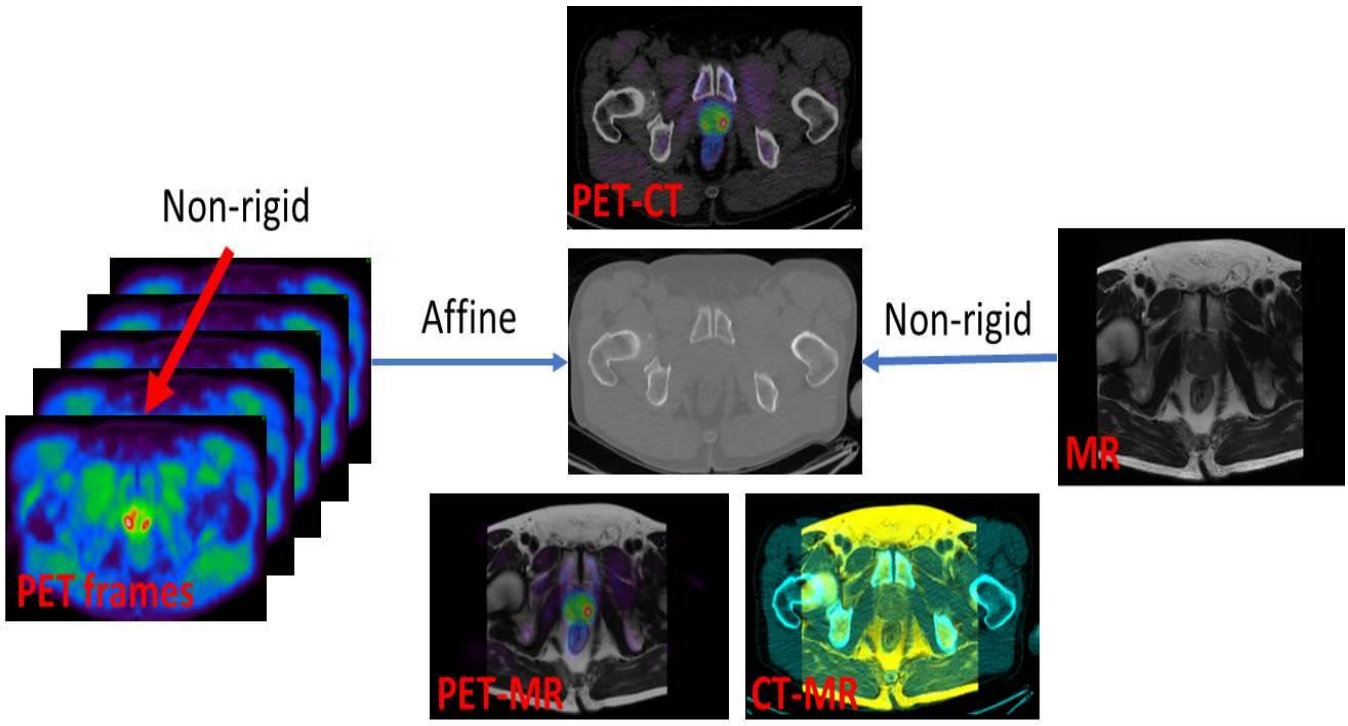

Figure 5.3: Schematic diagram of the image registration paradigm employed.

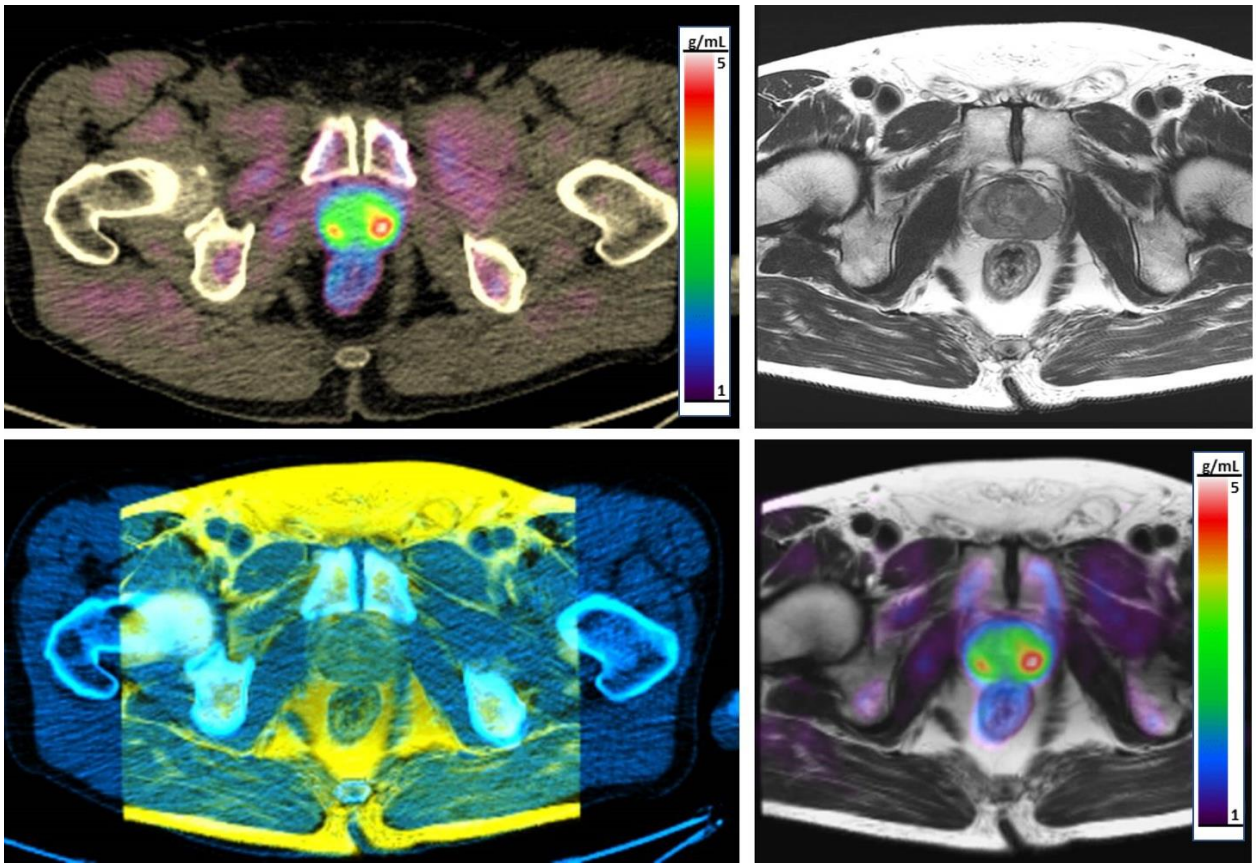

Figure 5.4. Fusion of PET/CT to MRI. PET/CT (top left) and T2-weighted axial MR images (top right) are fused via registration software using bony landmarks (bottom left), to create a fused PET/MRI image (bottom right) for assessment of pre-defined tumour and normal tissue ROIs from the diagnostic MRI sequences.

Lesion-based analysis: Registered frames of the dynamic PET image series corresponding to 6-10 min, 14-20 min, 20-30 min and 60-90 min post injection (p.i) were averaged, and utilised for the generation of standardised uptake value (SUV) images normalised by body weight. Tumour ROIs were delineated on the clinical diagnostic MRI by a radiologist with 7-years' experience reporting clinical prostate MRI; tumour ROI delineation included lesions in the peripheral (tPZ) and transition zones (tTZ). ROIs for normal prostate tissue in the peripheral zone (nPZ) and benign hyperplasia (BPH) were also delineated. ROI maps were transformed into the space of the attenuation correction CT and overlaid on the co-registered PET SUV maps for the calculation of SUV_{mean}, SUV_{max} and $SUV_{60\%}$ (voxel values above a 60% iso-contour of SUV_{max}) in these areas. Target-to-background ratios (TBR) for

both tumour and BPH regions were determined by normalising SUV_{max} in these regions by SUV_{mean} in normal PZ (tumour/nPZ and BPH/nPZ, respectively). Tissue time activity curves over the 90-min PET acquisition were derived by applying the ROIs onto the registered PET dynamic series.

5.2.6 Histopathological correlation

Prostatectomy specimens were fixed in formalin and oriented by the location of the seminal vesicles, posterior surface of the prostate, and by the position of the urethra. The apical cone was amputated, and sliced into 4 mm sections from left to right, the remaining gland was cut transversely into 5 mm whole-mount parallel slices in the horizontal plane from inferior to superior. Tumour was outlined on hematoxylin and eosin (H&E) stained sections from each slice by an experienced uropathologist specializing in prostate cancer. Each histopathology slice was manually co-registered to the corresponding PET/CT slice, with utilization of the diagnostic MR images where necessary.

5.2.7 Statistical analysis

Statistical analysis was conducted in Matlab 2016b (The Mathworks, Nattick, MA). Data are presented as n (%), mean (± standard deviation) or median [first quartile (Q1)-third quartile (Q3)] as appropriate. Linear mixed effects analysis was performed to assess the relationship between static PET parameters (SUV or TBR) and region type (nPZ, BPH or tumour). Region type and age were entered the model as fixed effects, while random effects included intercepts for subjects and regions, as well as by-region random slopes for the effect of static PET parameters. Visual inspection of residual plots did not reveal obvious deviations from homoscedasticity or normality. P-values were obtained by likelihood ratio tests of the

full model with the effect in question against the model without the effect in question; p-values < 0.05 were considered statistically significant.

5.3 Results

9 patients were included in the study group, with a median age of 66 years (mean 64.2, range 59 - 69 years) and a median pre-biopsy PSA level of 7.32 ng/mL (mean 8.16, interquartile range 5.03 – 9.76 ng/mL); **Table 5.1**. The median time from biopsy to PET/CT was 57 days (mean 70, range 40 - 189 days), and median time from MRI to PET/CT was 76 days (mean 87.3, range 45 - 177 days). The median time from PET scanning to surgery was 1 day (mean 5.78, range 0 - 20 days). 8 studies acquired data to 90 minutes, one study was stopped after 60 minutes due to patient intolerance. A total of 13 prostatic tumours were present; of these, nine lesions (69%) were in the peripheral zone and four (31%) in the transition zone. Four patients (44%) presented with multifocal disease: three patients (30%) had tumour foci in both the transition and peripheral zone, while one patient (11%) presented with bilateral peripheral zone lesions. Benign prostate hyperplastic (BPH) regions could be identified in all participants (100%).

Characteristic	Value
Median patient age, years (IQR)	66 (60 – 67)
Median PSA level, ng/mL (IQR)	7.32 (5.03 – 9.76)
Gleason score (n = 13)	
3+3	2
3+4	10
4+3	1
4+4	0
≥9	0
Pathologic tumour stage (n = 9)	
T2a	0
T2b	0
T2c	4
T3a	4
T3b	1

Table 5.1. Patient Characteristics. 13 tumours in 9 patients.

Patients were injected with a median activity of 1192 MBq ^{11}C-acetate (range 912 - 1482 MBq). The maximum activity released to the atmosphere was 4.6 MBq (mean 2.0 MBq); **Figure 5.5**. The fractional accumulation of the injected ^{11}C was 28.0%, derived as estimate activity in soda-lime trap at end of session (range 7.7 – 55%). The mean estimated release of activity into the room if there had been no trapping was 50.8 MBq (range 18.5 – 133.4 MBq); **Table 5.2**.

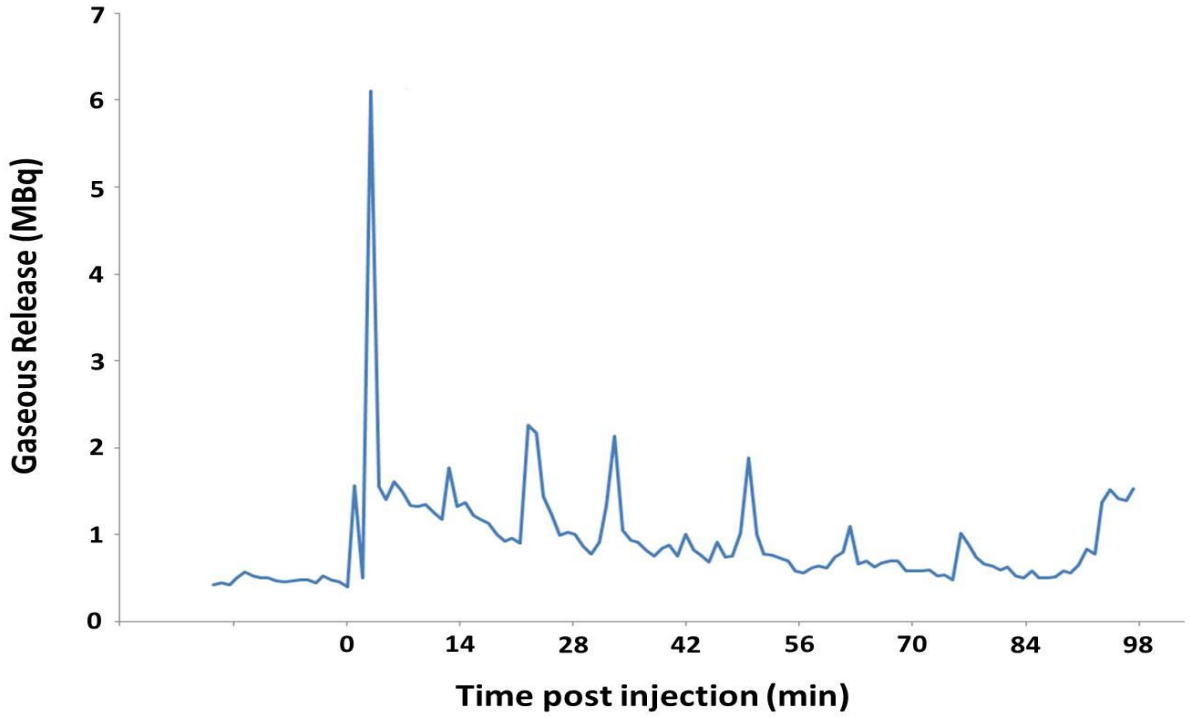

Figure 5.5. Example stack monitor of gaseous released activity. Patient 9: 59 year old man, injected activity 1349 MBq, total gaseous release 2.57 MBq.

#	Age	Administered activity (MBq)	Total gaseous release (MBq)	Fractional accumulation in trap	Total decay corrected release (MBq)	Estimated release if no trapping (MBq)
1	66	912	0.85	47.5%	11.3	33.4
2	62	1294.1	N/A*	24.2%	N/A*	N/A*
3	69	1041.5	4.61	7.7%	24	20.0
4	67	1481.8	N/A*	21.9%	N/A*	N/A*
5	59	1090	1.76	20.1%	14.76	27.9
6	60	1206.6	0.56	30.0%	2.86	71.4
7	67	1000.2	2.63	N/A†	13.78	N/A†
8	69	1304.7	1.33	17.8%	17.94	18.5
9	59	1349	2.57	55.0%	14.58	133.4

Table 5.2. Activity administered and released. * = could not be calculated as extractor not working during these studies; † = activity in the trap not estimated.

Time activity curves from the patient cohort corresponding to regions for the normal prostate, BPH and tumour regions in the peripheral and transition zones are illustrated in **Figure 5.6**. Box plots of SUV_{max}, and $SUV_{60\%,}$ for normal PZ, BPH and tumour tissue for all time intervals are presented in **Figure 5.7**.

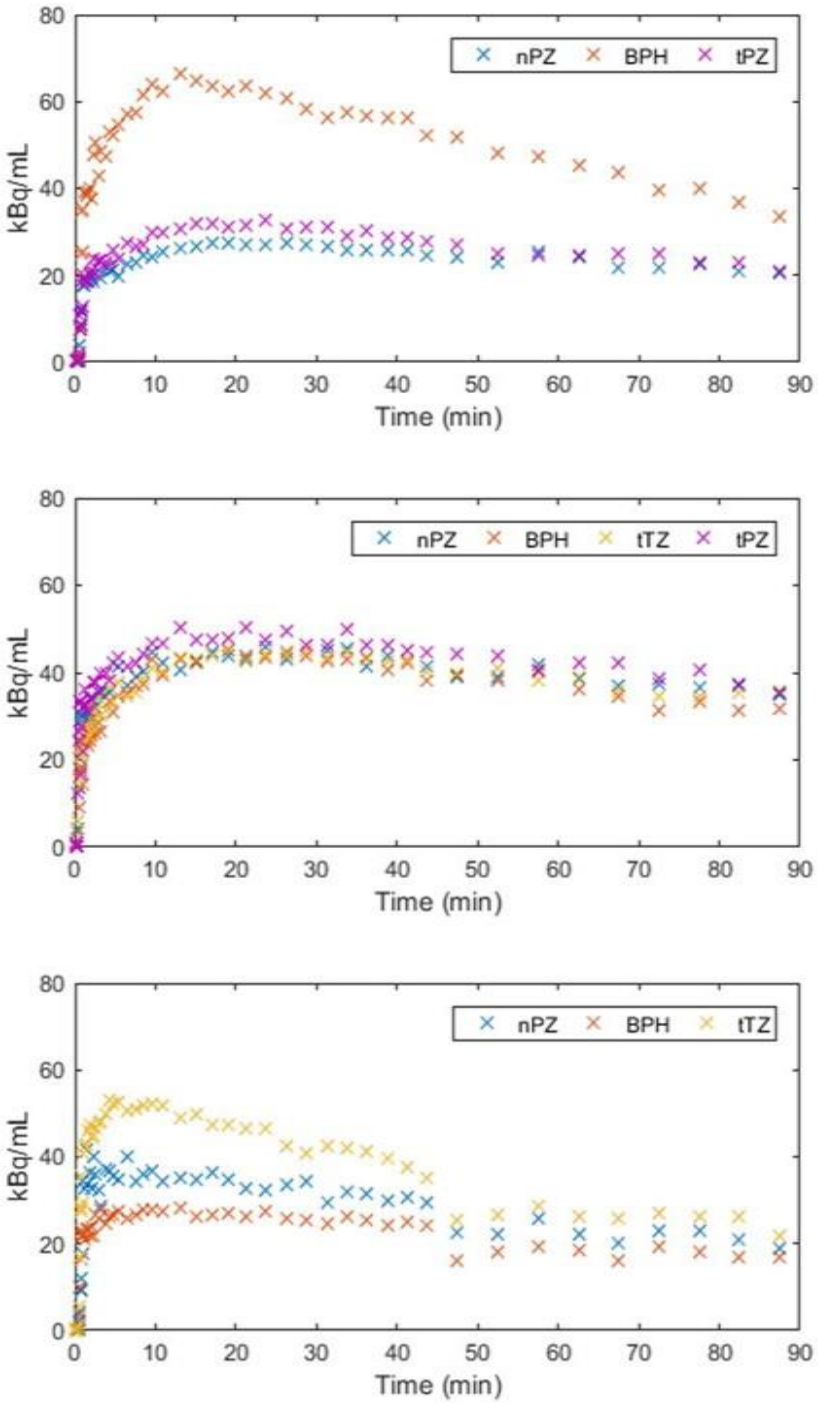

Figure 5.6a. Time activity curves for patients 1-3. Activity derived from ROIs placed on tumour and benign tissue. nPZ = normal peripheral zone (PZ), BPH = benign prostatic hypertrophy, tPZ = PZ tumour, tTZ = transition zone tumour.

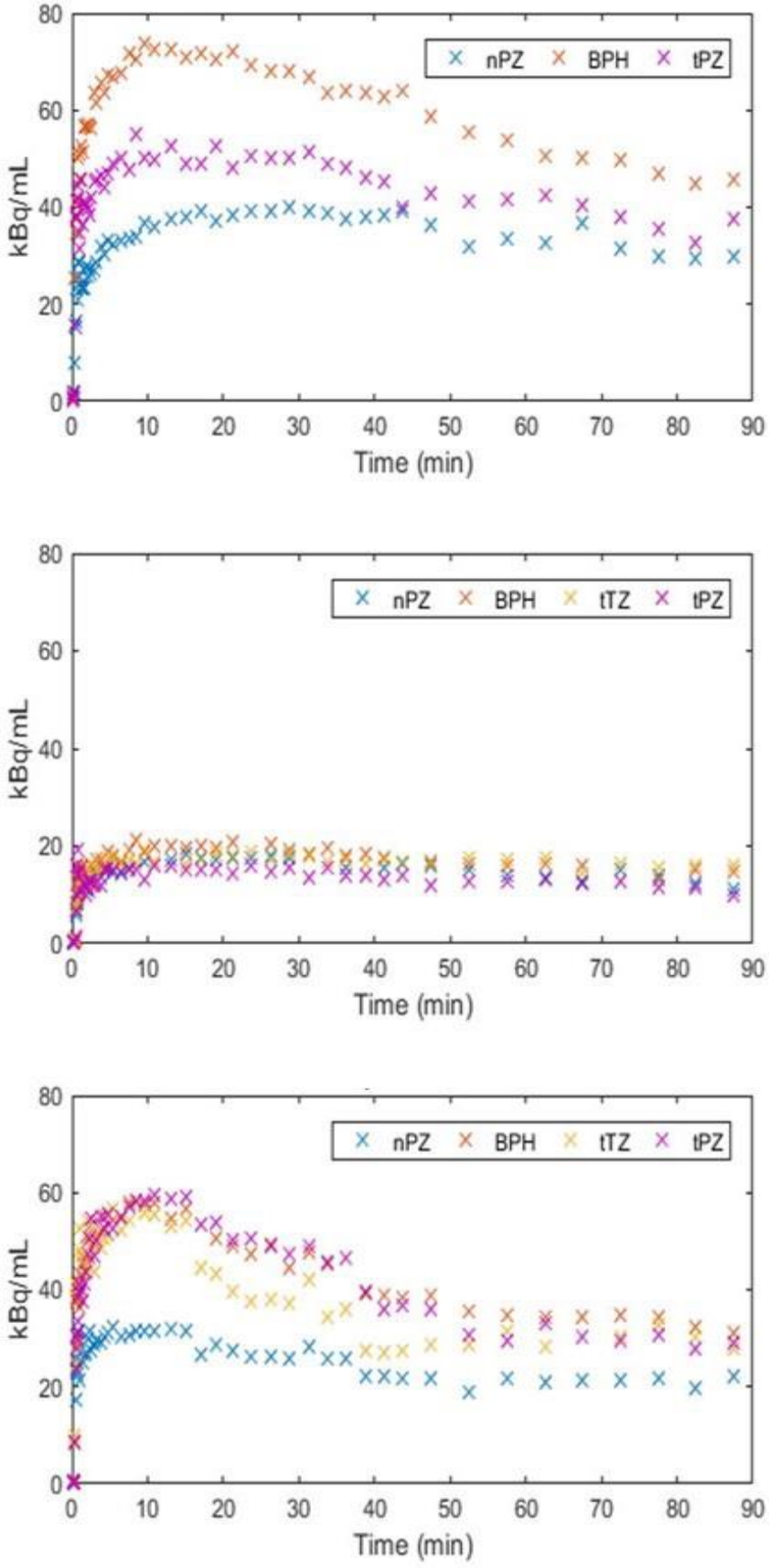

Figure 5.6b. Time activity curves for patients 4-6. Activity derived from ROIs placed on tumour and benign tissue. nPZ = normal peripheral zone (PZ), BPH = benign prostatic hypertrophy, tPZ = PZ tumour, tTZ = transition zone tumour.

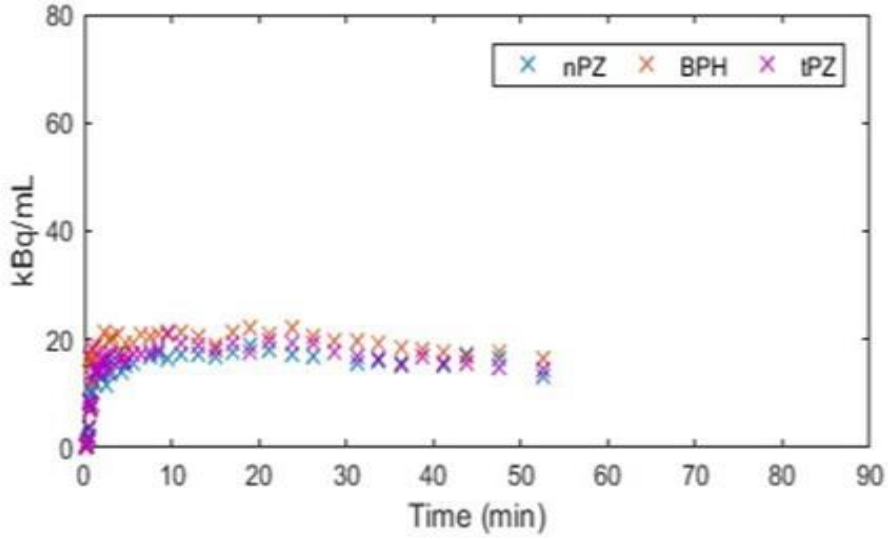

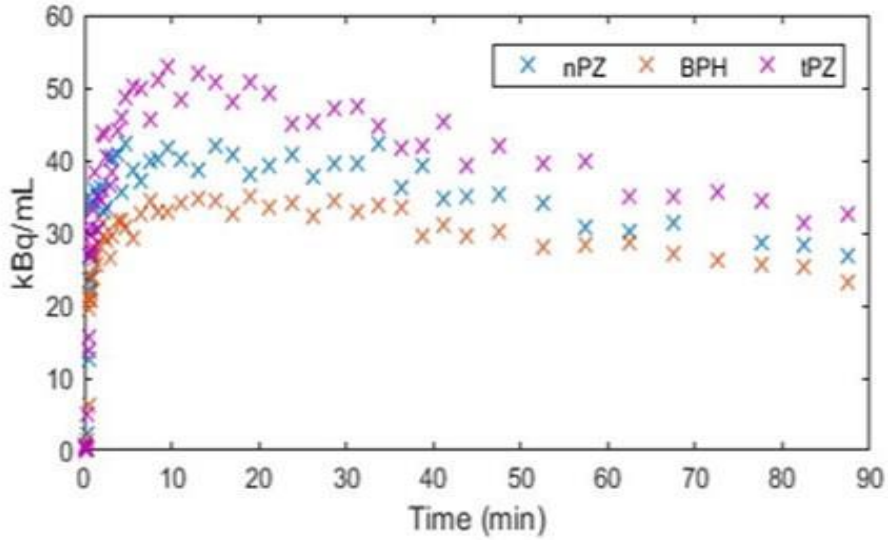

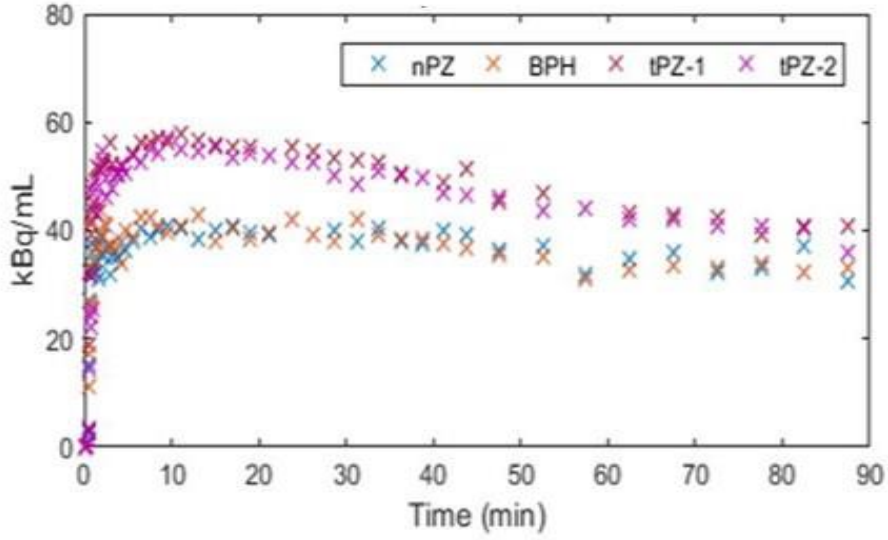

Figure 5.6c. Time activity curves for patients 7-9. Activity derived from ROIs placed on tumour and benign tissue. nPZ = normal peripheral zone (PZ), BPH = benign prostatic hypertrophy, tPZ = PZ tumour, tTZ = transition zone tumour.

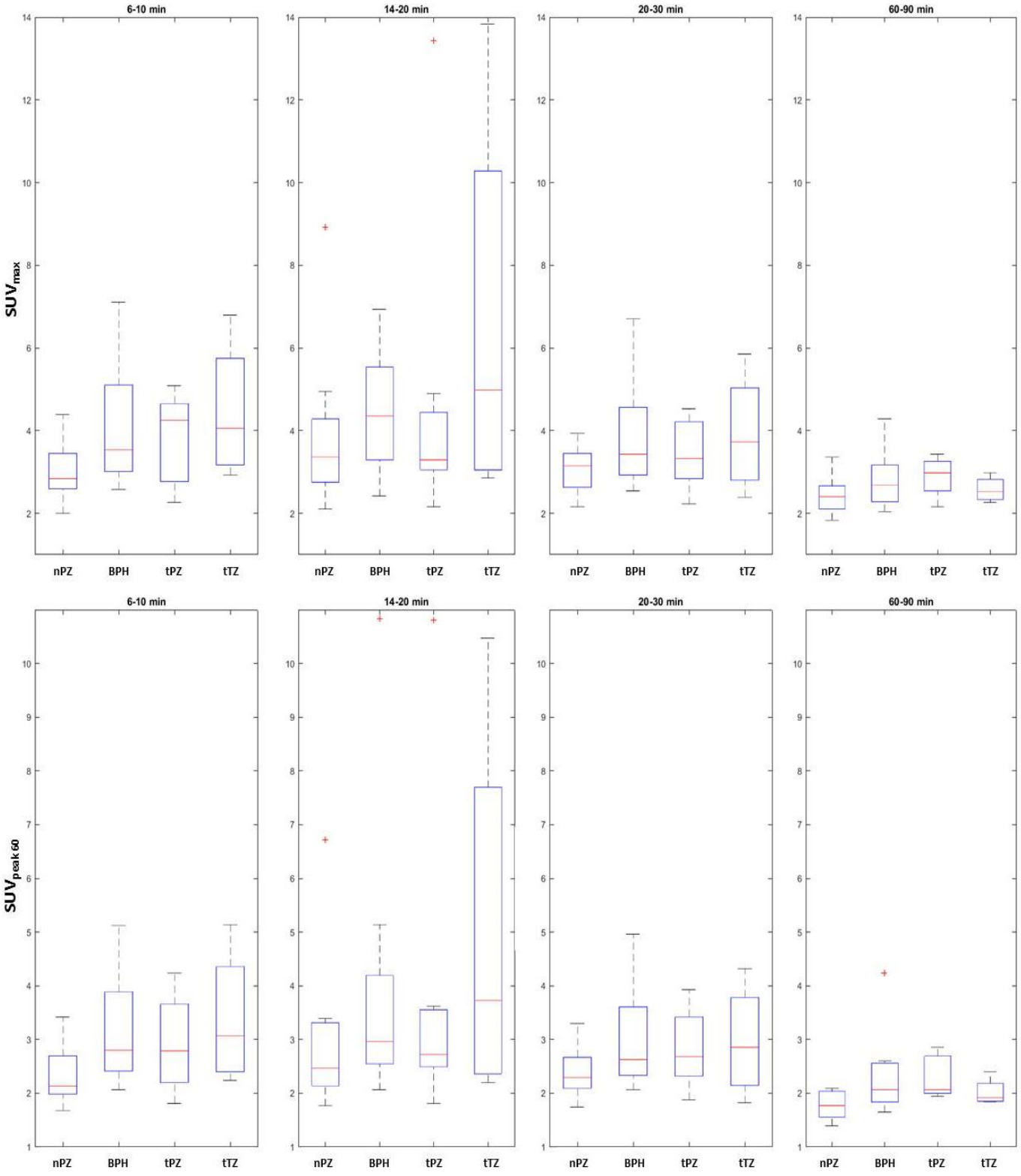

Figure 5.7. Box and whisker plots for distinguishing tumour from benign tissue. SUV_{max} (top row) and $SUV_{peak-60}$ (bottom row) derived from ROIs placed on tumour and benign tissue. nPZ = normal peripheral zone (PZ), BPH = benign prostatic hypertrophy, tPZ = PZ tumour, tTZ = transition zone tumour. Top and bottom of boxes represent 25th and 75th percentiles of data, line in boxes represents the median value and bars representing data within 1.5 times interquartile range, "+" denotes outliers.

^{11}C-acetate uptake was visualised in the prostate gland in all patients and for all time intervals post injection (p.i.); **Figure 5.8**. Linear mixed effects analysis indicated a statistically significant increase in BPH SUV_{max} and $SUV_{60\%}$ values relative to the normal prostate for all time intervals considered (SUV_{max} p = 0.025, 0.023, 0.039, 0.038; $SUV_{60\%}$: p = 0.019, 0.017, 0.033, 0.018 for 6-10, 14-20, 20-30 and 60-90 minutes p.i. respectively), with increase borderline significant on the basis of SUV_{mean} (p=0.052, 0.045, 0.076, 0.063, respectively). No age-dependent effects were observed in uptake values of the normal prostate (p=0.44); **Figure 5.9**.

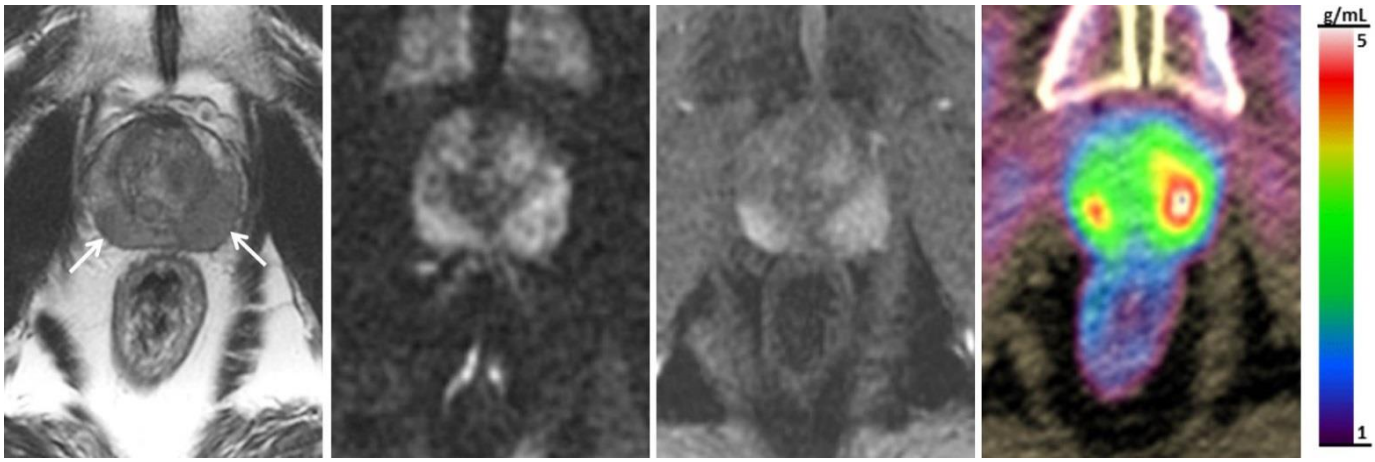

Figure 5.8a. Diagnostic MR imaging and ^{11}C-acetate PET/CT. 59 year old patient, PSA 4.88 ng/ml. Diagnostic MRI shows focal low T2 signal bilaterally (left) at the mid gland PZ, larger on the left side (arrows), with high signal on b-1400 DWI (centre, left) and early enhancement on DCE (centre, right). ^{11}C-acetate PET/CT image at the 14-20 minute time point shows increased tracer uptake within both lesions. Prostatectomy shows bilateral lesions of grade Gleason 3+4, with established extracapsular extension on the left (T3a disease).

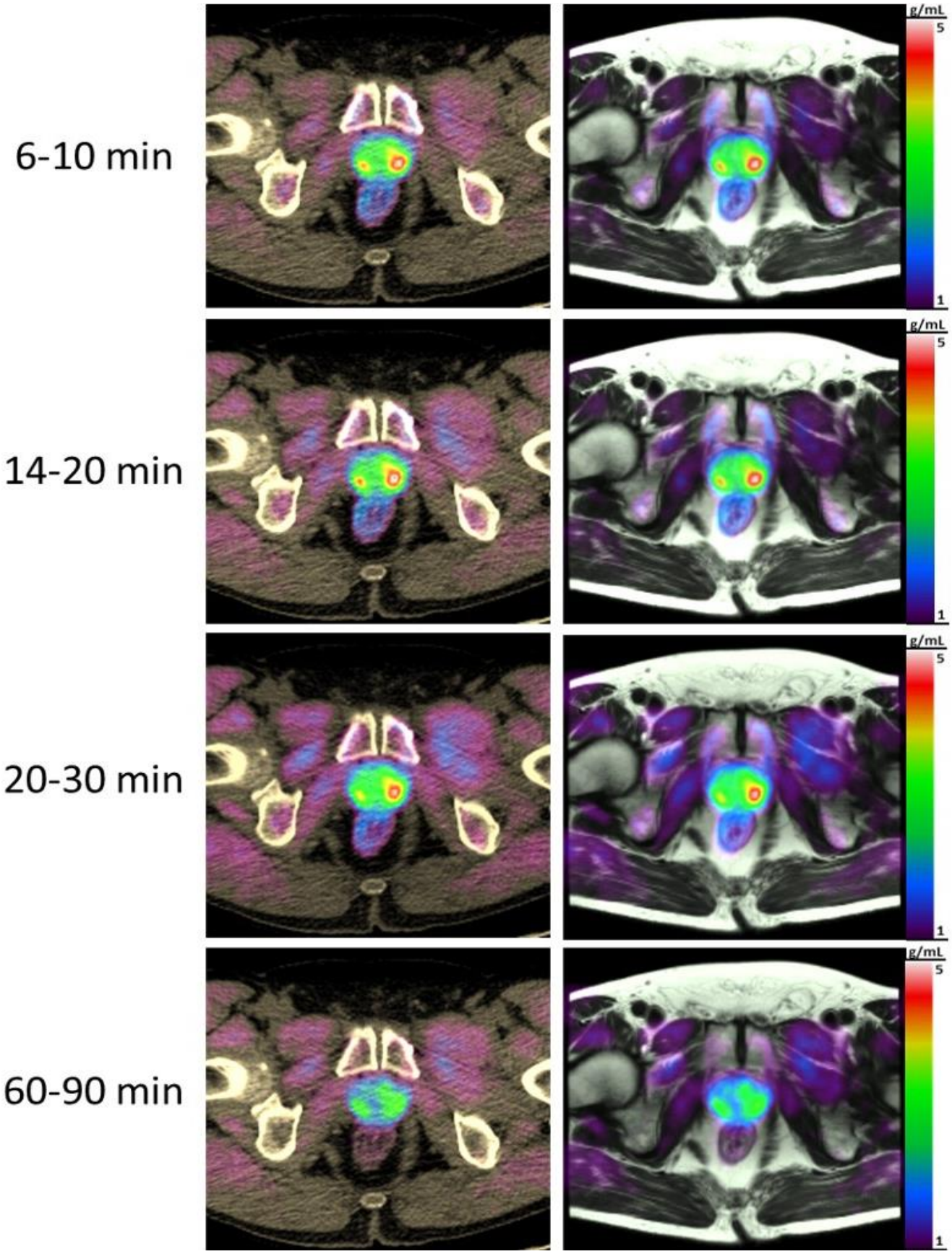

Figure 5.8b. Fusion of PET/CT to MRI. 59 year old patient, PSA 4.88 ng/ml, bilateral Gleason 3+4 tumours in the mid gland PZ. ^{11}C-acetate PET/CT image (left column) and fused ^{11}C-acetate PET-MRI images (right column) acquired at different time points post tracer injection, showing increased uptake within the lesions at the first 3 time-points.

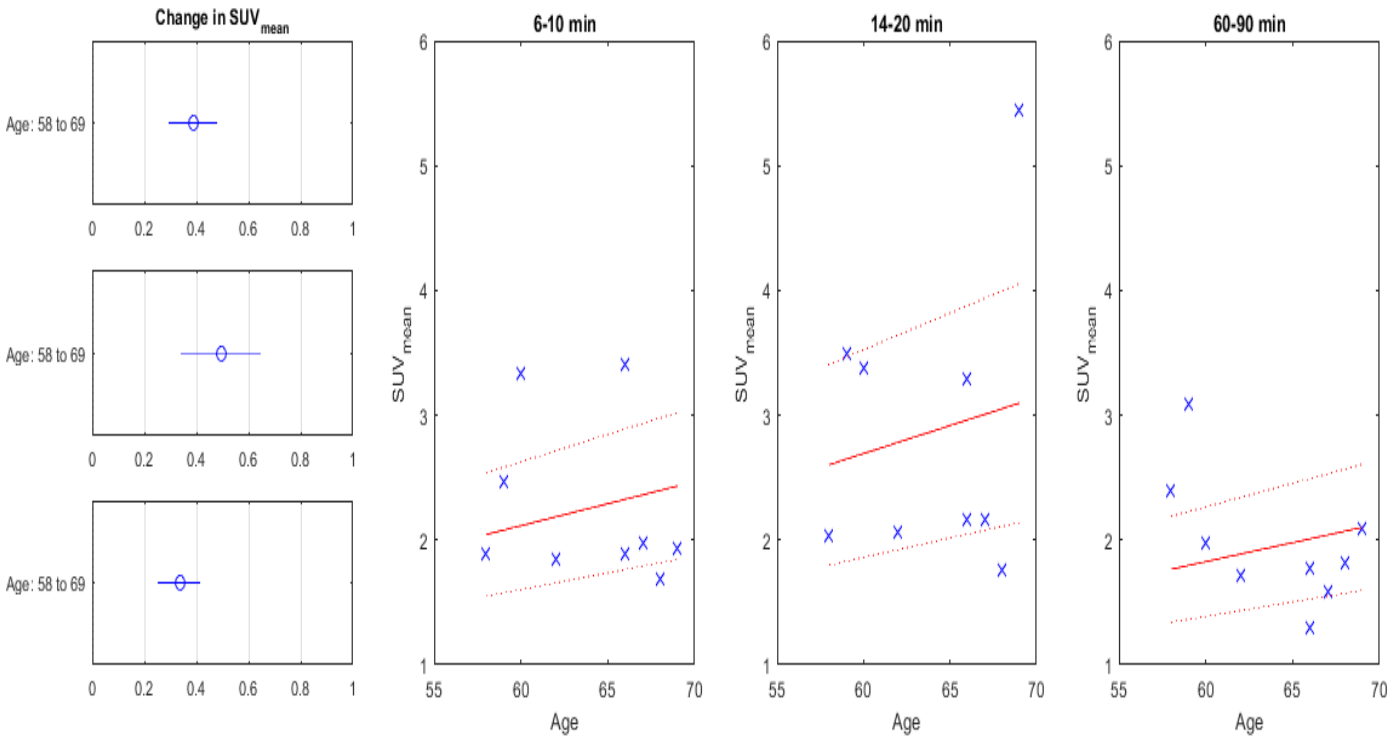

Figure 5.9. Correlation of patient age to SUV_{mean} uptake in the normal PZ.

An increase in values for all SUV metrics was also observed in PCa with respect to normal PZ regions. This was significant for all SUV metrics in the 6-10 min interval p.i. (SUV_{max}: p = 0.024; SUV_{mean}: p = 0.015; $SUV_{60\%}$: p = 0.018). No statistically significant increases in either SUV_{max} or SUV_{mean} relative to normal PZ were observed for the 14-20 min and 20-30 min time intervals. However, $SUV_{60\%}$ indicating a stronger effect at all time intervals p.i., reaching significance in all but the 20-30 minute time-point (6-10 min: p = 0.018; 14-20 min: p = 0.028; 20-30 min: p = 0.052; 60-90 min: p = 0.044). **Table 5.3** shows all values acquired during the late (60-90 minute) time point.

			Normal PZ			BPH			Tumour		
Patient	**Location**	**Gleason**	**SUV_{max}**	**SUV_{mean}**	**SUV_{p60}**	**SUV_{max}**	**SUV_{mean}**	**SUV_{p60}**	**SUV_{max}**	**SUV_{mean}**	**SUV_{p60}**
1	PZ	3+4	3.353	1.767	2.097	4.288	3.204	4.236	3.291	1.894	2.086
2	PZ	3+4	1.880	1.710	1.710	3.039	2.595	2.597	2.386	2.041	2.041
4	TZ	3+3	2.339	1.820	1.833	2.054	1.628	1.651	2.419	1.762	1.860
4 (lesion 2)	PZ	3+4	-	-	-	-	-	-	2.153	1.944	1.944
5	TZ	3+4	2.363	1.621	1.680	2.509	1.995	2.016	2.647	1.636	1.967
5 (lesion 2)	PZ	3+4	-	-	-	-	-	-	2.692	1.842	1.980
6	PZ	3+4	2.779	2.400	1.440	3.310	2.186	2.531	3.226	2.852	2.852
7	TZ	4+3	2.436	1.979	1.979	2.044	1.635	1.657	2.986	2.376	2.395
8	TZ	3+4	1.836	1.303	1.397	2.826	2.084	2.084	2.261	1.842	1.844
8 (lesion 2)	PZ	3+3	-	-	-	-	-	-	2.731	1.882	2.018
9	PZ	3+4	2.543	2.089	2.089	2.521	2.040	2.045	3.431	2.588	2.660
9 (lesion 2)	PZ	3+4	-	-	-	-	-	-	3.223	2.708	2.720
Group mean	**-**	**-**	**2.441**	**1.836**	**1.778**	**2.824**	**2.171**	**2.352**	**2.787**	**2.114**	**2.197**

Table 5.3. SUV max, mean and peak-60 results per lesion at the 60-90 minute time point. Mean values listed; patient 3 did not complete imaging beyond the 60 minute time-point.

Classification of lesions into tumours occurring in either the peripheral or transition zone revealed statistically significant differences between tumour-PZ and normal-PZ SUV for the 60-90 min time interval (SUV_{max}: $p = 0.030$; SUV_{mean}: $p = 0.047$; $SUV_{60\%}$: $p = 0.041$), and SUV_{max} for the 14-20 min period ($p = 0.034$). Differentiation of tumour-TZ from normal-PZ was not achievable on the basis of SUV at the 20-30 and 60-90-time intervals, with statistically significant increases occurring at earlier time points ($SUV_{60\%}$: $p = 0.018$, 0.026 for the 6-10 and 14-20 min time periods respectively).

Target-to-background ratios (TBR) using SUV_{max} for both BPH and tumour were compared, with normal PZ as the background denominator. For TBR, the max SUV value in the target regions (BPH and tumour) is normalised to the mean SUV normal prostate for that time interval.

TBR-BPH and TBR-tumour demonstrated high uptake values at all time intervals, and were not found to be significantly different from each other (range: $p = 0.34 - 0.83$). There was no significant difference demonstrated between time points for either TBR-BPH ($p = 0.85$) or TBR-tumour ($p = 0.63$). Discrimination between tumours in the PZ and TZ was also not feasible on the basis of TBR-PZ tumour compared to TBR-TZ tumour ($p = 0.40$, 0.10, 0.87, 0.37 for 6-10, 14-20, 20-30 and 60-90 min p.i. respectively).

5.4 Discussion

^{11}C-acetate has shown promise as a useful adjunct to current imaging methods for assessment of metastatic prostate cancer and recurrent disease [2, 5-8, 21, 22]. However, previous studies have shown limited ability of the tracer to distinguish primary tumours within the gland from BPH at the 10-20 minute time-point post injection. We tested the feasibility of imaging at later time-points to see if clearance of tracer from the blood pool and reversible uptake of tracer within prostate tumours could aid primary cancer detection.

An average of 28% of the initial injected activity was trapped within the soda lime canisters as exhaled (^{11}C)-CO_2, suggesting the majority of the expired activity was absorbed, with a mean of only 2.0 MBq gaseous release, representing 1.3% of the initial injected activity. Previous work suggests that this trapped percentage is expected: in canine models 23% of the injected ^{11}C-Acetate tracer will be exhaled as $^{11}CO_2$ in first 60 minutes, with the rest retained in the body [19], similar results have been noted in man, with the fractional recovery of ^{13}C-labelled CO_2 after ^{13}C-acetate infusion being 26.1 % [20]. The local Environment Agency permit allows for a daily PET/CT gaseous waste limit of 50 MBq and an annual limit of 500 MBq. These limits would be breached without use of the soda lime system, with an estimated mean release of activity without trapping being 50.8 MBq.

Differentiation between normal prostate and tumour could be achieved at both early (6-10 min) and late (60-90 min) time points post tracer administration on the basis of SUV_{max} and $SUV_{60\%}$, but not SUV_{mean}. The SUV_{mean} result may be explained by partial volume effects of normal tissue inaccuracies in co-registration of the ROIs from MRI, or tumours having a larger anatomical volume compared to their metabolic volume. However, our results did not

permit differentiation between BPH and prostate cancer at any time interval post injection.

Analysis of the time-activity-curves demonstrated rapid uptake in all regions, peaking approximately 3-10 min post tracer post injection. Regions of BPH tended to exhibit slowly decreasing patterns after approximately 10 minutes, whereas both tumours and normal prostatic tissue demonstrated a relative plateau phase after the initial peak, followed by a gradual decline in radioactivity concentration values at approximately 40 minutes. These findings are likely explained by the combined effects of perfusion, acetate metabolism and tracer efflux from prostatic tissue. It should be noted that the uptake mechanism of acetate in prostate tumours is yet to be fully elucidated. A plateau phase in tumours early after injection could be explained by sustained tracer delivery, however, this would not be exclusive to any tissue type. Acetate can be utilised by fatty acid synthase (FAS) as well as cholesterol synthesis, and predominance of one over the other may vary depending on the profile of each individual tumour. It is possible that in tumours with slow glycolytic activity, energy requirements are met by increased TCA metabolism due to fatty acid breakdown, whereas in others acetate uptake could represent fatty acid or cholesterol synthesis, or perhaps a combination of these, depending on the metabolic state of each individual tumour. FAS will exist in both normal tissue and BPH, although it will be expected to be significantly upregulated in cancer. This could perhaps explain the reversibility of time-activity-curves at late time points shown both here and in the Mena et al study [7], given that TCA and metabolites represent the reversible tissue pool (efflux to the circulation), but does not fully exclude the presence of an irreversible compartment in some tumours, relating to FAS.

^{11}C-acetate PET has been previously investigated for the ability to differentiate tumour from benign prostatic tissue. An early study by Oyama et al looked at 22 patients with biopsy proven prostate cancer showing a range of SUV_{max} ranged from 3.27 - 9.87 at 10 – 20 minutes in tumours; the majority of patients only had TRUS biopsy as the reference standard and they did not report benign tissue [8]. Jambor et al did not look at benign tissue, but showed no difference in tumour uptake compared to grade in 21 patients, with tumours of Gleason grade ≥3+4 having an average SUV_{max} and $SUV_{60\%}$ of 5.5 ±1.1 and 3.9 ±0.9, respectively [5]. Subsequent studies have shown results consistent to our study, with variable ability of ^{11}C-acetate to distinguish tumour from normal PZ, but not from BPH. A possible explanation for this finding may be an overlap in fatty acid synthase expression between tumours, BPH and normal tissue [4]. Mena et al, in a study of 38 patients showed than tumour SUV_{max} at 10-12 minutes (4.4 ±2.05) was significantly higher than normal prostate (2.1 ±0.94), but similar to BPH (4.8 ±2.01) [7]. A recent study by Polanec et al reported on 40 patients diagnosed with prostate cancer by differing reference tests and 16 without, showed that ^{11}C-acetate outperformed ^{18}FDG-PET, but with there being no significant difference between the SUV_{max} of tumours (4.6), BPH (5.0) or inflammatory prostatitis (4.6) at the 16-20 minute time-point [21]. Earlier work by Kato et al found SUV_{mean} at 16-20 minutes in 6 patients with prostate tumours (1.9 ±0.6) to be similar when compared to both BPH (2.1 ±0.6) and normal prostatic tissue (2.3 ±0.7) in separate patients and volunteers without prostate cancer, with a trend for reduced uptake values in normal prostate with age [22]. Similarly, we found SUV_{mean} to be poor at differentiating both BPH and prostate tumours from normal tissue. Inherent inaccuracies in ROI definition and image registration resulting in partial voluming of normal prostate tissue into BPH and tumour ROIs, may help to explain the low discriminative ability of SUV_{mean}. Our results did not

indicate a significant effect of age on the SUV of normal prostatic tissue; although the current patient cohort is small to draw significant conclusions, the age range reported here (58-69 years) is more typical of prostate cancer patient cohorts than the Kato study which additionally included normal volunteers of less than 50 years. In terms of tumour pathology the two papers using prostatectomy as gold standard [7, 21] had similar distributions to our cohort with predominantly Gleason 3+4 tumours, whereas, as expected, the two studies that used biopsy as standard and reported on grade had a much higher proportion of low grade Gleason 3+3 tumours [6, 8].

5.4.1 Limitations

Limitations of this study include the small sample size of the patient cohort, and the number of lesions investigated. A further limitation relates to potential translational inaccuracies in the region placement due to registration inaccuracies between PET, CT and MR images and the possibility of secondary partial voluming effects on the defined ROIs. The clinical MR images (in correlation to prostatectomy pathology) were chosen due to their improved spatial and contrast resolution and in order to minimise the risk of ROI selection bias for regions of increased uptake on PET/CT images. An important challenge in the registration process relates to the movement of the prostate, which can occur relative to the pelvic bones and neighbouring organs in the pelvis between sequential PET/CT and MRI sessions. This may result in an inaccurate alignment of the prostate in MR, CT and subsequently PET images, if the registration process is based on an alignment of the pelvic bones alone. Furthermore, variable rectal and bladder conditions between the two imaging sessions can induce local deformation of the prostate thereby further complicating the image registration process. We attempted to mitigate these effects by performing local non-rigid

registration of the prostate via the use of a bounding box. Future studies employing PET/MRI would serve to overcome this limitation.

5.4.2 Conclusions

The results from our study show that late time-point (60-90 minutes post injection) imaging is feasible using the tracer ^{11}C-acetate and can differentiate tumour tissue from normal peripheral zone. However, late imaging could not differentiate tumour tissue from BPH, in line with previous studies imaging at early time-points.

5.4.3 Clinical implications

An advantage of PET imaging is the ability of whole-body functional imaging to provide information on node and bone involvement for staging purposes. Any additional ability to identify and/or characterise the primary lesion would also be clearly advantageous.

Recently the PET tracer Gallium (^{68}Ga) labelled Prostate-specific membrane antigen (PSMA) has been developed. PSMA is a transmembrane protein that is known to be over-expressed on most prostate cancer cells. ^{68}Ga-PSMA has shown promise for detection of advanced and recurrent prostate cancer and an ability to detect micro-metastatic disease, occult to conventional standard of care CT and bone scintigraphy [23, 24]. Recent data suggests that ^{68}Ga-PSMA-PET may also improve diagnostic yield and localization of primary tumours within the gland. On sextant-based analyses, ^{68}Ga-PSMA has been shown to have a sensitivity of 67% and specificity of 92% [25] and a similar sensitivity (76%) compared to mpMRI (78%), but with a superior specificity (97% versus 79%) [26].

The results of our study suggest ^{11}C-acetate PET is unlikely to confer any advantage over ^{68}Ga-PSMA for primary disease, and further suffers from the disadvantage of needing an on-site cyclotron for tracer production. However, other potential clinical scenarios may provide a niche role. Fatty acid synthase inhibitors have recently been investigated for treatment of a number of tumour types, including prostate cancer [27], herein, ^{11}C-acetate may have serve as a treatment response biomarker for these novel agents, given the mechanism of acetate uptake and metabolism, however, this role would require further investigation.

5.5 References

[1] Hofer C, et al. Fluorine- 18-fluorodeoxyglucose positron emission tomography is useless for the detection of local recurrence after radical prostatectomy. Eur Urol. 1999; 36:31–35

[2] Haseebuddin M, et al. 11C-acetate PET/CT before radical prostatectomy: nodal staging and treatment failure prediction. J Nucl Med. 2013; 54(5):699-706

[3] Schiepers C, et al. 1-^{11}C-acetate kinetics of prostate cancer. J Nucl Med. 2008; 49(2):206-15

[4] Liu Y. Fatty acid oxidation is a dominant bioenergetic pathway in prostate cancer. Prostate Cancer Prostatic Dis. 2006; 9:230–234

[5] Jambor I, et al. Functional imaging of localized prostate cancer aggressiveness using 11C-acetate PET/CT and 1H-MR spectroscopy. J Nucl Med. 2010; 51(11):1676-83

[6] Jambor I, et al. Improved detection of localized prostate cancer using co-registered MRI and 11C-acetate PET/CT. Eur J Radiol. 2012; 81(11):2966-72

[7] Mena E, et al. 11C-acetate PET/CT in localized prostate cancer: a study with MRI and histopathologic correlation. J Nucl Med. 2012; 53(4):538-45

[8] Oyama N, et al. 11C-acetate PET Imaging of Prostate Cancer. J Nucl Med. 2002;43:181–6

[9] Huo L, et al. Dual time point C-11 acetate PET imaging can potentially distinguish focal nodular hyperplasia from primary hepatocellular carcinoma. Clin Nucl Med. 2009; 34(12):874-7

[10] Porenta G, Cherry S, Czernin J, et al. Noninvasive determination of myocardial blood flow, oxygen consumption and efficiency in normal humans by carbon-11 acetate positron emission tomography imaging. Eur J Nucl Med. 1999; 26:1465–1474

[11] Vavere AL, Kridel SJ, Wheeler FB, Lewis JS. 1-11C-acetate as a PET radiopharmaceutical for imaging fatty acid synthase expression in prostate cancer. J Nucl Med. 2008; 49:327–334

[12] Lewis DY, et al. Late Imaging with [1-11C] Acetate Improves Detection of Tumor Fatty Acid Synthesis with PET. J Nucl Med. 2014; 55:1144-1149

[13] Buck A, Wolpers HG, Hutchins GD, Savas V, Mangner TJ, Nguyen N, Schwaiger M. Effect of carbon-11-acetate recirculation on estimates of myocardial oxygen consumption by PET. J Nucl Med. 1991; 32(10):1950-7

[14] Yoshii Y, et al. Cytosolic acetyl-CoA synthetase affected tumor cell survival under hypoxia: the possible function in tumor acetyl-CoA/acetate metabolism. Cancer Sci. 2009; 100(5):821-7

[15] Hara T, et al. Effect of hypoxia on the uptake of [methyl-3H]choline, [1-14C] acetate and [18F] FDG in cultured prostate cancer cells. Nucl Med Biol. 2006; 33(8):977-84

[16] Yoshii Y, et al. Tumor uptake of radiolabeled acetate reflects the expression of cytosolic acetyl-CoA synthetase: implications for the mechanism of acetate PET. Nucl Med Biol. 2009; 36(7):771-7

[17] Seltzer MA, et al. Radiation dose estimates in humans for 11C-acetate whole-body PET. J Nucl Med. 2004; 45:1233–1236

[18] Barentsz JO, et al. ESUR prostate MR guidelines 2012. Eur Radiol. 2012; 22(4):746-57
[19] Shields AF, et al. Contribution of labeled carbon dioxide to PET imaging of carbon-11-labeled compounds. J Nucl Med. 1992; 33(4):581-4
[20] Trimmer JK, et al. Recovery of (13)CO2 during rest and exercise after [1-(13)C]acetate, [2-(13)C]acetate, and NaH(13)CO3 infusions. Am J Physiol Endocrinol Metab. 2001; 281(4):E683-92
[21] Polanec SH, et al. Multiparametric [11C]Acetate positron emission tomography-magnetic resonance imaging in the assessment and staging of prostate cancer. PLoS One.2017;12(7):e0180790
[22] Kato T, et al. Accumulation of [11C]acetate in normal prostate and benign prostatic hyperplasia: comparison with prostate cancer. Eur J Nucl Med Mol Imaging. 2002; 29(11):1492-5
[23] Maurer T, et al. Current use of PSMA-PET in prostate cancer management. Nat Rev Urol. 2016; 13(4):226-35
[24] Fendler WP, et al. 68Ga-PSMA PET/CT: Joint EANM and SNMMI procedure guideline for prostate cancer imaging: version 1.0. Eur J Nucl Med Mol Imaging. 2017; 44(6):1014-1024
[25]. Fendler WP, et al. 68Ga-PSMA-HBED-CC PET/CT detects location and extent of primary prostate cancer. J Nucl Med. 2016; 57:1-26
[26] Hamoen EHJ, et al. Use of the Prostate Imaging Reporting and Data System (PI-RADS) for prostate cancer detection with multiparametric magnetic resonance imaging: a diagnostic meta-analysis. Eur Urol. 2014; 67:1112-21
[27] Chen HW, et al. Targeted therapy with fatty acid synthase inhibitors in a human prostate carcinoma LNCaP/tk-luc-bearing animal model. Prostate Cancer Prostatic Dis. 2012; 15(3):260-4

Chapter 6: Thesis summary and conclusions

6.1 Limitations of current technologies

The PI-RADS version-2 system for mpMRI detection of prostate cancer is based on expert consensus opinion and accumulated scientific evidence derived from PI-RADS version-1. The test performance of version-2 in research and clinical practise has been shown to be an improvement over version-1, maintaining a higher diagnostic accuracy compared to standard of care systematic biopsies, as evidenced by the prospective PROMIS trial in the UK. Good performance can be attained in practise when the quality of the diagnostic process can be assured (including PI-RADS compliant MR imaging protocols, image interpretation, reporting and communication, and biopsy procedures), backed up by the robust training of radiologists and urologists working jointly within multidisciplinary teams. Multiparametric MRI detects the majority of tumours capable of causing harm, with the test performance being independent of the exact criteria used to define clinically significant disease. However, mpMRI fails to detect all cancers, and will miss around 10% of clinically significant cancers, highlighting room for improvement. This thesis assesses potential to increase the diagnostic yield of prostate cancer by employing different methods of functional imaging.

6.2 Restatement of aims

Imaging offers great potential for differentiating more aggressive, lethal prostate tumours from less aggressive ones. Although MRI with standard clinical sequences has altered the paradigm of prostate cancer diagnosis, it has inherent limitations and current guidelines actively encourage the development of new sequences. Novel functional MRI and PET

techniques to enable more accurate tumour localisation and characterisation were evaluated in this thesis.

6.3 Summary of main findings

Multiparametric MRI is a difficult technique to perform and interpret due to patient, tumour, radiologist, and MR scanner related factors. It was demonstrated that preparation and patient-related factors can affect the quality of images and attempts should therefore be made to control these in order to optimise image quality and outcomes for any MRI study performed.

The novel sequences of diffusion kurtosis and magnetization transfer imaging were able to readily distinguish benign tissue from tumour, but there was no incremental value over standard clinical sequences and none of the measured parameters reliably differentiated low and high-grade disease. MTI and DKI showed a correlation to ADC values suggesting that cellular density is at least in part contributing to their signal. Interestingly, although both parameters showed strong correlation to each other in normal tissue, this was not maintained in tumour tissue, suggesting that the sequences impart different and potentially complementary information relating to the tumour microenvironment.

An exciting new development in MR imaging is the ability to imaging non-proton nuclei within a reasonable time frame and with sufficient SNR to make clinical imaging feasible. Sodium MRI is one example of this and, as an important electrolyte in maintaining osmoregulation and pH, can potentially offer information on cell membrane integrity and tissue viability. Tissue and intracellular sodium concentrations of the prostate were

successfully quantified in vivo, with differences shown between the normal PZ and TZ and a significantly higher sodium concentration demonstrated within PZ tumours. Further developments in hardware and software and/or increasing magnet strength would be expected to improve SNR and make this technique more clinically available. The underlying physiology of cellular sodium suggests that ^{23}Na-MRI would be ideally suited to monitor treatment response, particularly in the setting of ablative focal therapy to the prostate.

^{11}C-acetate PET-CT was investigated as a technique to identify primary tumours within the prostate gland as a potential adjunct to its more usual means of assessing nodal or bone involvement in more advanced or recurrent disease. Although tumour could not be readily differentiated from benign prostatic hypertrophy, it was shown that despite the short 20-minute half-life of the tracer, late imaging up to 90 minutes was possible and could enable differentiation of tumour tissue from the normal PZ. Establishing the feasibility of late imaging in this context may allow for further exploration of the role of fatty acid synthase in prostate cancer metabolism and will allow for further investigation of the irreversibly labelled pool, representing tumour lipid uptake of acetate.

Ultimately if clear benefit is shown for any of the techniques investigated here, for either tumour localisation or characterisation, a niche role within the diagnostic pathway will need to be established. The pressures of clinical throughput mean that new MRI sequences cannot be added to every study performed, and the use of an endorectal coil for sodium imaging brings an extra invasive and expensive step. In the short to mid-term a potential role could be in assessing for local recurrence post radical radiotherapy. Herein, standard clinical sequences are limited and improved localisation of recurrent tumour can enable

treatment with salvage focal therapy to the gland. Future development of more specific biomarkers such as circulating tumour DNA may provide a further role in problem solving, for instance if their results are discrepant with the findings on standard clinical MRI, further functional imaging may be warranted. Increasingly attention is being drawn to more advanced disease and aggressive treatment options in patients with oligo-metastatic or oligo-progressive disease. This area may provide further opportunities for novel PET-tracers to assess primary and metastatic disease, or for MR imaging within the pelvic field of view to assess high risk patients for locally advanced disease.

6.4 Final conclusions

It has been shown that novel functional imaging techniques can offer different and sometimes divergent information on the tumour and its microenvironment. An incremental value for the novel MRI sequences investigated over existing clinical sequences was not established for lesion localisation, however, some promise has been demonstrated for lesion characterisation. Further work is needed to establish the added benefit and better define the role of novel imaging within the diagnostic pathway for prostate cancer.

Appendix: Peer Reviewed Publications by the author during the study period

1. **T. Barrett**, M. McLean, A. Priest, E. Lawrence, A. Patterson, B. Koo, I. Patterson, A. Warren, A. Doble, V. Gnanapragasam, C. Kastner, F. Gallagher. Diagnostic evaluation of magnetization transfer and diffusion kurtosis imaging for prostate cancer detection in a re-biopsy population. Eur Radiol. 2017 Dec 8. doi: 10.1007/s00330-017-5169-1. [Epub ahead of print] PMID: 29222677

2. M. Greer, J. Shih, **T. Barrett**, S. Bednarova, I. Kabakus, Y. Law, H. Shebel, M. Merino, B. Wood, P. Pinto, P. Choyke, B. Turkbey. All over the map: An Inter-observer agreement study of tumor location based on the PI-RADSv2 sector map. J Magn Reson Imaging. 2018 Jan 17. doi: 10.1002/jmri.25948. [Epub ahead of print] PMID: 29341356

3. L. Valle, M. Greer, J. Shih, **T. Barrett**, Y. Law, A. Rosenkrantz, H. Shebel, A. Muthigi, D. Su, M. Merino, B. Wood. P. Pinto, A. Krauze, A. Kaushal, P. Choyke, B. Turkbey, D. Citrin. Multiparametric MRI for the detection of local recurrence of prostate cancer in the setting of biochemical recurrence after low dose rate brachytherapy. Diagn Interv Radiol. 2018 Jan-Feb; 24(1):46-53. doi: 10.5152/dir.2018.17285. PMID: 29317377

4. N. Hansen, **T. Barrett**, C. Kesch, L. Pepdjonovic, D. Bonekamp, R. O'Sullivan, F. Distler, A. Warren, C. Samel, B. Hadaschik, J. Grummet, C. Kastner. Multicentre evaluation of Magnetic Resonance Imaging supported transperineal prostate biopsy in biopsy-naïve men with suspicion of prostate cancer. BJU Int. 2017 Oct 11. doi: 10.1111/bju.14049. [Epub ahead of print] PMID: 29024425

5. A. Gill, M. Czarniecki, F. Gallagher, **T. Barrett**. A method for mapping and quantifying whole organ diffusion-weighted image distortion in MR imaging of the prostate. Sci Rep. 2017; 7(1):12727. PMID: 28983116

6. N. Hansen, B. Koo, A. Warren, C. Kastner, **T. Barrett.** Subdifferentiating equivocal PI-RADS-3 lesions in multiparametric magnetic resonance imaging of the prostate to improve cancer detection. Eur J Radiol. 2017; 95:307-313. PMID: 28987685

7. D. Thurtle, G. Treece, **T. Barrett**, V. Gnanapragasam. Novel three-dimensional bone 'mapping' software can help assess progression of osseous metastases from routine CT. Radiat Oncol. 2017; 12(1):143. PMID: 28854948

8. M. Greer, J. Shih, N. Lay, **T. Barrett**, L. Bittencourt, S. Borofsky, I. Kabakus, Y. Law, J. Marko, H. Shebel, F. Mertan, M. Merino, B. Wood, P. Pinto, R. Summers, P. Choyke, B. Turkbey. Validation of the Dominant Sequence Paradigm and Role of DCE in PIRADSv2. Radiology. 2017 Jul 19:161316. doi: 10.1148/radiol.2017161316. [Epub ahead of print] PMID: 28727501

9. **T. Barrett**, J. Tanner, A. Gill, R. Slough, J. Wason, F. Gallagher. The longitudinal effect of ejaculation on seminal vesicle fluid volume and whole-prostate ADC as measured on prostate MRI. Eur Radiol. 2017 Jul 4. doi: 10.1007/s00330-017-4905-x. [Epub ahead of print] PMID: 28677052

10. R. Slough, I. Caglic, N. Hansen, A. Patterson, **T. Barrett**. Effect of hyoscine butylbromide on prostate multiparametric MRI anatomical and functional image quality. Clin Radiol. 2017 Aug 10. pii: S0009-9260(17)30388-4. doi: 10.1016/j.crad.2017.07.013. [Epub ahead of print] PMID: 28803622

11. I. Caglic, N. Hansen, R. Slough, A. Patterson, **T. Barrett**. Evaluating the effect of rectal distension on prostate multiparametric MRI image quality. Eur J Radiol. 2017; 90:174-180. PMID: 28583630

12. M. Chetan, **T. Barrett**, F. Gallagher. Clinical significance of prostate 18F-labelled fluorodeoxyglucose uptake on positron emission tomography/computed tomography: A five-year review. World J Radiol 2017; 9(9):350-358. PMID: 29098068

13. **T. Barrett**, M. Haider. The Emerging Role of MRI in Prostate Cancer Active Surveillance and Ongoing Challenges. AJR Am J Roentgenol. 2017; 208(1):131-139. PMID: 27726415

14. N. Hansen, B. Koo, F. Gallagher, A. Warren, A. Doble, V. Gnanapragasam, O. Bratt, C. Kastner, **T. Barrett**. Comparison of initial and tertiary center second opinion reads of multiparametric magnetic resonance imaging of the prostate prior to repeat biopsy. Eur Radiol. 2017; 27(6):2259-2266. PMID: 27778089

15. K. Wadhwa, G. Patruno, A. Patterson, **T. Barrett**, C. Dalia, B. Koo, F. Gallagher, E. Serrao, A. Warren, V. Gnanapragasam, N. Shah, A. Doble, C. Kastner. Robotic assisted laparoscopic radical prostatectomy following transrectal compared to transperineal prostate biopsy: surgical, oncological and functional outcomes. Minerva Urol Nefrol. 2017; 69(1):85-92. PMID: 28009149

16. N. Hansen, **T. Barrett**, B. Koo, A. Doble, V. Gnanapragasam, A. Warren, C. Kastner, O. Bratt. The influence of prostate-specific antigen density on positive and negative predictive values of multiparametric magnetic resonance imaging to detect Gleason score 7-10 prostate cancer in a repeat biopsy setting. BJU Int. 2017; 119(5):724-730. PMID: 27488931

17. N. Hansen, C. Kesch, **T. Barrett**, B. Koo, J. Radtke, D. Bonekamp, H. Schlemmer, A. Warren, K. Wieczorek, M. Hohenfellner, C. Kastner, B. Hadaschik. Multicentre evaluation of target and systematic biopsies using Magnetic Resonance and Ultrasound Image-Fusion guided Transperineal Prostate Biopsy in patients with a previous negative biopsy. BJU Int. 2016 Nov 10. doi: 10.1111/bju.13711. [Epub ahead of print] PMID: 27862869

18. D. Thurtle, R. Hsu, M. Chetan, A. Lophatananon, R. Hubbard, V. Gnanapragasam, **T. Barrett**. Incorporating multiparametric MRI staging and the new histological Grade Group system improves risk-stratified detection of bone metastasis in prostate cancer. Br J Cancer. 2016; 115(11):1285-1288. PMID: 27802450

19. V. Gnanapragasam, K. Burling, A. George, S. Stearn, A. Warren, **T. Barrett**, B. Koo, F. Gallagher, A. Doble, C. Kastner, R. Parker. The Prostate Health Index adds predictive value to multi-parametric MRI in detecting significant prostate cancers in a repeat biopsy population. Sci Rep. 2016; 6:35364. PMID: 27748407

20. E. Lawrence, A. Warren, A. Priest, **T. Barrett**, D. Goldman, A. Gill, V. Gnanapragasam, E. Sala, F. Gallagher. Evaluating Prostate Cancer Using Fractional Tissue Composition of Radical Prostatectomy Specimens and Pre-Operative Diffusional Kurtosis Magnetic Resonance Imaging. PLoS One. 2016;11(7): e0159652. PMID: 27467064

21. N. Hansen, I. Caglic, L. Berman, C. Kastner, A. Doble, **T. Barrett**. Multiparametric Prostate MRI and Cognitively Targeted Transperineal Biopsy in Patients with Previous Abdominoperineal Resection and Suspicion of Prostate Cancer. Urology. 2016; 96:8-14. PMID: 27155312

22. N. Hansen, G. Patruno, K. Wadhwa, G. Gaziev, R. Miano, **T. Barrett**, V. Gnanapragasam, A. Doble, A. Warren, O. Bratt, C. Kastner. Magnetic Resonance and Ultrasound Image Fusion Supported Transperineal Prostate Biopsy Using the Ginsburg Protocol: Technique, Learning Points, and Biopsy Results. Eur Urol. 2016; 70(2):332-40. PMID: 26995327

23. **T. Barrett**. What is Multiparametric-MRI of the Prostate and Why Do We Need It? J Imag Int Rad. 2016; 1(2):1-5

24. I. Caglic, S. Breznik, J. Matela, **T. Barrett**. Lesion Targeted CT-Guided Transgluteal Prostate Biopsy in Combination with Prebiopsy MRI in Patients Without Rectal Access. Urol Case Rep. 2016; 10:6-8. PMID: 27800298

25. **T. Barrett**. Contrast-ing opinions: biparametric versus multiparametric MRI. Diagn Interv Radiol. 2016; 22(3):299. PMID: 27116761

26. G. Gaziev, K. Wadhwa, **T. Barrett**, B. Koo, F. Gallagher, E. Serrao, J. Frey, J. Seidenader, L. Carmona, A. Warren, V. Gnanapragasam, A. Doble, C. Kastner. Defining the Learning Curve for multi-parametric MRI of the prostate using MRI-TRUS fusion guided transperineal prostate biopsies as a validation tool. BJU Int. 2016; 117(1):80-6. PMID: 25099182

27. **T. Barrett**, A. Patterson, B. Koo, K. Wadhwa, A. Warren, A. Doble, V. Gnanapragasam, C. Kastner, F. Gallagher. Targeted transperineal biopsy of the prostate has limited additional

benefit over background cores for larger MRI-identified tumors. World J Urol. 2016; 34(4):501-508. PMID: 26238348

28. E. Serrao and **T. Barrett**, K. Wadhwa, J. Frey, B. Koo, A. Warren, C. Kastner, F. Gallagher. Investigating the ability of multiparametric MRI to exclude significant prostate cancer prior to biopsy. Can Urol Assoc J. 2015; 9(11-12):E853-8. PMID: 26788234

29. **T. Barrett**, B Turkbey, P Choyke. PI-RADS version 2: what you need to know. Clin Radiol. 2015; 70(11):1165-76. PMID: 26231470

30. K. Wadhwa, **T. Barrett**, C. Kastner. The post PSA era: new developments in biomarkers, imaging and biopsy techniques in prostate cancer detection. Trends in Urology & Men's Health. 2015; 6(4):25-29; doi: 10.1002/tre.470

31. **T. Barrett**, A. Priest, E. Lawrence, D. Goldman, A. Warren, V. Gnanapragasam, E. Sala, F. Gallagher. The ADC ratio of tumor to normal prostate as a method for quantifying diffusion weighted imaging of the prostate. AJR Am J Roentgenol. 2015; 205(6):W585-93. PMID: 26587948

32. **T. Barrett**, S. Davidson, B. Wilson, R. Weersink, J. Trachtenberg, M. Haider. Dynamic contrast enhanced MRI as a predictor of vascular-targeted photodynamic focal ablation therapy outcome in prostate cancer post-failed external beam radiation therapy. Can Urol Assoc J. 2014; 8(9-10):E708-E714. PMID: 25408811

33. E. Lawrence, F. Gallagher, **T. Barrett**, A. Warren, A. Priest, D. Goldman, E. Sala, V. Gnanapragasam. Preoperative 3-T diffusion-weighted MRI for the qualitative and quantitative assessment of extracapsular extension in patients with intermediate- or high-risk prostate cancer. AJR Am J Roentgenol. 2014; 203(3):W280-6. PMID: 25148185

34. E. Lawrence, S. Tang, **T. Barrett**, B. Koo, D. Goldman, A. Nelson, K. Wadhwa, A. Warren, R. Axell, A. Doble, F. Gallagher, V. Gnanapragasam, C. Kastner, E. Sala. Prostate Cancer: MRI

targeting performance in the setting of transperineal template re-biopsy using MR-TRUS fusion. Eur Radiol 2014; 24(7):1497-505. PMID: 24744197